

Image reconstruction in magnetic induction tomography

PhD

29th February 2004

Andrew Morris MPhys

UWCC

UMI Number: U584683

All rights reserved

INFORMATION TO ALL USERS

The quality of this reproduction is dependent upon the quality of the copy submitted.

In the unlikely event that the author did not send a complete manuscript and there are missing pages, these will be noted. Also, if material had to be removed, a note will indicate the deletion.



UMI U584683

Published by ProQuest LLC 2013. Copyright in the Dissertation held by the Author.
Microform Edition © ProQuest LLC.

All rights reserved. This work is protected against
unauthorized copying under Title 17, United States Code.



ProQuest LLC
789 East Eisenhower Parkway
P.O. Box 1346
Ann Arbor, MI 48106-1346

Acknowledgements

Many people have helped me, in one way or another, during the course of this PhD. This page is not large (and my memory not competent) enough to list them all, but here are some I'd like to give thanks to.

Firstly, the other members of the MIT research group: my supervisors Bill Gough and Huw Griffiths, Bob Williams and Stuart Watson at University of Glamorgan. I feel lucky to have been involved in such an interesting project, and thank you all for your help and support during those three (plus!) years.

Thanks also go to all the staff members of the Physics department for their dedication and professionalism, of which I am rather envious. Special mention to John Inglesfield for being willing to step into the breach when needed.

Thanks go to my fellow students for making daily life more fun, among them:

Dan Matthews, Mei Jones, Rich Randel, Kate Phillips, Ed Gomez, Ashley James, Doug Boyd, Owen Davies, Emma Pearce, Tom Price, Ian Merrick.

Thanks to the footballers, who kicked me a lot (joke!): Churchy, Gazza, Brownny, Steve-O, Tomo, Leo, Dano, Yimino and Professor Walter Gear. I will miss pushing you all.

Finally, thanks to my wife Helen and my Mam and Dad, without whom none of this would have been possible.

Abstract

Magnetic induction tomography (MIT) is a medical imaging technique that uses magnetic fields to image the electrical properties of the human body. In this work, a numerical model has been described and used to simulate MIT systems. A reconstruction algorithm, based on the sensitivity matrix method, has been used to reconstruct images of the internal conductivity distributions of samples, from simulated and experimental measurements. Images of conductivity contrasts of the magnitude encountered in human body have been successfully reconstructed. An initial investigation has made into wave propagation delays in MIT.

Contents

1. Magnetic induction tomography for biomedical use

1.1.	The electromagnetic field as an investigative tool.....	1
1.2.	MIT development from EIT.....	2
1.3.	Magnetic EIT.....	2
1.4.	MIT systems.....	4
1.5.	Coil geometries.....	5
1.6.	Primary field cancellation.....	8
1.7.	Screening.....	10
1.8.	Amplitude vs. phase measurement.....	11
1.9.	Operating frequency.....	13
1.10.	Simulation studies.....	15
1.11.	Image reconstruction.....	17
1.12.	References.....	20

2. A numerical model for MIT

2.1.	The forward problem in MIT.....	27
2.2.	A finite-difference model for MIT.....	30
2.2.1.	Quasi-static approximation.....	30
2.2.2.	Transmitter coil.....	31
2.2.3.	Dielectric volume, scalar potential and eddy currents.....	34
2.2.4.	Emf induced in receiver coil due to eddy currents.....	38
2.2.5.	Emf induced in receiver coil due to transmitter coil current.....	41
2.2.6.	Grid size generalisation.....	42
2.2.7.	Evaluation of elliptic integrals.....	43
2.2.8.	Refinement of magnetic vector potential calculations.....	45

2.2.8.1.	Magnetic vector potential induced in the dielectric by the transmitter coil.....	45
2.2.8.2.	Emf induced in the receiver coil by eddy currents.....	47
2.3.	Analytical validation of numerical model.....	48
2.4.	Experimental validation of numerical model.....	51
2.5.	Simulating conductivity contrast.....	54
2.5.1.	High-contrast simulations.....	54
2.6.	Summary and conclusions.....	55
2.7.	References.....	58

3. A linear reconstruction algorithm for MIT

3.1.	Introduction.....	59
3.2.	Non-linearity.....	59
3.3.	Linear reconstruction algorithm.....	60
3.3.1.	Sensitivity matrix.....	61
3.3.2.	Calculation of the sensitivity matrix.....	61
3.3.3.	Normalization.....	65
3.3.4.	Singular value decomposition (SVD).....	67
3.3.5.	Spectral expansion.....	69
3.4.	Comparing linear image reconstruction in MIT and EIT via simulations.....	76
3.4.1.	Simulating EIT and MIT measurements.....	76
3.4.2.	Limited height conductivity perturbations.....	76
3.4.3.	Full height perturbations.....	79
3.4.3.1.	Variation of image quality with perturbation position.....	80
3.4.3.2.	Variation of image quality with sensitivity matrix regularisation.....	81
3.4.3.3.	Variation of image quality with conductivity magnitude.....	83
3.5.	Summary and conclusions.....	85
3.6.	References.....	88

4. The imaging performance of simulated MIT systems

4.1.	Introduction.....	90
4.2.	The Cardiff MIT system simulations.....	90
4.2.1.	Difference imaging.....	92
4.2.1.1.	Increasing the number of independent measurements.....	92
4.2.1.2.	Underdetermined sensitivity matrices.....	96
4.2.2.	Imaging with reference to free-space.....	104
4.2.2.1.	Introduction.....	104
4.2.2.2.	Underdetermined free-space sensitivity matrices.....	107
4.2.2.3.	Incorporating simulated noise.....	118
4.3.	Planar array simulation.....	125
4.3.1.	Introduction.....	125
4.3.2.	Cardiff MIT model simulation.....	128
4.3.3.	Simulation results comparison.....	128
4.3.3.1.	Singular value plots.....	128
4.4.	Summary and conclusions.....	132
4.5.	References.....	135

5. Imaging experimental measurements

5.1.	Introduction.....	136
5.2.	High-contrast conductivity distributions.....	137
5.2.1.	Absolute imaging.....	138
5.2.1.1.	Image variation with position.....	138
5.2.1.2.	Two samples.....	140
5.2.2.	Difference imaging.....	140
5.2.3.	Discussion.....	142
5.3.	Low-contrast distributions.....	143
5.3.1.	Absolute imaging.....	144

5.3.1.1.	Agar conductivity phantoms 1.....	144
5.3.2.	Difference imaging.....	146
5.3.2.1.	Agar conductivity phantoms 2.....	146
5.3.3.	Difference imaging with a free-space sensitivity matrix... 147	
5.3.3.1.	Agar conductivity phantoms 1.....	147
5.3.3.2.	Agar conductivity phantoms 2.....	149
5.3.4.	Discussion.....	151
5.3.4.1.	Absolute imaging.....	151
5.3.4.2.	Difference imaging with difference sensitivity matrix.....	152
5.3.4.3.	Difference imaging with a free-space sensitivity matrix.....	152
5.3.5.	Limited height perturbations.....	156
5.3.5.1.	Difference imaging with a difference sensitivity matrix.....	156
5.3.5.2.	Difference imaging with a free-space sensitivity matrix.....	157
5.3.5.3.	Discussion.....	160
5.4.	Summary and conclusions.....	161
5.5.	References.....	163

6. Wave propagation delays in MIT

6.1.	Introduction.....	164
6.2.	Plane wave analysis.....	165
6.2.1.	Theory.....	165
6.2.2.	Previous Work.....	167
6.3.	Near field analysis.....	168
6.3.1.	Introduction.....	168
6.3.2.	Magnetic dipole radiation.....	168
6.3.3.	Transmitter coil radiation.....	170
6.3.4.	Discussion.....	172
6.4.	Experimental measurement of propagation delays.....	173
6.4.1.	Background.....	173
6.4.2.	Description.....	173

6.4.3.	Results and Discussion.....	174
6.5.	Summary and conclusions.....	176
6.6.	References.....	178

7. Future Work

7.1.	Summary of this research.....	180
7.2.	Other areas of potential future work.....	181
7.2.1.	Computer modelling.....	181
7.2.2.	Image reconstruction.....	181
7.2.3.	MIT systems.....	182

1. Magnetic induction tomography for biomedical use

1.1. The electromagnetic field as an investigative tool

Electromagnetic fields are used in a variety of ways to investigate regions invisible to the naked eye. Radio astronomy (Krauss 1986) uses electromagnetic waves to probe distant regions of space, providing new information about the origins of the universe. The field of nondestructive testing, in which manufactured products and materials are checked for safety and reliability using methods that do not degrade their quality, uses various electromagnetic techniques, including magnetic flux leakage, eddy current and microwave methods (Blitz 1991). Geophysical exploration employs ground penetrating radar to probe beneath the earth's surface (Olhoeft 2002), in fields such as archeology and mining. Passive millimetre wave detection technologies are finding use in airport and border security systems (www.QinetiQ.com) and low visibility aircraft landing systems (Shoucri *et al* 1995).

Magnetic induction tomography (MIT) (Griffiths 2001) is a relatively new technique, which involves using magnetic fields produced by transmitter coils to induce eddy currents in a material to be studied. The magnetic fields produced by the eddy currents are measured by receiver coils, from which an image of the electrical properties (electrical conductivity, relative permittivity or magnetic permeability) of the interior of the material can be reconstructed. MIT is currently being investigated in two disparate fields; the process industry

and medical imaging. The research contained in this thesis is focused on the latter area.

1.2. MIT development from EIT

Progress in the field of medical MIT has developed from over twenty years research into electrical impedance tomography (EIT). EIT uses arrays of electrodes attached to the body to inject different current patterns and measure the resulting voltage changes (Barber and Brown 1984). This information can be used to produce cross-sectional images of conductivity and permittivity of the interior of the body. EIT can image absolute values of conductivity and permittivity, or changes in conductivity and permittivity with time, known as difference images. Filtered back-projection (Barber and Seagar 1987) and sensitivity matrix methods (Zadehkoochak *et al* 1991) are the most widely used image reconstruction methods. EIT suffers from low spatial resolution due to the limited number of independent measurements available ($(N-1)*N$ for an N-electrode array, which in turn is restricted by the number of electrodes it is possible to attach to the patient). Electrode positioning uncertainties and random noise also degrade the spatial resolution.

1.3. Magnetic EIT

The use of electrodes to inject current and measure voltages was found to have disadvantages: attaching an electrode array to a patient can be time

consuming; electrode positions are often not known accurately, which degrades the quality of reconstructed images; injected current is blocked by low conductivity tissue, such as the skull, making imaging of interior regions more difficult. Recognising these problems, research was undertaken into the use of magnetic induction as a replacement for electrode current injection (Purvis *et al* 1990, Scaife *et al* 1990, Healy *et al* 1992, Gencer *et al* 1992, Gencer *et al* 1996). Electrode arrays were still used to measure voltage changes. The complementary situation, that of using electrodes to inject current and coils to measure the resulting magnetic field, was investigated by Tozer *et al* 1998.

Using coils to induce currents magnetically overcomes some of the obstacles associated with current injection: the coils remain in a fixed position during operation, thus their position can be known relatively accurately; magnetic induction does not require contact with the body, eliminating time consuming electrode attachment; magnetic fields are not blocked by low conductivity tissue, allowing currents to be induced in areas inaccessible to injected currents. Magnetic EIT systems still suffered from problems associated with the voltage measurement electrodes, inspiring research into fully contactless coil-induction-coil-measurement (MIT) systems.

1.4. MIT systems

Al-Zeibak and Saunders (1993) produced the first report of research into biomedical MIT. The authors used a single channel system that consisted of two co-axial solenoids, and had an operating frequency of 2 MHz. Objects

under investigation were rotated and moved horizontally with respect to the coils, enabling a variety of magnetic field distributions to be used. By performing measurements on different shaped objects, the authors demonstrated that the receiver coil induced emf is roughly proportional to the simple length of the axial path through the object. Image reconstruction, by back projection and filtered back projection, was performed on measurement data derived from simple structures (including a plastic box containing two aluminium cylinders). The images are roughly indicative of the underlying structures, but have large artefacts. However, no images were reconstructed for samples representative of biological tissue (e.g. tissue equivalent saline solution). The validity of some of the results presented in this paper has since been questioned (Griffiths *et al* 1999 – see section 1.8).

Griffiths *et al* (1999) used a 10 MHz single channel MIT system, employing phase sensitive detection, to obtain horizontally scanned profiles of beakers containing tissue equivalent saline solution. The practical measurements agree well with theoretical predictions; for a conductivity change of 1 S/m, the amplitude of the received signal was predicted to change by less than 0.01%. Filtered back-projection was used to reconstruct rotated measurements made on one of the samples.

The first practical realisation of an electronically scanned multichannel MIT system for biomedical applications was presented by Korjnevsky *et al* (2000). This 16 channel system used direct measurement of phase angle, building on earlier theoretical research by the same group (Korzhenevskii and Cherepenin 1997). The system had an operating frequency of 20 MHz, which was mixed down to 20 kHz during the receive process to ease phase

measurement. Filtered back-projection along magnetic flux lines was used to reconstruct an image of a tank of saline solution with embedded regions of higher and lower conductivity, referenced to the saline tank. A lower frequency (10 MHz) MIT system, with a coil geometry based on that of Korjenvesky *et al*, has been reported by Watson *et al* (2002, 2003a). This system utilises heterodyne downconversion of received signals to 10 kHz, which reduces phase instabilities during signal distribution and processing. A digital lock-in amplifier is used to separate the real and imaginary parts of the received signal, relative to a synchronous reference signal. A linear reconstruction algorithm based on inversion of the sensitivity matrix (Morris *et al* 2001a; described in detail in chapters 3 and 4) is used to reconstruct real and imaginary images.

1.5. Coil geometries

The principal requirements of an MIT coil system, namely that the excitation coils induce eddy currents (in a sample) of sufficient size to be measured by receive coils, leave broad scope for variation in coil design and arrangement. Coil radius is one such parameter; a larger transmitter coil radius will produce a more spatially uniform excitation field, while smaller receive coils will allow the magnetic field to be measured at a higher spatial resolution. Increasing the number of turns in a coil increases both the strength of the magnetic field produced (for transmitter coils) and the induced emf (for receive coils). Careful consideration also needs to be given to the resonant frequency of the receiver coils; operation at this frequency will increase the induced emf, but the system

will become much more sensitive to temperature variations and mechanical vibration. The number of coils in a measurement system will define the number of independent measurements possible, and hence influence the spatial resolution. This range of possibilities has led to a number of different MIT measurement system (or 'front end') designs.

As medical MIT has developed predominantly from the field of EIT, it is unsurprising that many MIT coil geometries mimic the classical EIT electrode arrangement. This consists of 16 electrodes placed in a circle on the surface of the sample, in the same plane. Korjnevsky *et al* (2000) used a measurement system consisting of 16 transmitter and receiver coils, located around a circle of diameter 35cm. Each transmit-receive pair was wound on a former of diameter 5cm, the transmitter coils consisting of 2 turns, the receiver coils 4 turns. This circular coil arrangement is also found in industrial process MIT, where Peyton *et al* (1996) describe a system developed at the University of Aveiro consisting of 16 coils arranged on a circle of diameter 15cm. Each coil was used for both transmitting and receiving, with computer controlled system operation. The coils were filled with ferrite rods, a material that has a high magnetic permeability which increases the flux through the coil. This results in a larger induction field, and larger magnetic flux through the receiver coil, compared to air-filled coils.

MIT systems with configurations similar to above suffer from having a reduced sensitivity to central regions of the detector volume. A uniform magnetic field throughout the detector volume would be desirable, thus ensuring no reduction of sensitivity at the centre. It is possible to achieve this by use of a parallel excitation field, which effectively places the sample 'within'

a coil, to utilise the uniform field produced at the coil interior. The majority of magnetic EIT research utilised parallel excitation fields, produced by one or more 'large' (> 5cm diameter) coils. The sample to be imaged was placed into the interior of the coil(s), and was often effectively limited to two dimensions (the size in the dimension parallel to coil axis was much smaller than those in the plane of the coil). Yu *et al* (1993) describe an industrial process MIT system that uses two pairs of orthogonal excitation coils to produce a parallel field, along with 21 receiver coils placed in a ring configuration around the detector volume. Despite the advantage of magnetic field uniformity, this configuration is limited to a very small number of independent measurements, and hence spatial resolution.

Another obvious coil configuration would be that of a planar array. Gencer and Tek (1999) simulated a planar MIT system, consisting of a 7 x 7 plane of excitation coils, displaced 0.5 cm from a 7 x 7 plane of receiver coils. Each coil was 1cm in diameter, and had 1000 turns. Such a coil configuration yields a large number ($49 \times 49 = 2401$) of independent measurements. This planar system simulation was capable of imaging the conductivity of a sample located 0.5cm from the receiver coil plane, to a depth of 2cm.

Although the majority of coils used in MIT systems are constructed from wire wound on non-conducting formers, not all coils are constructed in this way. Rosell *et al* (2001) used a Printed Circuit board (PCB) sensing coil in single channel measurements. This was of square spiral design, having 7 turns with a minimum and maximum diameter of 3.8 and 7.5cm respectively. PCB coils offer the advantage of more precise construction compared with

hand-wound wire coils, but their use as excitation coils is hampered by a lower maximum current, and hence weaker excitation field.

1.6. Primary field cancellation

One of the most challenging aspects of practical MIT system design involves primary field cancellation. For medical MIT, the primary excitation field is significantly larger (100:1 at 10MHz, Griffiths *et al* 1999) than the magnetic field produced by the eddy currents induced in the sample (the 'secondary' magnetic field). Left unaddressed, the primary field will dominate the received signal. Some form of primary field nulling is required, to enable the much smaller secondary field to be measured.

One method, undertaken by Tarjan and McFee (1968) during single channel measurements of full body conductivity, involved using two receiver coils equidistant from a transmitter coil along a common axis; an axial gradiometer. Connection in series opposition lead to a cancellation of the primary field, but as one receiver coil was closer to the sample, the secondary emf induced in the two receive coils was different, and hence did not cancel. This method was also used by Crowley and Rabson (1976) to measure the resistivity of semiconductor samples.

Rosell *et al* (2001) used a planar gradiometer in single channel measurements made on a conducting sphere. This consisted of two square spirals each of 10 turns, aligned adjacent in the same plane and connected in opposition. When the excitation coil axis is aligned with the midpoint of the gradiometer, the primary field signal is nulled. The primary field measured by

the gradiometer was found to be 100 times smaller than the signal measured by the single receiver coil. Unfortunately, this method has the drawback of being insensitive to conductivity perturbations that are symmetrical about the excitation coil axis. It is also unsuitable for use in a multichannel system, as each gradiometer needs to be aligned to one excitation coil, reducing the number of independent measurements of a 16 channel system (for example) from 240 to just 16.

Another variation of this method, in which a single 'back-off' coil was located away from the single channel axis, was reported in Griffiths *et al* 1999. The back-off coil could be rotated until its signal was in antiphase with the primary field in the receive coil, at which point addition of the back-off and receive signals provided the necessary cancellation. This method is not suitable for a multichannel electronically scanned measurement system as it requires manual adjustment.

Primary field cancellation by programmable back-off for process industry MIT was described in Yu *et al* 1994. This involved subtracting a measurement of primary field only (no sample) from subsequent sample measurements, and was programmable in both amplitude and phase. For medical MIT, this approach would require a particularly stable back-off, as any drift in amplitude or phase could introduce large errors into the relatively small phase measurements.

Manipulation of coil geometry allows another method of primary field cancellation. Watson *et al* (2003b) proposed a planar coil array of transmitter coils, with receiver coils mounted at right angles so that no primary flux linked the receiver coils. The receiver signals for all transmitter-receiver

combinations would in theory be zero, for no sample present. Measurements carried out with a single-channel system (suitable for incorporation into such a planar array) have illustrated a reduction of the primary field by a factor of 298 on average (Watson *et al* 2004).

1.7. Screening

The use of confinement screens in MIT are necessary for several reasons. By confining the excitation fields to the detector volume, interference from nearby magnetic or conductive objects that would otherwise be excited is avoided.

The screen also serves to block fields generated wholly outside the detector volume. In general, two types of confinement screens are used; a magnetic shield (composed of high permeability material), and an electromagnetic shield (high conductivity material). Peyton *et al* (1999) reported that use of a soft-magnetic screen also increased the sensitivity of the measurement system by a factor of up to two.

The frequency of excitation influences the type of screen used.

Korzhenevskii and Cherepenin (1997) advocated the use of a ferromagnetic screen for frequencies below the megahertz region (typical in industrial process MIT), as this provides a closed path for the magnetic flux lines. For medical MIT, the simpler option of an electromagnetic screen is recommended. At the frequencies involved (10 – 20MHz) the low skin depth (~10 μ m) of a material such as aluminium stops the magnetic field from penetrating the screen. In contrast to the soft-magnetic screen, eddy currents induced in an electromagnetic screen reduce the imaging sensitivity to

samples inside the array, dependent on the distance of the coils from the screen (Peyton *et al* 2003).

An electromagnetic screen was used in the 20 MHz biomedical MIT system reported in Korjenevsky *et al* (2000), and the 10 MHz biomedical Cardiff MIT system reported in Watson *et al* (2002). Peyton *et al* 1996 describe the University of Aviero 100 kHz MIT system as incorporating a ferrite screen, while the 500 MHz MIT system reported by Yu *et al* 1993 used both an inner magnetic ferrite screen, and an outer copper electromagnetic screen.

1.8. Amplitude vs. phase measurement

Typical industrial process applications, such as imaging the flow of molten metal in pipes (Pham *et al* 1999), involve samples having conductivity or magnetic permeability values that produce significant secondary magnetic fields. For example, Yu *et al* (1994) report a 25% change in signal amplitude, at an operating frequency of 200 kHz. Amplitude measurement in these cases can sufficiently quantify the changes caused by the objects under investigation.

For medical MIT, however, the conductivities of biological tissue (section 1.9) are substantially smaller than those of metals (for example), and the magnetic permeability is effectively unity. This leads to much smaller changes in the amplitude of the received signal. It has been shown theoretically (Griffiths *et al* 1999) that the conductivity of a sample placed into a magnetic field will perturb the signal's imaginary part only, while the relative

permittivity will perturb the real part. From this treatment, the change in signal amplitude caused by a representative sample is of the order of 0.01% for an operating frequency of 10 MHz, significantly smaller than the industrial process MIT scenario. This is in stark contrast to the 73% amplitude change reported by Al-Zeibak and Saunders (1993), for single channel measurements made at the lower frequency of 2 MHz on tissue equivalent saline solution. Although electrical screening was employed in this work, these large amplitude changes are believed to be due to capacitive coupling between the coils (Griffiths *et al* 1999).

An alternative method to amplitude measurement, proposed by Korzhenevskii and Cherepenin (1997), is to measure the change in the phase of the signal. Single channel measurements on a beaker of 1 S/m tissue equivalent saline solution, at an operating frequency of 10 MHz (Griffiths *et al* 1999), showed that the imaginary component of the received emf is approximately 1% the size of the primary signal. This results in a phase change of the order of 1°. To adequately measure phase changes due to pathological or physiological conductivity perturbations, simulation studies have estimated that a phase resolution of the order of a few millidegrees would most likely be required (Morris *et al* 2001b). At an operating frequency of 10 MHz, this presents a significant challenge in system electronics design.

A solution to this problem used by Korjnevsky *et al* 2000, is to 'downconvert' the received signal to a lower frequency. The receiver coil signal (at an operating frequency of 20 MHz) was multiplied by a 19.98 MHz sinusoid, producing a signal containing the sum and difference frequency components. The phase information is preserved, and filtering with a low pass

filter eliminates the 39.98 MHz signal leaving a 20 kHz signal that is much easier to process.

1.9. Operating frequency

The optimum frequency at which the electromagnetic waves are transmitted in an MIT system is a subject open to interpretation. The selection of operating frequency is governed by several factors, including hardware constraints such as the resonant frequency of the transmitter coils, and (for direct phase measurement) the maximum frequency at which the electronic circuitry can function effectively. The information available in the sample to be imaged at a particular frequency is another important factor. Process industry MIT systems can afford to operate at lower frequencies than biomedical MIT systems, as process measurements often involve samples with significantly higher conductivities (e.g. metals) than encountered in biological tissue.

The electrical properties of biological tissue (electrical conductivity and relative permittivity) are frequency dependent. When an external electric field is applied to tissue, a conduction current occurs due to ionic motion within the tissue (Pethig 1987). A time-varying field will cause displacement currents, as a result of the polarisation of bound charges within the tissue. The free and bound charges can be modelled as resistive and capacitive components, having a conductivity σ and relative permittivity ϵ_r . These properties vary with tissue type and frequency, and there are three main regions in the response spectrum where these properties vary significantly (dispersion); the alpha, beta and gamma dispersion regions.

EIT research has focused on the beta dispersion region (1kHz to 1MHz). However, in MIT the phase change in the magnetic field caused by conductivity increases with frequency, hence the use of higher operating frequencies in some MIT systems (10 MHz in Griffiths *et al* 1999, 20 MHz in Korjenevsky and Cherepenin 2000). The conductivity of biological tissue also increases with frequency. Although just outside the beta dispersion region, there is still evidence to suggest that useful information can be obtained at these higher frequencies. Gabriel *et al* (1996) report a comprehensive set of conductivity and permittivity values across the frequency spectrum (10 Hz to 20 GHz), calculated from impedance measurements made mainly on human and ovine tissue *in vitro*. A selection of these conductivity values at EIT and MIT frequencies is reproduced in figure 1.1.

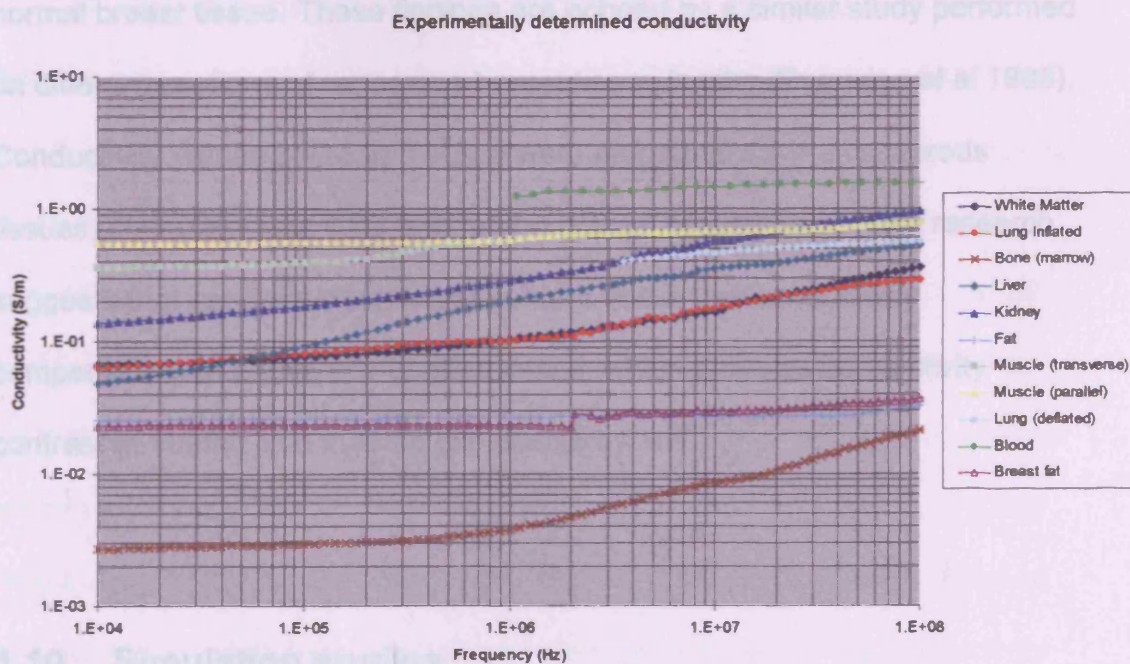


Figure 1.1. Conductivity values of common tissue types in the frequency range 10 kHz to 100 MHz, reproduced from the work of Gabriel *et al* 1996.

These values illustrate the greater contrast between the conductivity of each type tissue at EIT frequencies (10KHz – 1MHz), compared with MIT frequencies (10 – 20 MHz). However, in the latter case there appears to be a greater contrast between two different tissue categories; high water content tissue (e.g. muscle, blood, kidney) and low water content tissue (e.g. fat, bone). The largest conductivity value of biological tissue measured at 10 MHz is 2 S/m for cerebro-spinal fluid (Duck 1990).

There is also evidence to suggest that pathological tissue contrast is available at MIT frequencies. *In vitro* measurements of the dielectric properties of malignant human breast carcinoma and normal breast tissue (Chaudhary *et al* 1984) illustrated a significant conductivity contrast at 10MHz, approximately 0.75 S/m for cancerous tissue compared with 0.15 S/m for normal breast tissue. These findings are echoed by a similar study performed on different sections of cancerous breast tissue *in vitro* (Surowiec *et al* 1988). Conductivity values of 0.4 to 0.9 S/m were measured for the cancerous tissues, compared with 0.03 S/m for the normal breast tissue. This research suggests that cancerous low water content tissue has conductivity comparable with high water content tissue, which provides conductivity contrast at 10MHz that may be exploitable by MIT.

1.10. Simulation studies

A valuable aid to the design and operation of an MIT system is a simulation of the system, in the form of a computer model. This significantly simplifies investigating the effects of system parameter changes (e.g. changing size or

position of coils, estimating signal sizes from samples), reducing the need for often costly and time consuming hardware modifications. System simulations are also vital components of the image reconstruction process. Due to the ill-conditioned, non-linear nature of electromagnetic imaging problems (chapter 3), image reconstruction in MIT is more challenging than many established imaging modalities, such as X-ray computed tomography. Many reconstruction algorithms suitable for MIT require a solution of the 'forward problem', i.e. calculate receive coil emfs produced by the excitation of a certain conductivity distribution. This solution is used as a starting point for solving the 'inverse problem', i.e. calculate the conductivity distribution that, when excited by a certain coil configuration, produces a certain receive coil emf set.

There has been substantial research into EIT simulations, and many of these techniques have been adapted for MIT simulations. Morris *et al* (2001b) report a finite-difference model for simulating biomedical MIT measurements, which is described in full in chapter 2. The planar coil array simulation referred to in 1.5 (Gencer and Tek 1999), utilises the finite-element method (FEM) to provide a solution to the forward problem. The authors derived an expression for the change in secondary magnetic field in terms of the electric scalar potential within the conductive block, which was calculated using the finite-element method. The conductive block was discretized into 5 layers of 10 x 10 volume elements (voxels), and it was assumed that the conductivity and scalar potential were constant on each voxel. A sensitivity matrix, which is a linearized mapping between the changes in conductivity to changes in magnetic field, was calculated. This was used in combination with simulated

measurements to reconstruct images of conductivity perturbations within the block. This simulation is analysed in more detail in chapter 4.

Rosell *et al* (2001) used an adaptation of Geselowitz's lead field theorem to calculate sensitivity maps (receiver coil emf throughout measurement space due to a small perturbation in conductivity) for a circular receiver coil and planar gradiometer. This algorithm was also used to simulate the sensitivity of a 700 kHz single-channel system with an empty detector region (Scharfetter *et al* 2002). In the same work, Finite-Difference Time Domain (FDTD) software called LC (Cray Inc.) was used to simulate a low contrast conductivity distribution, that of a 8 S/m conductive sphere immersed in 4 S/m saline. The FDTD method numerically solves the full Maxwell wave equations for E and H using a time-stepping algorithm (see chapter 6). Results of these simulations (along with corresponding experiments) provide interesting insight into the applicability of the back-projection reconstruction algorithm to biomedical MIT (see section 1.11).

1.11. Image reconstruction

Korjnevsky and Cherepenin (2000) used weighted back-projection to reconstruct images of plastic bottles containing saline solution, both in free space and placed inside a larger saline filled tank. The technique of weighted back-projection was developed for use in X-ray computed tomography, and involves summing weighted projections along a straight line connecting the X-ray source and the detector (Brooks and Di Chiro 1975). Initial EIT systems used filtered back-projection (Barber and Seagar 1987), but with

measurements back-projected along curved equipotential lines. Korjenevsky and Cherepenin applied this technique to MIT, back-projecting along lines of flux linking a transmitter and detector pair. This provided good images of high contrast conductivity perturbations, and back-projection has also been used in industrial MIT studies (Peyton *et al* 1996). Scharfetter *et al* (2002) showed that sensitivity maps for low contrast conductivity perturbations differed greatly from high contrast maps; high contrast distributions have localised zones of sensitivity, while for low contrast distributions the sensitivity zones have a greater spatial extent. This suggests that back-projection may only be suitable for imaging high contrast conductivity perturbations.

Reconstruction algorithms based on sensitivity matrix methods were first applied to EIT (Zadehkoochak *et al* 1991), and then MIT (Gencer and Tek 1999, Morris *et al* 2001a). Analytical or numerical models are used to solve the forward problem for a particular system configuration, and simulate the response to small changes in material parameters (electrical conductivity or relative permittivity). This produces a sensitivity matrix that can be inverted using the Singular Value Decomposition (SVD) technique, to provide an estimation of the original conductivity and/or permittivity distribution. The relationship between the conductivity and voltage measurements is non-linear, but the sensitivity matrix is a linear approximation of this relationship. Consequently, this technique can be used iteratively to obtain improved results. The sensitivity matrix method has been applied to MIT by Gencer and Tek (1999), who used a finite element numerical model as a forward solver. The authors investigated the imaging performance of a 49 coil planar MIT system (placed above a conductive block) through simulations, and found the

system to have good resolution to a depth of 2cm. This study is analysed in more detail in chapter 4. Morris *et al* (2001a) compared images of conductivity, reconstructed from simulated EIT and MIT measurements, using a linear reconstruction algorithm based on the inversion of the sensitivity matrix. This work is described in chapter 3.

The use of artificial neural networks in MIT image reconstruction has been investigated in Korjenevsky *et al* (2001). A 3-layer network utilised simulated measurements as a training set, learning via an error back-propagation algorithm. Images reconstructed from experimental measurements, made on a saline phantom (consisting of a 1% saline bath into which containers of 3% saline and deionised water were placed) showed a marked improvement compared to those from a standard filtered back-projection reconstruction algorithm.

1.12. References

Al-Zeibak S, Saunders NH, 1993, A feasibility study of in vivo electromagnetic imaging. *Phys. Med. Biol.*, vol. **38**, p. 151-160

Barber DC and Brown BH, 1984, Applied Potential Tomograph. *J. Phy. E: Sci. Instrum.*, vol. **17**, p. 723-733

Barber DC, Seagar AD, 1987, Fast reconstruction of resistance images. *Clin. Phys. Physiol. Meas.*, vol. **8**, Suppl. A, p. 47-54

Blitz J, 1991, Electrical and Magnetic Methods of Nondestructive Testing,
Adam Hilger

Brooks RA, Di Chiro G, 1975, Theory of Image Reconstruction in Computer Tomography. *Radiology*, vol. **117**, p. 561-572

Chaudhary SS, Mishra RK, Swarup A, Thomas JM, 1984, Dielectric properties of normal and malignant human breast tissue at radiowave and microwave frequencies. *Indian Journal of Biochemistry and Biophysics*, vol. **21**, p.76-79

Crowley JD, Rabson TA, 1976, Contactless method of measuring resistivity. *Rev. Sci. Instrum.*, vol. **47**, no. 6, p. 712-715

Duck, FA, 1990, Physical Properties of Tissue. Academic Press, New York/London

Gabriel S, Lau RW, Gabriel C, 1996, The dielectric properties of biological tissues: II. Measurements in the frequency range 10 Hz to 20 GHz. *Phys Med Biol* , vol. **41**, p. 2251-2269

Gencer NG, Ider YZ, Kuzuoglu M, 1992, Electrical impedance tomography using induced and injected currents. *Clin. Phys. Physiol. Meas.*, vol. **13**, Suppl. A, p. 95-99

Gencer NG, Ider YZ, Williamson SJ, 1996, Electrical impedance tomography: induced-current imaging achieved with a multiple coil system. *IEEE Trans. BioMedical Engineering*, vol. **43**, no. 2, p. 139-149

Gencer NG, Tek MN, 1999, Electrical conductivity imaging via contactless measurements. *IEEE Trans. Medical Imaging*, vol. **18**, no. 7, p. 617-627

Griffiths H, 2001, Magnetic Induction Tomography. *Meas. Sci. Technol.*, vol. **12**, p. 1-6

Griffiths H, Stewart WR, Gough W, 1999, Magnetic induction tomography: a measuring system for biological tissues. *Annals of NY Acad. Sci.*, vol. **873**, pp 335-345

Healy TJ, Tozer RC, Freeston IL, 1992, Impedance imaging of 3D objects using magnetically induced currents. *Proc. 14th Ann. Int. Conf. IEEE Eng. Med. Biol. Soc.* , vol. **14**, p. 1719-1720

Korzhenevskii AV, Cherepenin VA, 1997, Magnetic induction tomography. *J. Commun. Tech. Electron.* **42** 469-474

Korjnevsky A, Cherepenin V, Sapetsky S, 2000, Magnetic induction tomography : experimental realisation. *Physiol. Meas.*, vol. **21**, no. 1, p. 89-94

Korjnevsky A, 2001, Application of artificial neural networks for static image reconstruction in "Soft Field" tomography, *Proc. 3rd EPSRC Engineering Network Meeting on Biomedical Applications of EIT, 4-6 April, London*

Krauss JD, 1986, Radio Astronomy, Cygnar-Quasar Books

Morris A, Griffiths H, 2001a, A comparison of image reconstruction in EIT and MIT by inversion of the sensitivity matrix. *Scientific Abstracts of 3rd International Conference of EPSRC Engineering Network on Impedance Tomography, London, Apr. 4-6*

Morris A, Griffiths H, Gough W, 2001b, A numerical model for magnetic induction tomographic measurements in biological tissue. *Physiol. Meas.*, vol. **22**, p. 113-119

Olhoeft GR, 2002, Applications and Frustrations In Using Ground Penetrating Radar. *IEEE AESS Systems Magazine*, vol. 17, issue 2, p 12-20

Peyton AJ, Beck MS, Borges AR, de Oliveira JE, Lyon GM, Yu ZZ, Brown MW, Ferrera J, 1999, Development of electromagnetic tomography (EMT) for industrial applications. Part 1: Sensor design and instrumentation. *Proc. 1st World Congress on Industrial Process Tomography, Buxton, UK, 14-17 April*, pp 306-312

Peyton AJ, Watson S, Williams RJ, Griffiths H, Gough W, 2003, Characterising the Effects of the External Electromagnetic Shield on a Magnetic Induction Tomography Sensor. *Proc. 3rd World Congress on Industrial Process Tomography, Banff, Canada*

Pethig R, 1987, Dielectric properties of body tissues. *Clin. Phys. Physiol. Meas.*, vol. 8, suppl. A, p. 5-12

Peyton AJ, Yu ZZ, Lyon G, Al-Zebiak S, Ferreria J, Velez J, Linhares F, Borges AR, Xiong HL, Saunders NH, Beck MS, 1996, An overview of electromagnetic inductance tomography: description of three different systems. *Meas. Sci. Technol.* vol. 7, p. 261-271

Pham MH, Hua Y, Gray NB, 1999, Eddy current tomography for metal solidification imaging. *Proc. 1st World Congress on Industrial Process Tomography, Buxton, UK, 14-17 April*, pp. 451-458

Purvis WR, Tozer RC, Anderson DK, Freeston IL, 1993, Induced current impedance imaging. *IEE Proceedings-A*, vol. **140**, no. 2, p. 135-141

Purvis WR, Tozer RC, Freeston IL, 1990, Impedance imaging using induced currents. *Proc. 12th Ann. Int. Conf. IEEE Eng. Med. Biol. Soc.*, vol. **12**, p. 114-115

Rosell J, Casanas R, Scharfetter H, 2001, Sensitivity maps and system requirements for magnetic induction tomography using a planar gradiometer. *Physiol. Meas.*, vol. **22**, p. 121-130

Scaife JM, Tozer RC, Freeston IL, 1990, Real and imaginary impedance images using induced currents. *Proc. 12th Ann. Int. Conf. IEEE Eng. Med. Biol. Soc.*, vol. **12**, p. 116-117

Scaife JM, Tozer RC, Freeston IL, 1994, Unreferenced imaging using an induced current electrical impedance imaging system. *Electronics Letters*, vol. **30**, no. 5, p. 393-394

Scharfetter H, Riu P, Populo M, Rosell J, 2002, Sensitivity maps for low-contrast-perturbations within conducting background in magnetic induction tomography (MIT). *Physiol Meas*, vol. **23**, p.195-202

Surowiec AJ, Stuchly SS, Barr JR, Swarup A, 1988, Dielectric properties of breast carcinoma and the surrounding tissues. *IEEE Trans. Bio-Medical Engineering*, vol. **35**, no. 4, p. 257-263

Tarjan PP, McFee R, 1968, Electrodeless measurements of the effective resistivity of the human torso and head by magnetic induction. *IEEE Trans. Bio-Medical Engineering*, vol. **BME-15**, no. 4, p. 266-278

Tozer JC, Ireland RH, Barber DC, Barker AT, 1998, Magnetic impedance tomography. *Proceedings of 10th Int. Conf. on Electrical Bioimpedance, Barcelona, Spain, April 5-9*, p. 369-72

Tozer RC, Simpson JC, Freeston IL, Mathias JM, 1992, Noncontact induced current impedance imaging. *Electronics Letters*, vol. **28**, no. 8, p. 773-774

Watson S, Morris A, Williams RJ, Griffiths H, Gough W, 2004, A primary-field compensation scheme for planar array magnetic induction tomography. *Physiol. Meas.*, vol. **25**, p. 271-279

Watson S, Williams RJ, Gough W, Morris A, Griffiths H, 2002, The Cardiff magnetic induction tomography system. *Proc. Int. Med. Fed. Biol. Eng. EMBEC02, Vienna, Austria, Dec. 4-8*, ISBN 3-901351-62-0, vol. **3** (1), p. 116-

Watson S, Williams RJ, Griffiths H, Gough W, Morris A, 2003a, Magnetic induction tomography: phase vs. vector voltmeter measurement techniques. *Physiol. Meas.*, vol. 24, p. 555-564

Watson S, Williams RJ, Griffiths H, Gough W, 2003b, A primary field compensation scheme for planar array magnetic induction tomography. *Abstracts of 4th Conference on Biomedical Applications of Electrical Impedance Tomography, UMIST Manchester 23-25 April*, p36

Yu ZZ, Peyton AJ, Conway WF, Xu LA and Beck MS, 1993, Imaging system based on electromagnetic tomography (EMT). *Electronics Letters*, vol. 29, p. 625-626

Yu ZZ, Peyton AJ, Beck MS, 1994, Electromagnetic tomography (EMT), Part I: Design of a sensor and a system with a parallel excitation field. *Proc. European Concerted Action in Process Tomography, Oporto, Portugal, 24-26 March*, pp. 147-154

Zadehkoochak M, Blott BH, Hames TK, George RF, 1991, Spectral expansion analysis in electrical impedance tomography. *J. Phys. D: Appl. Phys.*, vol. 24, p. 1911-1916

2. A numerical model for MIT

2.1. The forward problem in MIT

The principle of operation for magnetic induction tomography is illustrated in figure 2.1. A sinusoidal current is passed through a transmitter coil, which produces a primary magnetic field (figure 2.1a). This B field induces an emf V in a receiver coil; this is referred to as the primary emf V . When a conductive sample is placed between the coils, the primary B -field induces eddy currents in the conductor (figure 2.1b). These volume eddy currents produce their own magnetic field, referred to as the secondary magnetic field, which causes a perturbation ΔB in the primary B field. This secondary field causes a perturbation ΔV in the induced emf V . It is the quantities $\frac{\Delta B}{B}$ and $\frac{\Delta V}{V}$ that are of interest in MIT.

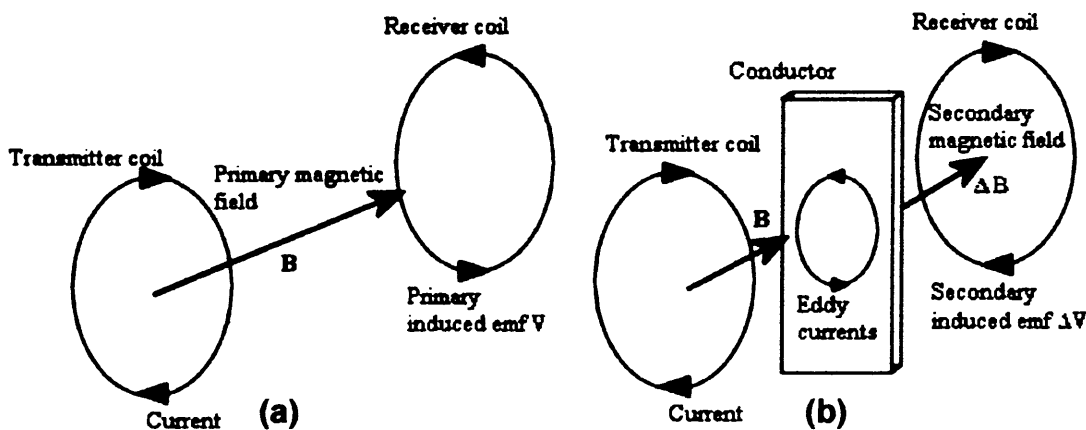


Figure 2.1. (a) The transmitter coil produces a primary magnetic field B , which in turn induces an emf V in the receiver coil. (b) Eddy currents induced in a conducting volume by B produce a secondary magnetic field ΔB , which induces an emf ΔV in the receiver coil.

Solving the forward problem in MIT involves finding $\frac{\Delta V}{V}$, given conductive sample transmitter-receiver coil configuration. This is the first step in the image reconstruction process, and must be solved before solution of the inverse problem (finding the sample properties from the receiver coil emfs) can be attempted. The forward problem is analysed using Maxwell's equations

$$\nabla \cdot \mathbf{D} = \rho \quad (2.1.1)$$

$$\nabla \cdot \mathbf{B} = 0 \quad (2.1.2)$$

$$\nabla \times \mathbf{H} = \mathbf{J} + \frac{\partial \mathbf{D}}{\partial t} \quad (2.1.3)$$

$$\nabla \times \mathbf{E} = -\frac{\partial \mathbf{B}}{\partial t} \quad (2.1.4)$$

where \mathbf{E} is the electric field, \mathbf{B} is the magnetic flux density, \mathbf{H} is the magnetic intensity, \mathbf{D} is the displacement current density, \mathbf{J} is the current density, ρ is the volume charge density, and t denotes time. Supplementary equations relate the field quantities in a linear, isotropic medium

$$\mathbf{D} = \varepsilon \mathbf{E} \quad (2.1.5)$$

$$\mathbf{B} = \mu \mathbf{H} \quad (2.1.6)$$

$$\mathbf{J} = \sigma \mathbf{E} \quad (2.1.7)$$

where ε is the permittivity, μ is the permeability, and σ is the electrical conductivity. The introduction of potentials, namely the electric scalar potential ϕ and the magnetic vector potential \mathbf{A}

$$\mathbf{B} = \nabla \times \mathbf{A} \quad (2.1.8)$$

$$\mathbf{E} = -\nabla \phi - \frac{\partial \mathbf{A}}{\partial t} \quad (2.1.9)$$

aid in the solution of the problem. It can be shown (Sadiku 1992) that the magnetic vector potential \mathbf{A} due to a current density \mathbf{J} , and the electric scalar potential ϕ due to a volume charge density ρ are given by

$$\mathbf{A} = \int \frac{\mu[\mathbf{J}]d\tau}{4\pi r} \quad (2.1.10)$$

$$\phi = \int \frac{[\rho]d\tau}{4\pi\epsilon r} \quad (2.1.11)$$

where $d\tau$ is a volume element, r is the distance between the source and the point at which \mathbf{A} is calculated, and the square brackets denote time retardation (at time $t - \frac{r}{v}$). Once \mathbf{A} and ϕ are known, the \mathbf{E} and \mathbf{B} fields can be calculated using equations (2.1.8) and (2.1.9), and subsequently the emf induced in the receiver coil can be found.

The field of biomedical MIT is only concerned with sinusoidal stimuli, so the governing equations can be expressed in time harmonic form. Taking the divergence of (2.1.3) gives

$$\nabla \cdot (\nabla \times \mathbf{H}) = \nabla \cdot \left(\mathbf{J} + \frac{\partial \mathbf{D}}{\partial t} \right) \quad (2.1.12)$$

Substituting 2.1.5 and 2.1.7 into 2.2.5, and replacing time derivatives by $j\omega$ (time harmonic dependence)

$$\nabla \cdot (\sigma + j\omega\epsilon)\mathbf{E} = 0 \quad (2.1.13)$$

Re-writing $\sigma^* = (\sigma + j\omega\epsilon)$, where $*$ indicates a complex quantity, gives

$$\mathbf{J} = \sigma^* \mathbf{E} \quad (2.1.14)$$

$$\nabla \cdot \mathbf{J} = 0 \quad (2.1.15)$$

Equation (2.1.15), along with the Neumann boundary condition

$$\frac{\partial I}{\partial n} = 0 \quad (2.1.16)$$

(the outward normal component of current on the sample's boundary is zero), describes the eddy current flow within the sample. These equations form the foundation of the numerical model described in section 2.2.

2.2. A finite-difference model for MIT

2.2.1. Quasi-static approximation

A quasi-static finite-difference model, based on the work of Armitage *et al* (1982), has been developed as a forward problem solver. The model simulates a single channel MIT system; this consists of one transmitter coil and one receiver coil, between which a volume of dielectric material that simulates a biological sample is situated. The 'quasi-static' description refers to the fact that the equation

$$\mathbf{A} = \int \frac{\mu \mathbf{J} d\tau}{4\pi r} \quad (2.2.1)$$

which is the unretarded version of equation 2.1.10, is used to calculate the magnetic vector potential \mathbf{A} due to the transmitter coil. Phase differences in the value of \mathbf{A} calculated at different points are neglected. The governing equations are not static (time derivatives are not equal to zero), but also do not have rigorous time-dependence (as retardation is neglected); hence the term quasi-static. The validity of using a quasi-static approximation in MIT at

10 MHz is considered in more detail in chapter 6; here it is assumed to be an appropriate approximation.

Another assumption used is that the magnetic vector potential due to the transmitter coil is not altered by the effects of the eddy currents induced in the sample. The magnetic influence of the induced eddy currents is only considered at the receiver coil, not within the dielectric block itself. This approximation to the primary magnetic vector potential field, as proposed by Gencer *et al* (1994), reduces the number of calculations required.

The structure of this model, coded in Visual Fortran (included in Appendix A), is divided into three sections:- transmitter coil, dielectric volume, and receiver coil.

2.2.2. Transmitter coil

The circular single turn transmitter coil (figure 2.2) has variable position, orientation and radius, and is assumed to be a filament coil. The position vector of the coil centre is referred to as r_1 , while the orientation unit vector (which is orthogonal to the coil area), is n . The current in the coil is sinusoidal with variable frequency.

The magnetic vector potential induced in the dielectric volume by this coil is described by the general equation for a current density J , namely equation (2.2.1).

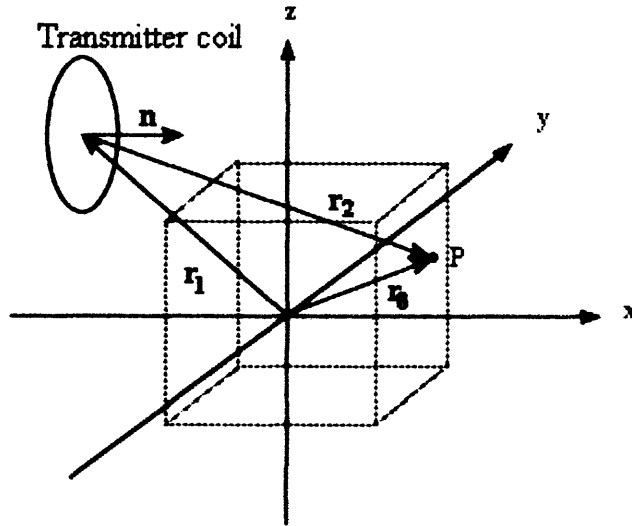


Figure 2.2. Transmitter coil geometry; the transmitter coil position vector (r_1) and orientation unit vector (n), the position vector (r_0) of a field point P, and the vector from the coil centre to P, $r_2 = r_0 - r_1$. The cubic dielectric volume outline is shown by the dashed lines.

For a circular coil of radius a , lying in the $z=0$ plane of a cylindrical polar co-ordinate system, the amplitude of the magnetic vector potential at a point having co-ordinates (r, ϕ, z) is given by equation 2.2.1 (Shadowitz 1975)

$$A_\phi = \frac{\mu_0 I}{2\pi} \sqrt{\frac{a}{r}} F(k) \quad (2.2.2)$$

where

$$F(k) = \left[\left(\frac{2}{k} - k \right) K(k) - \frac{2}{k} E(k) \right] \quad (2.2.3)$$

$$k = \sqrt{\frac{4ra}{z^2 + (r+a)^2}} \quad (2.2.4)$$

and I is the coil current, and $K(k)$ and $E(k)$ are elliptic integrals of the first and second kinds.

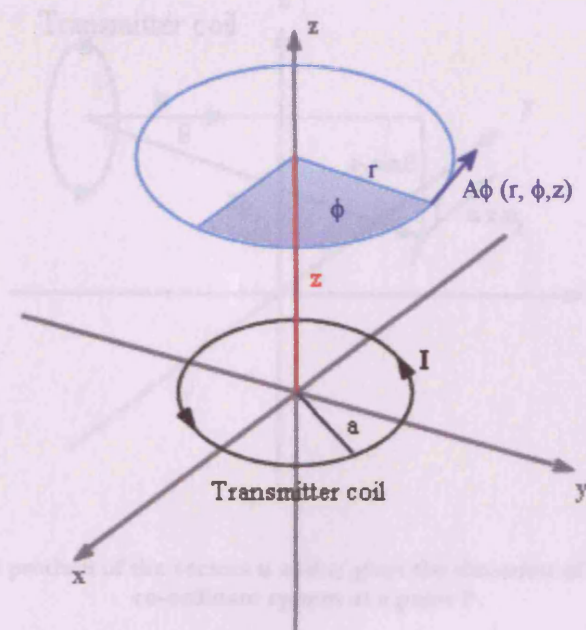


Figure 2.3. The magnetic vector potential A , at cylindrical polar co-ordinates (r, ϕ, z) due to a transmitter coil of radius a carrying current I . Due to the geometry of the scenario, A only has a component in the ϕ direction.

2.2.3. Dielectric volume, scalar potential and eddy currents

The magnetic permeability in free space μ_0 was used because the relative permeability μ_r of all biological tissue types is approximately unity. The magnetic vector potential lines mirror those of current, hence A only has a component in the ϕ -direction (figure 2.3). For a given value of r and z , A_ϕ is independent of ϕ , i.e. A_ϕ has the same value at all points on the blue circle of figure 2.3. The direction of the A field at a point P in the model co-ordinate system can be calculated from the vectors \mathbf{n} and \mathbf{r}_2 . Figure 2.4 illustrates the relationship between these vectors. The cross product of \mathbf{n} and \mathbf{r}_2 gives a vector in the direction of A_ϕ . Dividing this vector by its own magnitude ($r_2 \sin \theta$) gives a unit vector in the direction of A_ϕ , which can be multiplied by equation (2.2.2) to give a full vector description of the magnetic vector potential A at a point in the simulation space.

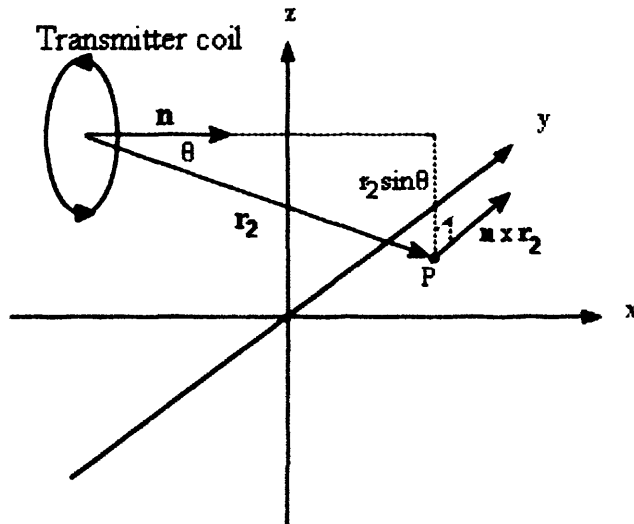


Figure 2.4. The cross product of the vectors \mathbf{n} and \mathbf{r}_2 gives the direction of the \mathbf{A} field in the model co-ordinate system at a point P .

2.2.3. Dielectric volume, scalar potential and eddy currents

The dielectric volume used to simulate biological tissue is comprised of a variable number of cubic voxels. A value of electrical conductivity σ and relative permittivity ϵ_r is assigned to each voxel; in this way different biological entities can be simulated. A node of the finite-difference mesh is located at the centre of each voxel, and between neighbouring nodes a complex admittance Y (figure 2.5) is calculated using the values of conductivity and permittivity (details of this calculation are contained in Appendix B). The amalgamation of conductivity and relative permittivity into the complex quantity admittance results in a complex valued $\frac{\Delta V}{V}$; the real part of $\frac{\Delta V}{V}$ is a measure of the emf phase change due to the relative permittivity, while the imaginary part relates to conductivity.

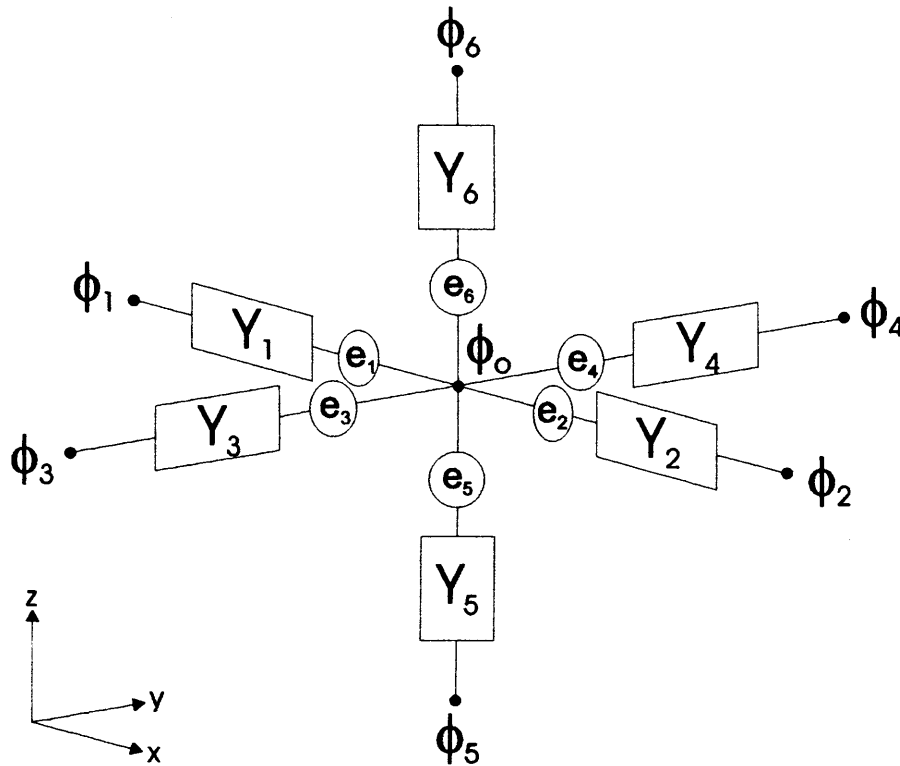


Figure 2.5. Electric scalar potential (ϕ_0) at a node and its nearest neighbours (ϕ_1 - ϕ_6). The admittances Y_{1-6} and vector voltage generator components e_{1-6} are also shown.

The conductivity and relative permittivity are assigned to each grid voxel using a text file containing material codes (the characters '0', '1', '2', etc.). Each code has a specific value of conductivity and permittivity associated with it. The codes are organised into layers, each of which represents one x-y plane at a certain z value. By assigning a material representing free space to peripheral voxels (figure 2.6a), the necessary current-constraining boundary conditions (equation 2.1.1.7) can be enforced. In fact, the free space material code '0' has infinite impedivity (zero conductivity and zero relative permittivity), making it more insulating than free space (which has a relative permittivity of 1). This approximation is valid as the permittivities of materials to be simulated are significantly larger than 1. The free space code can also be used to model samples of more complex geometries (figure 2.6b). An error

trap included in the code involves checking that the outer boundary voxels are all insulating (code '0').

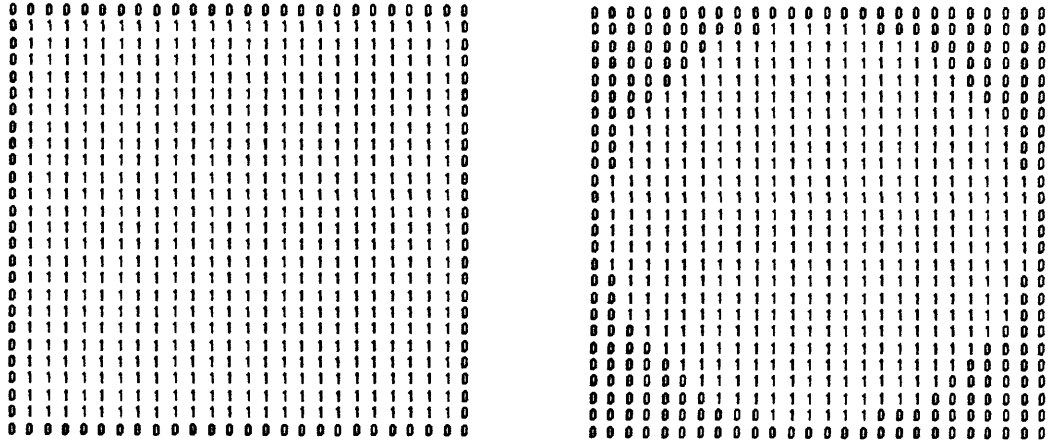


Figure 2.6. Material code text file layers; one layer represents an x-y plane through the grid at a certain z value. (a) insulating voxels (code '0') enforce current boundary conditions, (b) one layer of a cylindrical conducting simulation.

The magnetically induced electric field is modelled using the concept of a vector voltage generator \mathbf{e} , the components of which are located between the mesh nodes (figure 2.5),

$$e = -\frac{\partial A_s}{\partial t} s \quad (2.2.5)$$

where A_s is the component of the magnetic vector potential in a particular direction, and s is the inter-node spacing. Calculation of the eddy currents induced in the dielectric material first requires calculation of the electric scalar potential distribution. The finite-difference form of equation (2.1.16) is

$$\frac{I_1 + I_2 + I_3 + I_4 + I_5 + I_6}{\Delta x} = 0 \quad (2.2.6)$$

where I_{1-6} are the currents into node 0 (notation as in figure 2.5), and Δx is the inter-node spacing. The current can be described in terms of the complex

admittance Y , scalar potential ϕ and vector voltage generator e . For example, for nodes 1 and 0

$$I_1 = Y_1(\phi_1 - \phi_0 + e_1) \quad (2.2.7)$$

which is Ohm's law incorporating the vector voltage generator. Substituting (2.2.7) into (2.2.6) gives

$$\phi_0 = \frac{Y_1(\phi_1 + e_1) + Y_2(\phi_2 + e_2) + \dots + Y_6(\phi_6 + e_6)}{Y_1 + Y_2 + \dots + Y_6} \quad (2.2.8)$$

In this way the scalar potential at a node can be calculated iteratively using the six nearest neighbour values. If the most recently updated values are used in the above equation, this is known as the Gauss-Seidel method. In this model the successive over-relaxation method (Sadiku 1992) was used, in which the change in scalar potential at a node from one iteration to the next is calculated using

$$\Delta\phi_0 = \phi_0^n - \phi_0^{n-1} \quad (2.2.9)$$

and the new value of ϕ^n is found using

$$\phi_0^n = \phi_0^{n-1} + k\Delta\phi_0 \quad (2.2.10)$$

where the superscripts denote the n^{th} iteration. The factor k determines the rate of convergence of the iteration process; $1 < k < 2$ (a value greater than 2 causes instability, while a value of 1 is equivalent to the Gauss-Seidel method). The amount that the sum of the squares of the increments of scalar potential $\sum |\Delta\phi_0|^2$ reduces by after each iteration, gives an indication of the state of convergence of the scalar potential. Once the potential has converged satisfactorily, equation (2.2.7) calculates the eddy currents induced in the dielectric. The current I , like the admittance Y , is a complex quantity.

2.2.4. Emf induced in receiver coil due to eddy currents

The receiver coil was modelled as an n-sided polygon (figure 2.7). The coil, of radius b , is defined by the equations

$$\mathbf{m} \cdot \mathbf{b} = 0 \quad (2.2.11)$$

$$b_x^2 + b_y^2 + b_z^2 = b^2 \quad (2.2.12)$$

where \mathbf{m} is the orientation unit vector of the receiver coil, and \mathbf{b} is a vector from the coil centre to a point on the coil. The local coil axis \mathbf{b}_0 is defined to be perpendicular to the orientation unit vector \mathbf{m} , such that

$$\mathbf{b}_0 = (b_{0x}, b_{0y}, b_{0z}) \quad (2.2.13)$$

where

$$b_{0x} = -\frac{b}{\sqrt{1 + \frac{m_y^2}{m_x^2}}} \quad (2.2.14)$$

$$b_{0y} = \frac{b}{\sqrt{1 + \frac{m_y^2}{m_x^2}}} \quad (2.2.15)$$

$$b_{0z} = 0 \quad (2.2.16)$$

except for the following two special cases;

when $|m_x| < 10^{-6}$ metres

$$\mathbf{b}_0 = (b, 0, 0) \quad (2.2.17)$$

when $|m_y| < 10^{-6}$ metres

$$\mathbf{b}_0 = (0, b, 0) \quad (2.2.18)$$

The second local coil axis \mathbf{b}_1 is defined to be perpendicular to \mathbf{b}_0 and \mathbf{m}

$$\mathbf{b}_1 = \mathbf{m} \times \mathbf{b}_0 \quad (2.2.19)$$

such that any point on the coil is described by the vector \mathbf{b} in terms of \mathbf{b}_0 and \mathbf{b}_1

$$\mathbf{b} = \mathbf{b}_0 \cos \theta + \mathbf{b}_1 \sin \theta \quad (2.2.20)$$

where θ is the angle from the \mathbf{b}_0 axis to the coil axis position vector \mathbf{b} . The position vector \mathbf{r}_p of the coil element in the main co-ordinate system is given by

$$\mathbf{r}_p = \mathbf{r}_3 + \mathbf{b} \quad (2.2.21)$$

where \mathbf{r}_3 is the position vector of the receiver coil centre (figure 2.8).

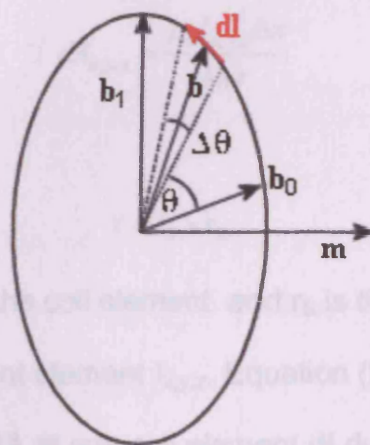


Figure 2.7. The receiver coil is modelled as an n-sided polygon. The orientation unit vector (\mathbf{m}), and two local coil axes (\mathbf{b}_0 and \mathbf{b}_1) allow the position vector (\mathbf{b}) of each coil element ($d\mathbf{l}$) to be specified.

The sides of the regular polygon are specified as vector coil elements $d\mathbf{l}$

$$d\mathbf{l} = 2(\mathbf{b}_1 \cos \theta - \mathbf{b}_0 \sin \theta) \sin \frac{\Delta \theta}{2} \quad (2.2.22)$$

where $\Delta \theta$ is the angle subtended by $d\mathbf{l}$.

At each of the coil elements, the magnetic vector potential components $dA_{x,y,z}$ due to each eddy current element $I_{x,y,z}$ are given by

$$dA_{x,y,z} = \frac{\mu_0 I_{x,y,z}}{4\pi} \int_{\text{along current element}} \frac{df}{r} \quad (2.2.23)$$

where r is the distance from the coil element $d\mathbf{l}$ to a point on the eddy current element $I_{x,y,z}$ (figure 2.8), and the integral is along the eddy current element.

The size of the current element (which is equal to the grid spacing Δx) is assumed to be small compared with r , and so all points on $I_{x,y,z}$ are assumed to be at an equal distance (r) from the coil element. This allows equation (2.2.23) to be written as

$$dA_{x,y,z} = \frac{\mu_0 I_{x,y,z} \Delta x}{4\pi r} \quad (2.2.24)$$

where r is calculated from

$$\mathbf{r} = \mathbf{r}_P - \mathbf{r}_E \quad (2.2.25)$$

\mathbf{r}_P is the position vector of the coil element, and \mathbf{r}_E is the position vector of the mid-point of the eddy current element $I_{x,y,z}$. Equation (2.2.24) calculates the magnetic vector potential $d\mathbf{A}$ at one coil element $d\mathbf{l}$ due to one current element I . To obtain the vector potential \mathbf{A} at one coil element due to all current elements, equation (2.2.24) must be summed over the entire finite-difference grid

$$\mathbf{A} = \sum_{\text{dielectric grid}} d\mathbf{A} \quad (2.2.26)$$

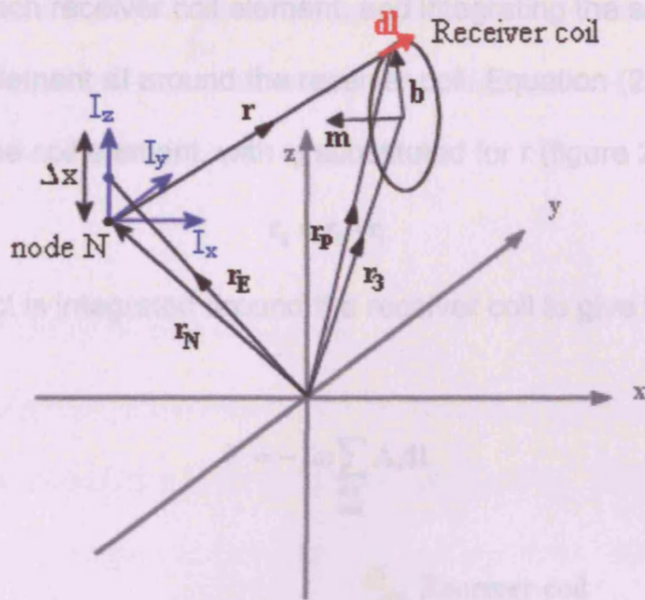


Figure 2.8. The eddy current elements I_z , which has a position vector r_E , is distance r from the receiver coil element dl , which has a position vector r_p .

The emf ΔV , induced in receiver coil due to the eddy currents in the dielectric block, is calculated by integrating the time derivative of the vector potential \mathbf{A} at each coil element, using

$$\Delta V = -j\omega \oint_{\text{Rx coil}} \mathbf{A} \cdot d\mathbf{l} \quad (2.2.27)$$

which is realised in practice by summing the scalar product of the vector potential \mathbf{A} and the coil elements $d\mathbf{l}$

$$\Delta V = -j\omega \sum_{\text{Rx coil}} \mathbf{A} \cdot d\mathbf{l} \quad (2.2.28)$$

2.2.6. Grid size generalization

2.2.5. Emf induced in receiver coil due to transmitter coil current

The alternating current in the transmitter coil directly induces an emf V in the receiver coil (which is the emf induced in the absence of the dielectric volume). This primary emf is found by calculating the magnetic vector

potential \mathbf{A} at each receiver coil element, and integrating the scalar product of \mathbf{A} and the coil element $d\mathbf{l}$ around the receiver coil. Equation (2.2.2) is used to calculate \mathbf{A} at the coil element, with r_2 substituted for r (figure 2.9), where

$$\mathbf{r}_2 = \mathbf{r}_0 - \mathbf{r}_1 \quad (2.2.29)$$

The $\mathbf{A} \cdot d\mathbf{l}$ product is integrated around the receiver coil to give the primary emf V .

$$V = -j\omega \sum_{\text{Rx coil}} \mathbf{A} \cdot d\mathbf{l} \quad (2.2.30)$$

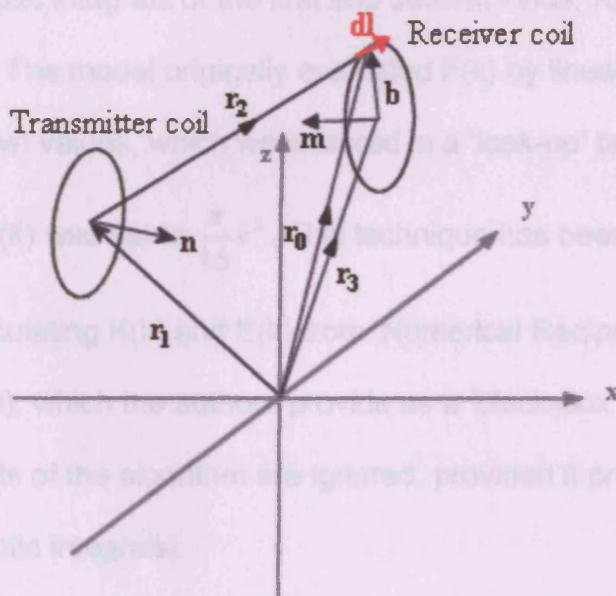


Figure 2.9. The transmitter coil induces a 'primary field' emf V in the receiver coil. The receiver coil element $d\mathbf{l}$, which has a position vector \mathbf{r}_0 , is a distance r_2 away from the transmitter coil centre.

2.2.6. Grid size generalisation

The model code was altered to allow any size of cubic grid, removing the constraint of a $14 \times 14 \times 14$ grid that had previously been enforced. This allowed more accurate geometrical representations of non-cubic distributions, but at the cost of increased program execution time. It should also be noted

that large grid sizes (>100 x 100 x 100) resulted in convergence problems with regards the scalar potential calculation, and thus were avoided. The cause of this problem has not been established.

2.2.7. Evaluation of elliptic integrals

The magnetic vector potential distribution induced in the dielectric block by the transmitter coil is formulated in terms of the function $F(k)$. This is a function of the complete elliptic integrals of the first and second kinds, $K(k)$ and $E(k)$, equation (2.2.3). The model originally evaluated $F(k)$ by linearly interpolating between 23 known values, which were stored in a 'look-up' table. For values of k below 0.1, $F(k)$ was set to $\frac{\pi}{16}k^3$. This technique has been replaced by an algorithm for calculating $K(k)$ and $E(k)$ from 'Numerical Recipes in Fortran', by Press *et al* (1989), which the authors provide as a 'black-box' routine (i.e. the operational details of the algorithm are ignored, provided it produces accurate values of the elliptic integrals).

Figure 2.10 shows $F(k)$ values produced by the 23 value interpolation method (red line) and Numerical Recipes algorithm (green line), and compares these with values produced by the Matlab elliptic integral function 'ellipke' (blue line, taken to be the 'actual' $K(k)$ and $E(k)$ values). For the interpolation, the $F(0.85)$ and $F(0.90)$ values were retrieved from the look-up table, and the intermediary values of F ($k = 0.86$ to 0.89) were calculated by linear interpolation.

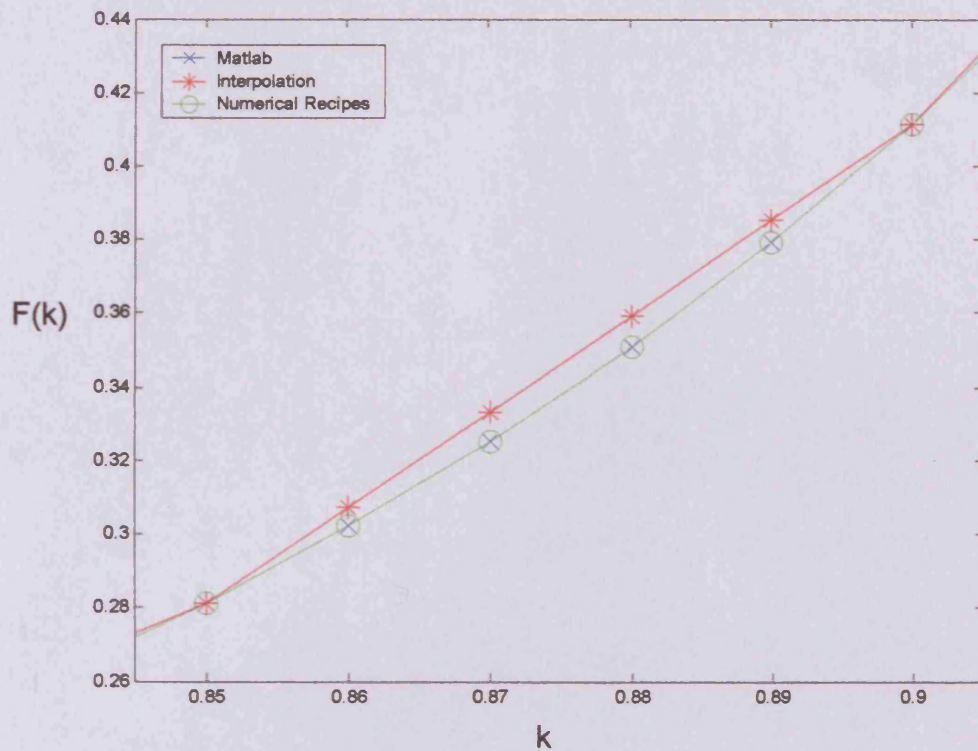


Figure 2.10. Comparison of $F(k)$ values for the linear interpolation method (red line), Numerical Recipes method (green line), and Matlab values (blue line).

For these values of k , the Numerical Recipes $F(k)$ values agree more closely with the Matlab values than those calculated by interpolation (the green line overlaps the blue line). The accuracy of the interpolation method could have been improved by storing more look-up table values (e.g. at every $k = 0.01$), however it was considered simpler to use the Numerical Recipes algorithm to obtain the same level of accuracy.

2.2.8. Refinement of magnetic vector potential calculations

2.2.8.1. Magnetic vector potential induced in the dielectric by the transmitter coil

The magnetic vector potential \mathbf{A} is calculated at each node in co-ordinate directions x, y and z. These values are used to calculate the vector voltage generators, which induce emfs between nodes. The induced emf ε between one node and its neighbour is given by

$$\varepsilon_c = -j\omega \int A_c \cdot dl \quad (2.2.31)$$

where the subscript c denotes the directional component, ω is the angular frequency of the source radiation, and dl is the line element connecting a node and its nearest neighbour (e.g. between node 0 and node 2 in figure 5).

The implementation of equation (2.2.31) in the model was achieved using equations of the form

$$\varepsilon_{+x} = -\frac{j\omega\Delta x}{2} [A_x(n) + A_x(n+1)] \quad (2.2.32)$$

where Δx is the inter-node spacing, and the bracketed n and n+1 refer to the nodes at which the vector potential values are calculated. Equation (2.2.32) is specifically for the vector voltage generator in the +x direction. Figure 2.11 illustrates this in one dimension; the magnetic vector potential x-component is considered to have a constant value of $A_x(n)$ for half the length of the line between nodes n and n+1 (red region), while along the second half of the line the value is constant at $A_x(n+1)$ (blue region).

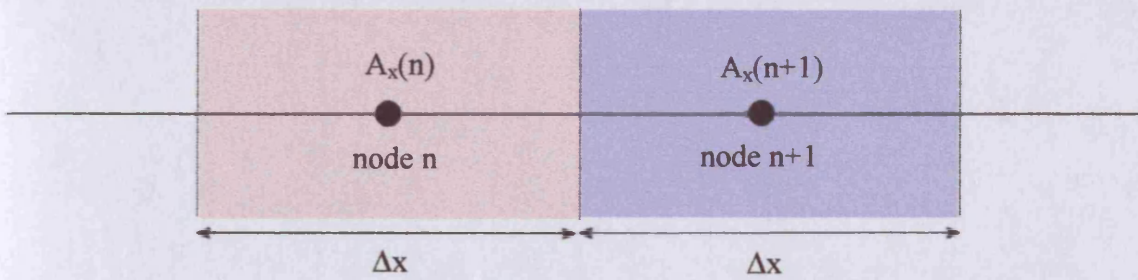


Figure 2.11. The magnetic vector potential A is calculated at nodes n and $n+1$, and is constant over a distance $-\Delta x/2$ to $+\Delta x/2$ around each node (red region for node n , blue region for node $n+1$).

Equation (2.2.32) is valid as long as A_x varies linearly between the nodes, which is the case when the distance from the transmitter coil to the dielectric is significantly larger than the inter-node spacing. However, when the coil is close to the sample (i.e. when the inter-node spacing is comparable with the coil-to-sample displacement) a closer approximation to the integral in equation (2.2.31) is required. This is achieved by calculating the magnetic vector potential at various points between the two nodes, rather than just at the nodes themselves. The equation

$$\varepsilon_{+x} = -j\omega\Delta x \left[\frac{A_x^1 + A_x^m}{2(m-1)} + \sum_{i=2}^{m-1} \frac{A_x^i}{m-1} \right] \quad (2.2.33)$$

illustrates how these A_x values are combined to produce the induced emf between two nodes (again, equation (2.2.33) is specifically for vector voltage generator in the $+x$ direction). Here m is the number of points between (and including) nodes n and $n+1$ at which A_x is calculated. Figure 2.12 illustrates this concept for $m = 5$ in one dimension; the vector potential values A_x^1 and A_x^5 are calculated at the nodes n and $n+1$ respectively, while A_x^2 , A_x^3 , and A_x^4 are calculated at points spaced $\frac{\Delta x}{4}$ along the line (the superscripts on the A values are a numbering scheme, rather than indices). The different coloured

regions illustrate the distance over which the vector potential is considered constant.

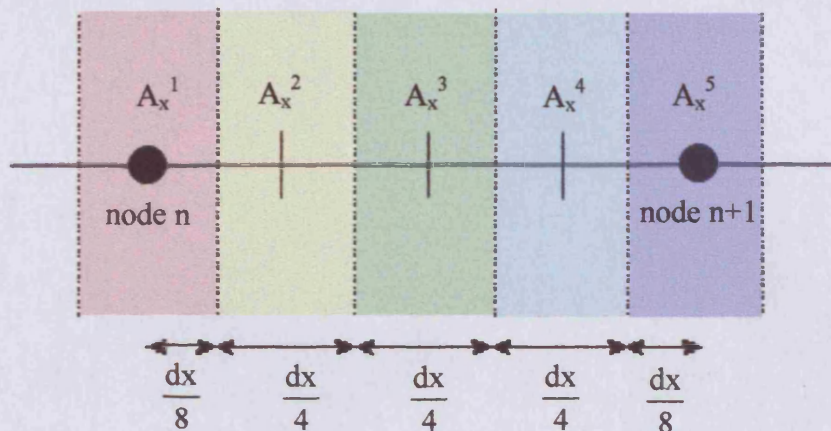


Figure 2.12. The magnetic vector potential is calculated at five points, including the nodes n and $n+1$. The different colour regions indicate lengths over which the A values are constant.

All nodes within a certain user-defined distance (e.g. $10 \cdot \Delta x$) of the coil centre are included in this refinement calculation.

2.2.8.2. Emf induced in the receiver coil by eddy currents

Equation (2.2.24) calculates the magnetic vector potential $d\mathbf{A}$ at a receiver coil element due to one eddy current. This approach is valid when the distance r from the eddy current element to the coil element is much less than the length of the eddy current element (for current elements far from the coil, the distance r is approximately equal at all points along the current element length). For current elements close to the coil, it is possible for r to vary significantly from one end of a current element to the other (figure 2.13, $r_1 > r_5$). An amendment to equation (2.2.24) has been introduced for such elements.

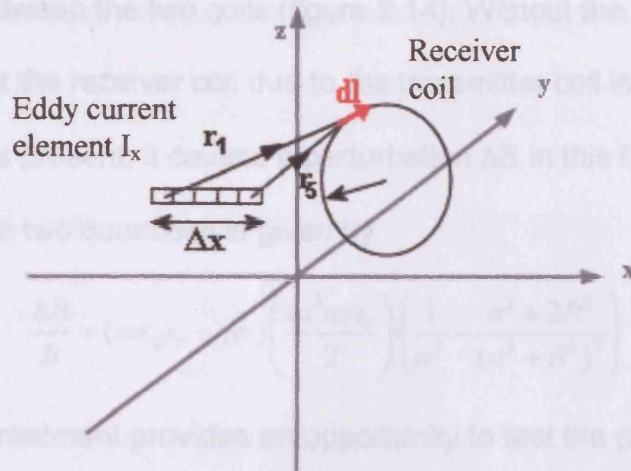


Figure 2.13. An eddy current element I_x close ($\Delta x \sim r$) to the receiver coil. The distance (r_1 to r_2) of points along the current element from a coil element (dl) can vary significantly; hence the current element is split into smaller parts, and the distance calculated to each.

This involves splitting each current element into n smaller elements of equal length, and calculating the contribution from each smaller element to the magnetic vector potential at the receiver coil separately, using

$$dA_{x,y,z} = \frac{\mu_0 I_{x,y,z} \Delta x}{4\pi n} \sum_n \frac{1}{r_n} \quad (2.2.34)$$

Equations (2.2.26) and (2.2.28) are then used, as before, to calculate the emf ΔV induced in the receiver coil by the eddy currents.

2.3. Analytical validation of numerical model

An analytical treatment of the magnetic interaction of a dielectric disk with a simple two coil system is given in Griffiths *et al* 1999. The small coils (one transmitter and one receiver) are positioned co-axially, separated by a distance $2a$. The circular disk, of radius R and thickness t , is located coaxially

and centrally between the two coils (figure 2.14). Without the disk, the magnetic field at the receiver coil due to the transmitter coil is denoted by B . When the disk is present, it causes a perturbation ΔB in this field, such that the ratio of these two quantities is given by

$$\frac{\Delta B}{B} = (\omega \epsilon_0 \epsilon_r - j\sigma) \left(\frac{t a^3 \omega \mu_0}{2} \right) \left\{ \frac{1}{a^2} - \frac{a^2 + 2R^2}{(a^2 + R^2)^2} \right\} \quad (2.3.1)$$

This analytical treatment provides an opportunity to test the performance of the MIT model. The situation described above was simulated, with the conductivity and the relative permittivity of the disk set to 1 S/m and 1 respectively.

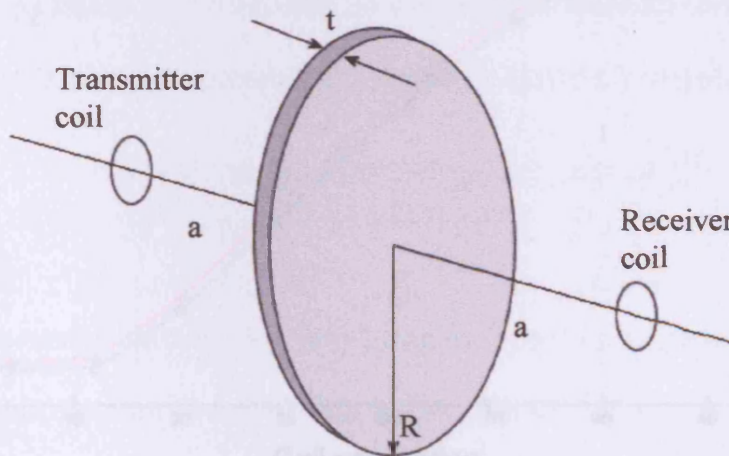


Figure 2.14. Circular disk of radius R and thickness t , with a transmitter and receiver coil both distance a from the disk centre.

The radius and thickness of the disk were 12cm and 1cm respectively, while the transmitter frequency used was 10 MHz. As the derivation in Griffiths *et al* (1999) approximated the transmitter coil as a magnetic dipole moment, the coil radii were set to the relatively small value of 0.5cm. The coil separation was varied from 12 to 48cm, ensuring that the condition $t \ll 2a$ ($1\text{cm} \ll$

24cm) was not violated. Another constraint satisfied was that the skin depth

$$\delta = \sqrt{\frac{2}{\omega\mu_0\sigma}}$$

, which for this situation was equal to 15cm, was much greater

than the disk thickness (1cm), so that the attenuation produced by the disk

was small. The values of $\frac{\Delta B}{B}$ for the analytical and numerical methods are

shown in figure 2.15.

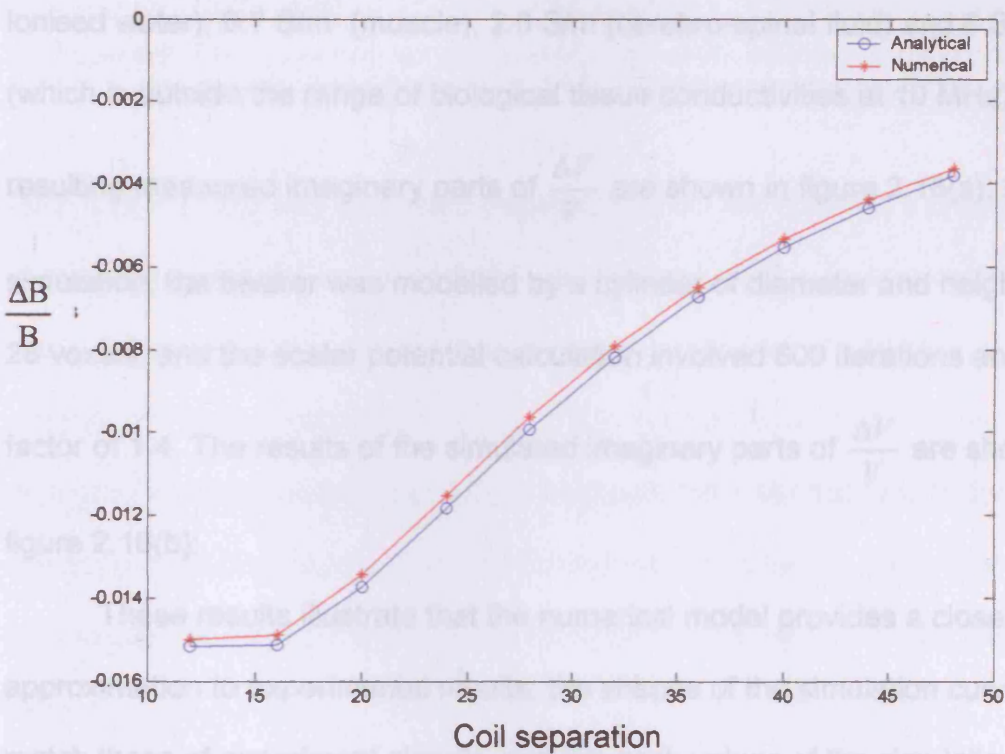


Figure 2.15. Comparison of $\Delta B/B$ vs. coil separation for analytical (blue line) and numerical (red line) methods

The largest difference between the analytical and numerical $\frac{\Delta B}{B}$ values was

4%. This example illustrates the good agreement found between the

numerical model and analytically derived results.

2.4. Experimental validation of numerical model

An experiment described in Griffiths *et al* (1999), involving a single channel 10 MHz MIT system, has been simulated. The system consisted of a 9 cm diameter transmitter coil and a 1.5 cm diameter receiver coil, located coaxially 17.5 cm apart. A beaker with diameter and depth both 9 cm was placed at different horizontal displacements halfway between the coils. Different saline solutions were placed inside the beaker, 0.001 S/m (corresponding to de-ionised water), 0.7 S/m (muscle), 2.0 S/m (cerebro-spinal fluid) and 6 S/m (which is outside the range of biological tissue conductivities at 10 MHz). The resulting measured imaginary parts of $\frac{\Delta V}{V}$ are shown in figure 2.16(a). In the simulation, the beaker was modelled by a cylinder of diameter and height both 28 voxels, and the scalar potential calculation involved 600 iterations and a 'k' factor of 1.4. The results of the simulated imaginary parts of $\frac{\Delta V}{V}$ are shown in figure 2.16(b).

These results illustrate that the numerical model provides a close approximation to experimental results; the shapes of the simulation curves match those of experiment closely, and the peak values of the simulation curves '0.7 S/m', '2.0 S/m' and '6.0 S/m' agree to within 14% of the corresponding experimental values. The '0.001 S/m' experimental and simulated values differ significantly; such a small conductivity would be expected theoretically to produce a much smaller signal than observed experimentally. The over-large experimental values are due to a baseline drift, as commented on by the authors.

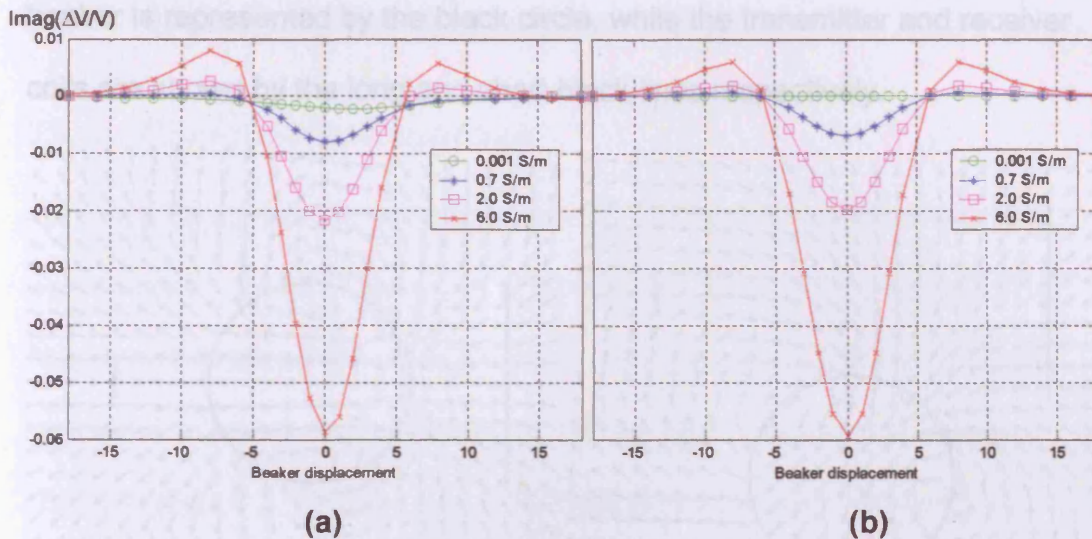


Figure 2.16. Experimental (a) and simulated (b) values of the imaginary part of $(\Delta V/V)$ vs. perpendicular beaker displacement, for four different sample conductivities.

Both experimental and simulated displacement curves illustrate a change in sign as the beaker is displaced from the common coil axis by approximately 5cm. The cause of this change in sign can be visualised with the aid of magnetic field-line plots (figure 2.17). These two dimensional plots were produced by using equation (2.4.1) to calculate the magnetic field \mathbf{B} due to the eddy current elements $d\mathbf{l}$ induced in the sample *only*, i.e. the primary field was neglected (where \mathbf{r} is the vector from the current element to the field point)

$$\mathbf{B} = \frac{\mu_0}{4\pi} \sum_{\text{current elements}} \frac{d\mathbf{l} \times \hat{\mathbf{r}}}{r^2} \quad (2.4.1)$$

This calculation was performed for all positions in a 24 x 21 grid in the vicinity of the coils and sample. For clarity, only the components of magnetic field in a plane that passes through the coil centres and at right angles to the cylinder axis, are shown in figure 2.17. The arrow sizes have been scaled logarithmically to clearly represent the varying magnetic field magnitudes. The

beaker is represented by the black circle, while the transmitter and receiver coils are shown by the long and short black lines respectively.

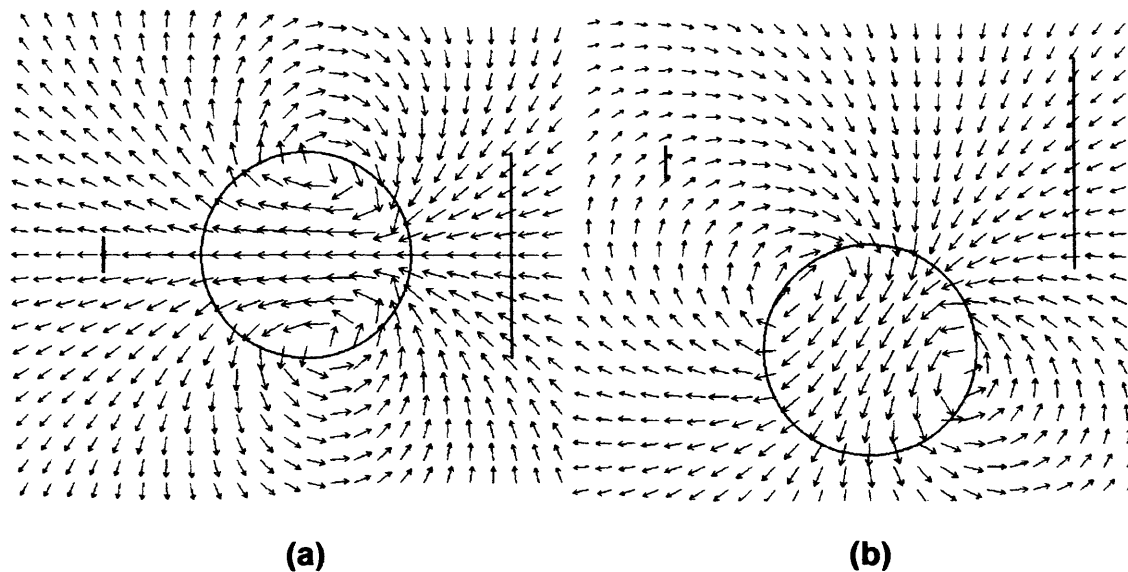


Figure 2.17. The magnetic field due to the current distribution in the saline-filled beaker, for the central position between the coils (a) and for a sideways displacement of 8cm (b). The positions of the transmitter and receiver coils are indicated by the long and short black lines respectively.

In figure 2.17(a), the sample is positioned on the common coil axis, and the magnetic flux links the receiver coil from right to left. The 8cm sideways displacement of the sample in 2.17(b) causes changes in the orientation of the magnetic field lines, reversing the direction of flux linkage at the receiver coil. This change in the direction of flux through the receiver coil is the cause of the sign change observed in the beaker displacement profiles of figure 2.16.

2.5. Simulating conductivity contrast

2.5.1. High-contrast simulations

In order to image conductivity changes due to physiological functions (e.g. cardiac cycle), an MIT system must be capable of measuring the resulting magnetic field phase changes. To obtain a rough estimate of the required resolution, a 3cm diameter insulating rod has been simulated at various positions (figure 2.18) within the 2 S/m saline-filled beaker simulated in section 2.4. This scenario describes a larger conductivity contrast (and hence larger magnetic field phase changes) than is likely to occur in biological tissue at 10MHz.

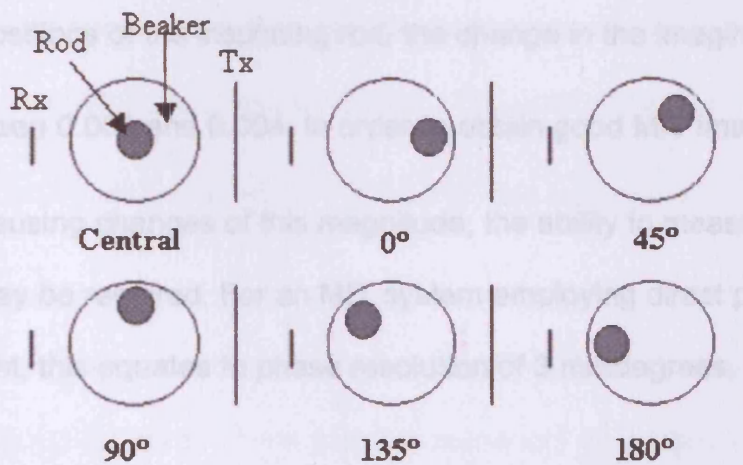


Figure 2.18. The positions of the insulating rod inside the beaker, with respect to the transmitter (short line) coil and receiver (long line) coil positions.

The beaker was again moved horizontally between the coils. Figure 2.19

shows the change in the imaginary part of $\frac{\Delta V}{V}$ caused by the introduction of

the rod into the beaker, for the six different rod positions. For clarity, the central rod position only is shown in 2.19(a).

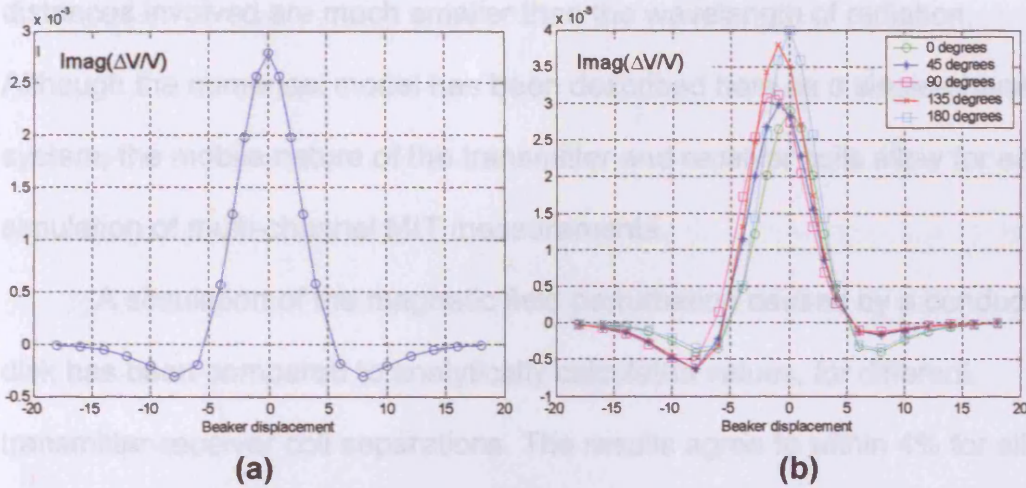


Figure 2.19. The simulated change in the imaginary part of $(\Delta V/V)$ caused by the introduction of an insulating rod (a) at the centre of the beaker, and (b) at five other positions.

For all six positions of the insulating rod, the change in the imaginary part of

$\frac{\Delta V}{V}$ is between 0.003 and 0.004. In order to obtain good MIT images of

structures causing changes of this magnitude, the ability to measure to 1% of this value may be required. For an MIT system employing direct phase measurement, this equates to phase resolution of 3 millidegrees.

2.6. Summary and conclusions

The governing equations for MIT have been presented. A finite-difference MIT system model that solves these equations has been described. The model consists of a moveable transmitter coil that induces eddy currents in a finite-difference grid (used to represent biological samples). The perturbation in the

receiver coil emf due to these eddy currents is calculated. The model uses a quasi-static approximation that neglects the propagation properties of electromagnetic waves, and is valid for situations where the typical interaction distances involved are much smaller than the wavelength of radiation. Although the numerical model has been described here as a single-channel system, the mobile nature of the transmitter and receiver coils allow for easy simulation of multi-channel MIT measurements.

A simulation of the magnetic field perturbation caused by a conducting disk has been compared to analytically calculated values, for different transmitter-receiver coil separations. The results agree to within 4% for all values of separation, illustrating the realistic performance of the numerical model. Further comparison has been made between simulated and experimental measurements, for single channel measurements made on beakers of tissue-equivalent saline solution. The peak values of the $\text{imag}\left(\frac{\Delta V}{V}\right)$ curves produced when the beaker was scanned horizontally between the coils agree for simulation and experiment to within 14%. The good agreement between the numerical model results and both the analytical and experimental values confirms that this numerical model provides an accurate simulation of an MIT system.

Increased understanding of the mechanism behind a feature of the experimental results has been provided by the numerical model. The simulated and experimental curves mentioned above displayed a change of sign at a certain horizontal displacement of the sample. Simulated magnetic field line plots illustrated that this feature was due to a change in direction of

the magnetic flux linking the receiver coil. Insights such as this show the usefulness of having an MIT system simulation.

The magnetic field phase change resolution required by a biomedical MIT system has been estimated. Simulations calculating the phase change caused by the insertion of an insulating rod into a beaker of tissue-equivalent saline solution, estimated the phase resolution required to be of the order of 3 millidegrees (for direct phase measurement). Such a small resolution poses a significant technological challenge to MIT measurement and signal processing hardware design (at 10MHz this is equivalent to measuring time of the order of picoseconds).

The numerical model described in this chapter will be referred to as the Cardiff MIT model from this point onwards. It is used as the foundation of the image reconstruction work described in the following chapters.

The work described in this chapter has been published as Morris *et al* (2001).

2.7. References

Armitage DW, LeVeen HH, Pethig R, 1982, Radiofrequency-induced hyperthermia: computer simulation of specific absorption rate distributions using realistic anatomical models. *Phys. Med. Biol.*, vol. **28**, no. 1, p. 31-42

Gencer NG, Kuzuoglu M, Ider YZ, 1994, Electrical impedance tomography using induced currents. *IEEE Trans. Medical Imaging*, vol. **13**, no. 2, p. 338-350

Griffiths H, Stewart WR, Gough W, 1999, Magnetic induction tomography: a measuring system for biological tissues. *Annals of NY Acad. Sci.*, vol. **873**, pp. 335-45

Morris A, Griffiths H, Gough W, 2001, A numerical model for magnetic induction tomographic measurements in biological tissues. *Physiol. Meas.*, vol. **22**, p. 113-9

Press WH, Flannery BP, Teukolsky SA, Vetterling WT, 1989, Numerical Recipes for Fortran, Cambridge University Press

Sadiku MO, 1992, Numerical Techniques in Electromagnetics, CRC Press

Shadowitz A, 1975, The Electromagnetic Field, Dover NY

3. A linear reconstruction algorithm for MIT

3.1. Introduction

This chapter describes a linear reconstruction algorithm for MIT, and its initial evaluation using simulated measurements. The Cardiff MIT model described in chapter 2 is used to calculate MIT and EIT sensitivity matrices and simulated measurements. Comparisons are made between MIT and EIT images using a linear reconstruction algorithm based on inversion of the sensitivity matrix. Use of the same forward solver in calculating the sensitivity matrix and simulated measurements is often referred to as an inverse crime, but is considered here to be the most favourable test of the reconstruction algorithm (i.e. if image reconstruction is unsuccessful here, it is unlikely to be successful with measurements simulated using a different forward solver).

3.2. Non-linearity

The equations describing the eddy currents induced in a sample during a typical MIT measurement (2.1.9 and 2.1.14) are reproduced here for convenience as 3.2.1 and 3.2.2. For simplicity, the complex conductivity σ^* will be considered as real (σ), i.e. the imaginary part containing relative permittivity is neglected.

$$\mathbf{E} = -\nabla\phi - j\omega\mathbf{A} \quad (3.2.1)$$

$$\mathbf{J} = \sigma\mathbf{E} \quad (3.2.2)$$

Non-linearity in MIT arises from the fact that the conductivity gradients inside the sample cause non-zero electric scalar potential gradients ($\nabla\phi$). The electric field \mathbf{E} is consequently a function of conductivity, leading to a non-linear relationship between the current density \mathbf{J} and the conductivity.

Equation (3.2.2) would be more accurately written as

$$\mathbf{J} = \sigma \mathbf{E}(\sigma) \quad (3.2.3)$$

This in turn leads to a non-linear relationship between the measured receiver coil emfs V and the conductivity of the sample.

$$V = A(\sigma)\sigma \quad (3.2.4)$$

For small changes in the sample's conductivity $\Delta\sigma$, the relationship between receiver coil emf and conductivity can be linearized

$$\Delta V = S\Delta\sigma \quad (3.2.5)$$

where ΔV is the change in V caused by $\Delta\sigma$. In matrix form, S is known as the Jacobean, or sensitivity matrix. The calculation of the sensitivity matrix is described in 3.3.

3.3. Linear reconstruction algorithm

A linear reconstruction algorithm, based on the inversion of a sensitivity matrix using singular value decomposition, has been developed to reconstruct images of conductivity and permittivity from MIT measurements.

3.3.1. Sensitivity matrix

The sensitivity matrix **S** relates perturbations in conductivity σ to resulting changes in the measured emf set **V**. Considering the discrete case, where there are m emf measurements and n conductivity regions, **S** is an m by n matrix, each element of which is given by

$$S_{ij} = \frac{V_i^{\text{pert}} - V_i^{\text{uni}}}{\sigma_j^{\text{pert}} - \sigma_j^{\text{uni}}} = \frac{\Delta V_i}{\Delta \sigma_j} \quad (3.3.1)$$

where the superscripts 'pert' and 'uni' refer to perturbed and uniform distributions, and the subscripts i and j refer to the i^{th} transmitter-receiver coil combination and j^{th} conductivity region (or image voxel – distinct from the model voxels described in chapter 2) respectively. σ_j^{pert} and σ_j^{uni} are always fixed and non-zero, such that S_{ij} is never infinite.

3.3.2. Calculation of the sensitivity matrix

The forward solver described in chapter 2 provides the method of calculating **S**:-

- a measurement set (\mathbf{V}^{uni}) for a uniform conductivity distribution (σ^{uni}) is calculated;
- the conductivity of one of the image voxels is perturbed by 1%;
- a measurement set (\mathbf{V}^{pert}) for the perturbed conductivity distribution (σ^{pert}) is calculated;
- the last two steps are repeated for all of the image voxels, allowing equation (3.3.1) to be calculated.

The simulation used to calculate the MIT sensitivity matrix included a cylindrical volume of diameter and height 24cm, having a conductivity of 1 Sm^{-1} . One 26×26 layer of this volume (a cross-section in the x-y plane, the z-direction is out of the plane of the paper) is shown in figure 3.1. The black squares represent insulating voxels, while the red squares approximate the cylinder (the outline of which is shown in blue). The relative permittivity of the cylinder was neglected (set to zero), as it is the changes due to conductivity that are of primary interest. The cylinder was encircled by 16 coils, each having a diameter of 5cm. The coils were positioned at equal intervals around the middle of the cylinder, facing it radially, and positioned 14.5cm from the cylinder axis. Each coil was assumed to be able to transmit and receive, but not at the same time, leading to $16 \times (16-1) = 240$ measurements. However, the principle of reciprocity (Geselowitz 1971, Jordan and Balmain 1968), formulated for MIT, states that the emf induced in coil A when coil B is transmitting is the same as that induced in coil A when coil B is transmitting. The consequence of this is that only half of the 240 measurements are independent, and so only 120 measurements are calculated (although it should be noted that in practical MIT systems it is still useful to record all 240 measurements and average, to reduce noise). Reciprocity pairs of simulated measurements were compared, and found to differ by less than 1%.

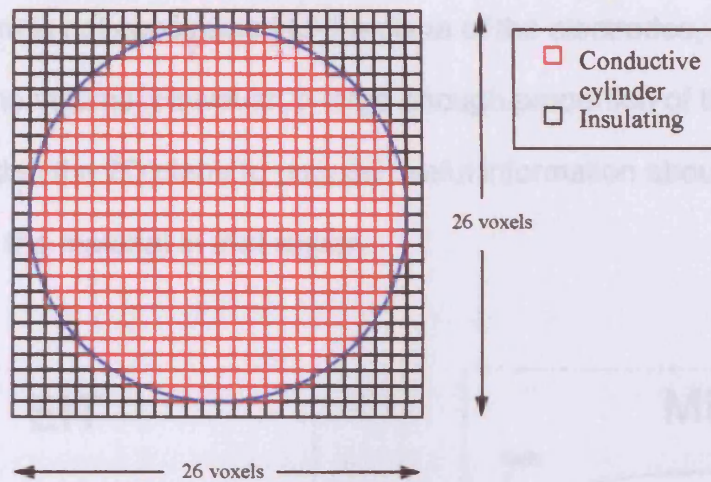


Figure 3.1. One layer of the conductive cylinder used to calculate the sensitivity matrices (the z-direction is out of the plane of the paper).

The MIT model has been reconfigured to calculate an EIT sensitivity matrix, by simulating current drive and signal measurement from adjacent electrodes. The MIT coils were replaced by 16 electrodes placed on the boundary of the cylinder. The injection of current was simulated by fixing the scalar potential of two of the electrodes during the iterative scalar potential calculation. The potentials at all of the other electrodes were recorded, and used to calculate potential differences for constant injected current.

The image resolution of EIT systems is proportional to the number of independent measurements, and the limited number (104) that 16 electrode EIT systems provide would give poor volume resolution. To counter this, the assumption is made that the current flow is constrained to a two-dimensional (2D) slice through the volume. This reduction in size of the probed region improves the resolution such that useful images can be obtained. It is possible to use a sensitivity matrix calculated in 2D (figure 3.2a), with measurements made on 3D samples, to produce clinically useful images. Current injected by

an EIT system is not constrained to the plane of the electrodes, but flows throughout the volume. However, a large enough proportion of the current does flow within the 2D plane to provide useful information about the electrical properties of the material in that region.

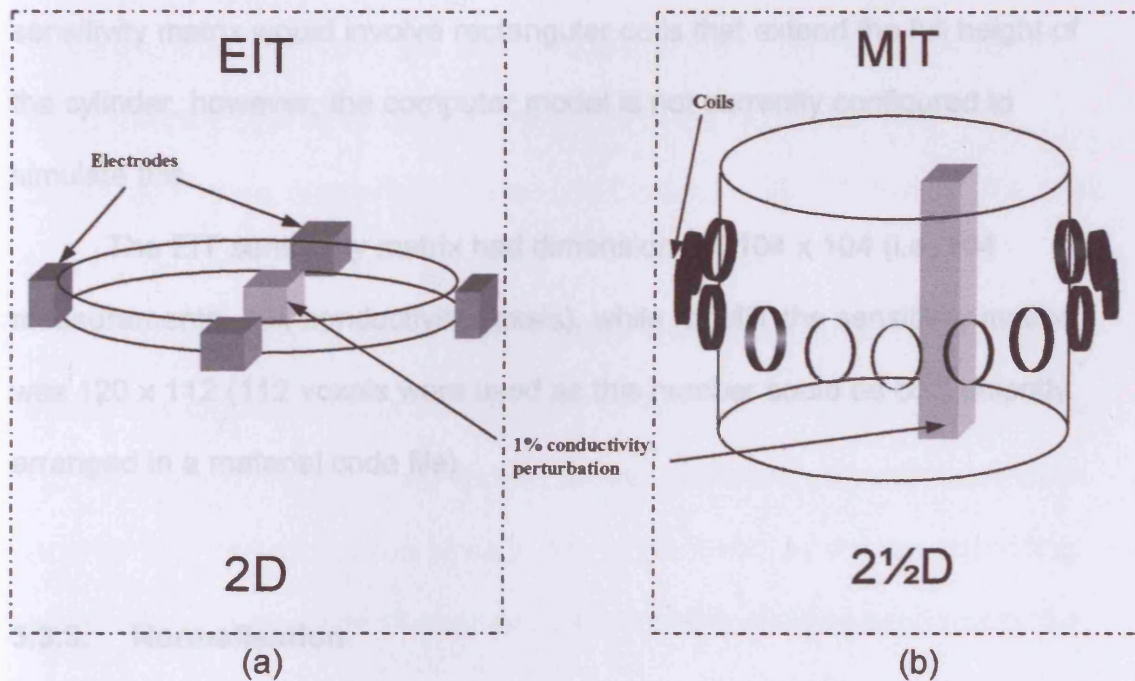


Figure 3.2. (a) 2D EIT sensitivity matrix calculation, (b) 2½D MIT sensitivity matrix calculation

For the particular case of an MIT system considered here, the current flow within the probed volume is inherently different to EIT, due to the different excitation method. The current paths are concentric with the excitation coil, and distributed much more evenly over the entire volume. The assumption of constrained current used in EIT cannot be applied to MIT, leaving the problem of unacceptably poor volume resolution. One way of circumventing this problem is to assume invariance in the z-direction, or 'full height' conductivity perturbations.

The MIT sensitivity matrix is calculated using full-height perturbations (Figure 3.2b), where the conductivity region perturbed spans the full height of the cylindrical volume. As EIT uses a 2D sensitivity matrix, the calculation of the MIT sensitivity matrix is referred to as 2½D: the conductivity perturbations are invariant in the z-direction, but the coil geometries are not. A 2D MIT sensitivity matrix would involve rectangular coils that extend the full height of the cylinder, however, the computer model is not currently configured to simulate this.

The EIT sensitivity matrix had dimensions of 104 x 104 (i.e. 104 measurements, 104 conductivity voxels), while for MIT the sensitivity matrix was 120 x 112 (112 voxels were used as this number could be conveniently arranged in a material code file).

3.3.3. Normalisation

In EIT, when practical measurements are used in conjunction with simulations to produce images of conductivity, uncertainties in the electrode positions and object shape result in significant image artefacts. For example, when performing measurements on the human body it is very difficult to know the exact positions of the electrodes, and the precise shape of the body.

Sensitivity matrix calculations will often involve simplifying assumptions about the electrode positions (e.g. equidistant) and body shape (e.g. cylindrical).

The differences in simulated and actual geometry can result in artefacts in the reconstructed images.

To counter this problem, data normalisation schemes (Metherall P 1998, Brown BH *et al* 1999) have been introduced that involve dividing the difference measurements $V_{diff} = (V_{pert} - V_{ref})$ by reference measurements V_{ref} , producing the normalised measurements $V_{norm} = \frac{(V_{pert} - V_{ref})}{V_{ref}}$. These normalised measurements are less sensitive to the errors described above, due to the cancellation of those same errors in the numerator and denominator. Data normalisation also has the advantage of reducing the large dynamic range of EIT measurements.

Normalisation of the sensitivity matrix itself is also undertaken, often to ensure that all drive positions are equally sensitive (which in practice may not occur due to varying electrode contact areas). Different protocols have been used for this, including; dividing each row of the matrix by the corresponding reference measurements (Barber and Brown 1988); dividing each row of the matrix by the average of the perturbed and reference measurements (Brown *et al* 1999); dividing each matrix row by the analytically calculated reference values (Metherall *et al* 1998); and dividing each matrix element by the sum of its row, known as row normalisation (Metherall *et al* 1996).

MIT measurement coils have fixed positions, and do not suffer from motion during the measurement procedure. However, inaccuracies in coil positioning is inevitable, and one method of compensating for this is by using the $\frac{\Delta V}{V}$ values in both measurements and sensitivity matrix elements. As with data normalisation in EIT, the inclusion of a measurement in both numerator

and denominator should reduce the effect of inaccuracies in coil positioning.

This approach is used throughout the remainder of this work.

3.3.4. Singular value decomposition (SVD)

Singular value decomposition (SVD) can be used to find a 'pseudo-inverse' of an ill-conditioned matrix, such that useful information can be derived from it.

This technique (Golub and Reinsch, Press *et al*) decomposes an $m \times n$ matrix \mathbf{S} into three constituent matrices:

$$\mathbf{S} = \mathbf{U}\mathbf{W}\mathbf{Y}^T \quad (3.3.2)$$

where \mathbf{U} is an $m \times n$ unitary matrix, \mathbf{Y} is a an $n \times n$ unitary matrix, and \mathbf{W} is an $n \times n$ diagonal matrix. The diagonal elements of \mathbf{W} (w_i) are the 'singular values'; a generalised form of the more commonly known eigenvalues. The pseudo-inverse, \mathbf{S}^\dagger , is formed using

$$\mathbf{S}^\dagger = \mathbf{Y}[\text{diag}(1/w_i)]\mathbf{U}^T \quad (3.3.3)$$

As \mathbf{Y} and \mathbf{U} are unitary, their inverses are simply their transposes, while the inverse of \mathbf{W} is calculated by taking the reciprocals of the individual diagonal elements w_i . The conductivity can be reconstructed from MIT measurements \mathbf{b} using

$$\Delta\sigma = \mathbf{Y}[\text{diag}(1/w_i)]\mathbf{U}^T\mathbf{b} \quad (3.3.4)$$

where $b_i = \frac{\Delta V_i}{V_i}$. Difficulties arise when the matrix \mathbf{S} is singular or ill-

conditioned (see 3.5 for comments on ill-posedness); in the former case some of the diagonal elements will be equal to zero, in the latter some will have very small values. The condition number gives a measure of how ill-conditioned a

matrix is; this is the ratio of the largest singular value to the smallest. The larger the condition number, the more ill-conditioned the matrix is. If some of the singular values are equal to zero the condition number is infinite, i.e. the matrix is singular. Taking the reciprocal in these cases leads to the solution 'blowing-up', as would occur using the other matrix inversion methods (e.g. QR decomposition). The strength of SVD is that it is possible to eliminate the causes of this instability by setting the reciprocals of offending diagonal elements to zero. This truncation, or regularisation, of the inverted matrix gives a least-squares solution.

A plot of the log of the normalised singular values for the EIT and MIT sensitivity matrices is shown in figure 3.3. The curves are very similar, but the EIT matrix is of slightly better condition than the MIT matrix for most of the indices. The EIT singular values decay more rapidly than the MIT values above an index of 90, resulting in a larger condition number of 7.9×10^8 compared with 4.8×10^7 for the MIT matrix.

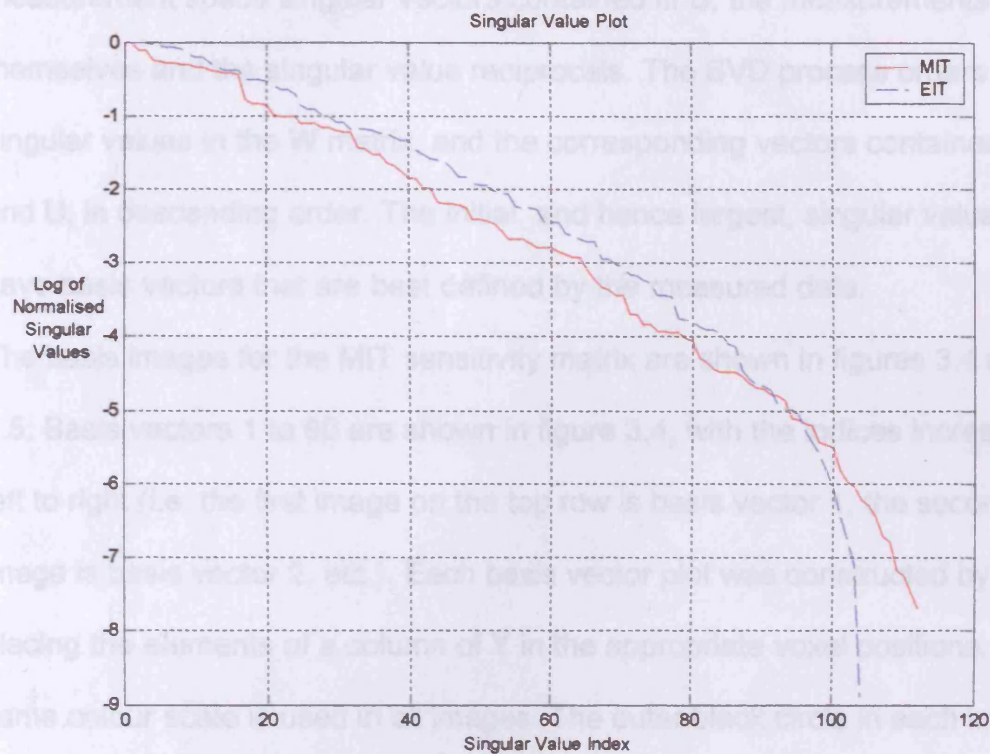


Figure 3.3. Log-normalised singular value plot for 104 x 104 EIT sensitivity matrix (blue line), and 120 x 112 MIT sensitivity matrix (red line).

3.3.5. Spectral expansion

Spectral expansion describes a conductivity distribution σ as a basis vector expansion (Zadehkoochak 1991), according to the equation

$$\sigma = \sum_{i=1}^n a_i x_i \quad (3.3.5)$$

where the x_i are the basis vectors, and the a_i are the associated coefficients.

In matrix equation form

$$\sigma = \mathbf{X}\mathbf{A} \quad (3.3.6)$$

Comparing this equation with (3.3.4) identifies the basis vectors contained in \mathbf{X} with the columns of \mathbf{Y} , and the coefficients \mathbf{A} are a combination of the

measurement space singular vectors contained in \mathbf{U} , the measurements themselves and the singular value reciprocals. The SVD process orders the singular values in the \mathbf{W} matrix, and the corresponding vectors contained in \mathbf{Y} and \mathbf{U} , in descending order. The initial, and hence largest, singular values have basis vectors that are best defined by the measured data.

The basis images for the MIT sensitivity matrix are shown in figures 3.4 and 3.5. Basis vectors 1 to 60 are shown in figure 3.4, with the indices increasing left to right (i.e. the first image on the top row is basis vector 1, the second image is basis vector 2, etc.). Each basis vector plot was constructed by placing the elements of a column of \mathbf{Y} in the appropriate voxel positions. The same colour scale is used in all images. The outer black circle in each image represents the position of the receiver coils, and is used throughout this work to emphasise that MIT is a non-contact imaging method. The slightly smaller inner black circle represents the boundary of the conductive cylinder.

Figure 3.4 shows that the initial basis vectors (those best described by the measurement data) contain more detail in the periphery of the conductivity region. As the basis vector index increases, and the corresponding singular values reduce in size, the basis vectors describe more of the central region. This trend is not surprising considering the physical situation:- the transmitter and receiver coils are closer to the periphery of the conductivity region, so both the excitation and measurement fields will be larger at the periphery than in the region's centre. Therefore, it is logical that these measurements will contain more information about the periphery than the more central regions.

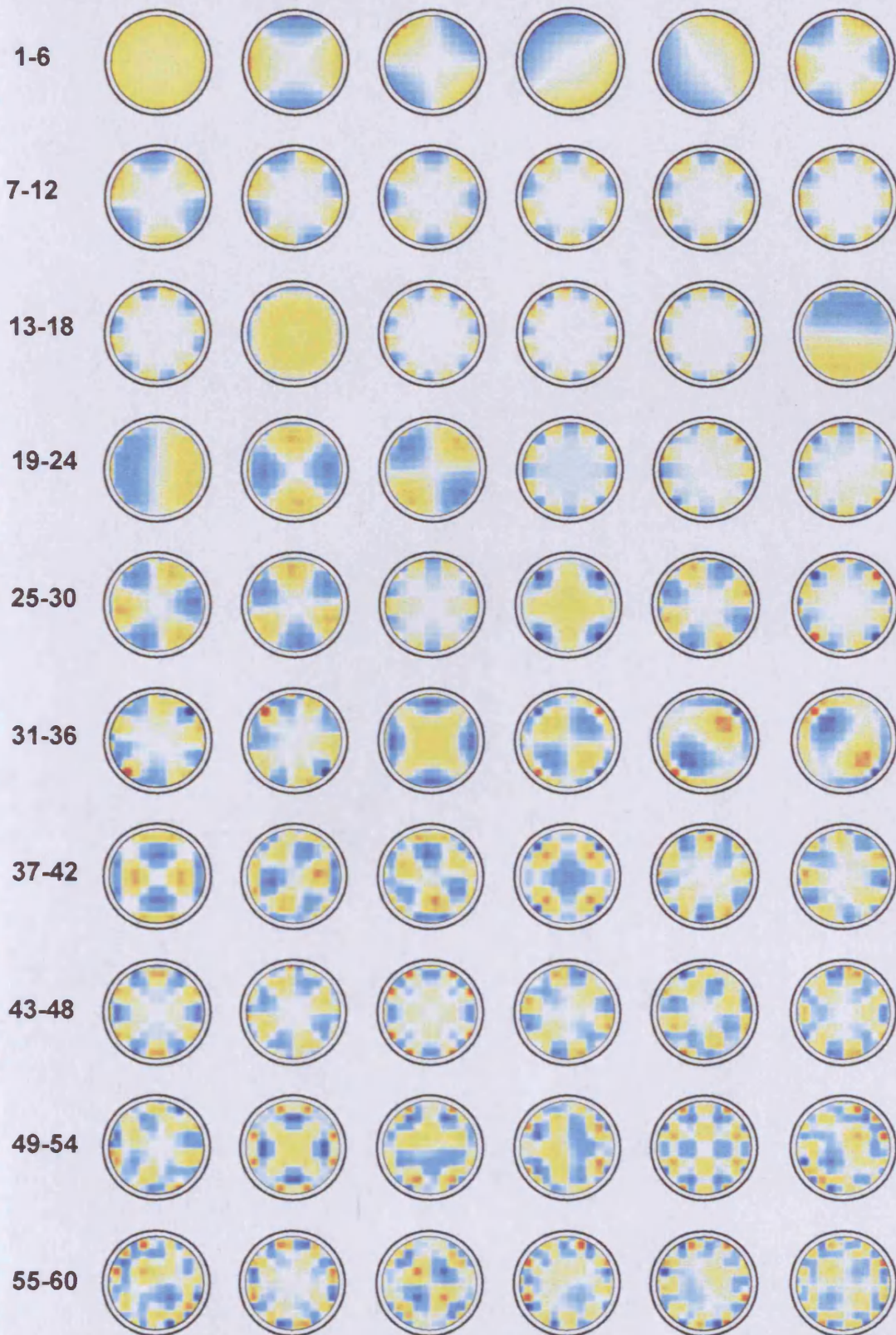


Figure 3.4. MIT basis vectors 1-60, with indices increasing left to right, ordered with respect to increasing singular values.

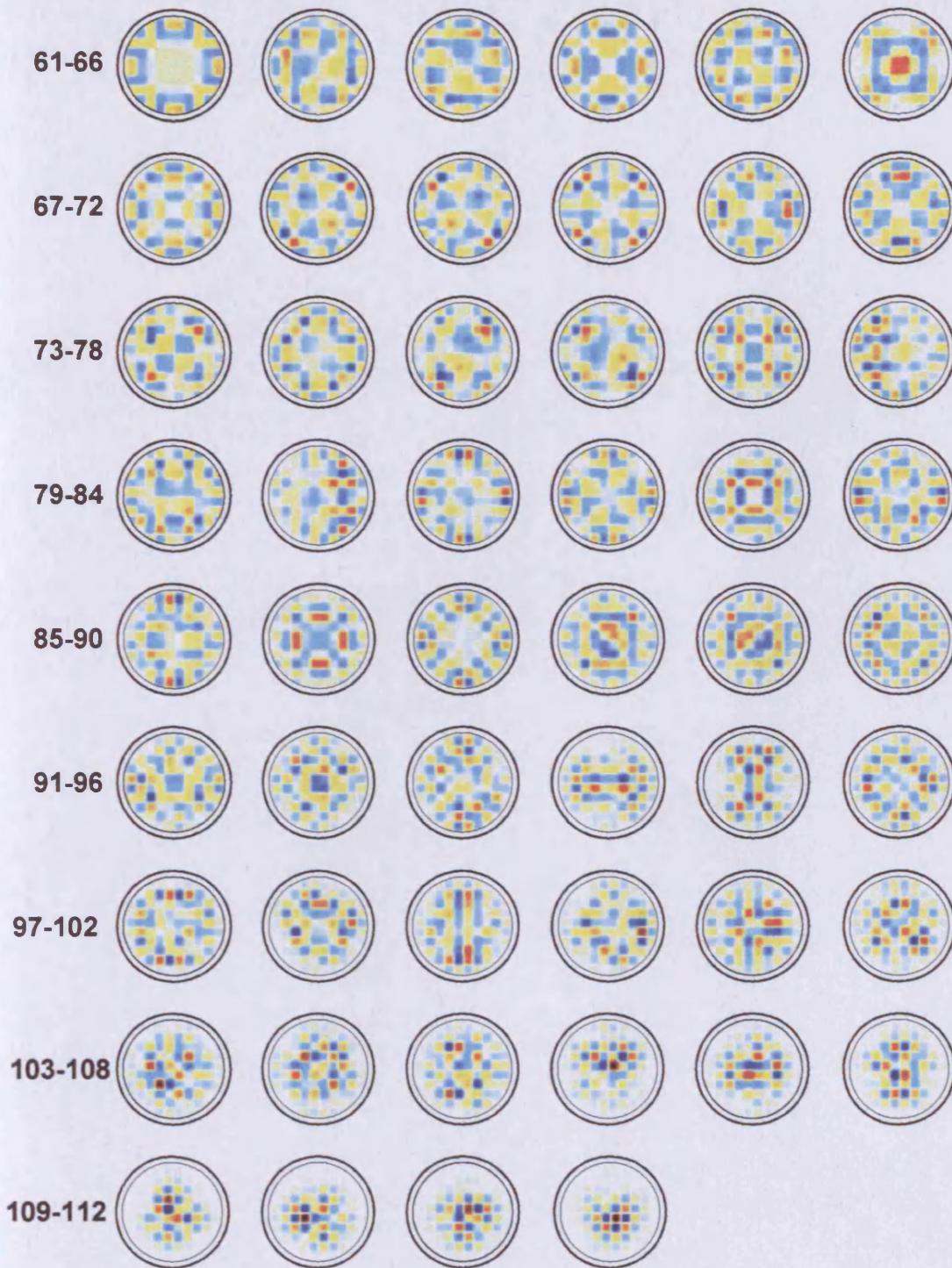


Figure 3.5. MIT basis vectors 66-112.

Spectral expansion of an EIT sensitivity matrix (Zadehkoochak 1991) has also shown this general trend, which is supported by a basis vector expansion of the EIT sensitivity matrix considered here (figures 3.6 and 3.7).

It is noticeable that the MIT basis vectors are less predictable in their order in the series than those for EIT, i.e. MIT basis vectors with low spatial frequency information occur suddenly within a sequence of higher frequency images (e.g. MIT basis image 14).

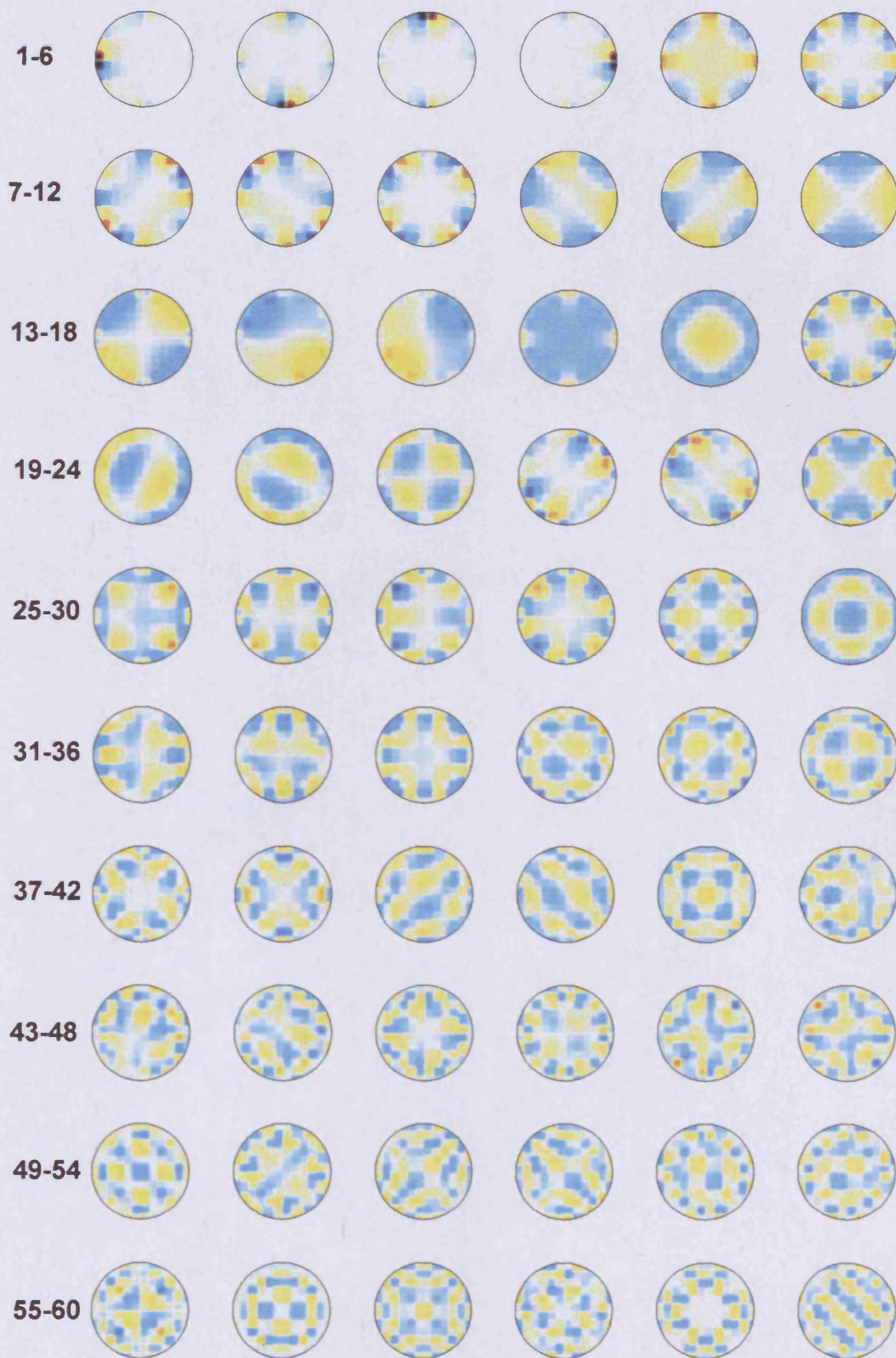


Figure 3.6. EIT basis vectors 1-60.

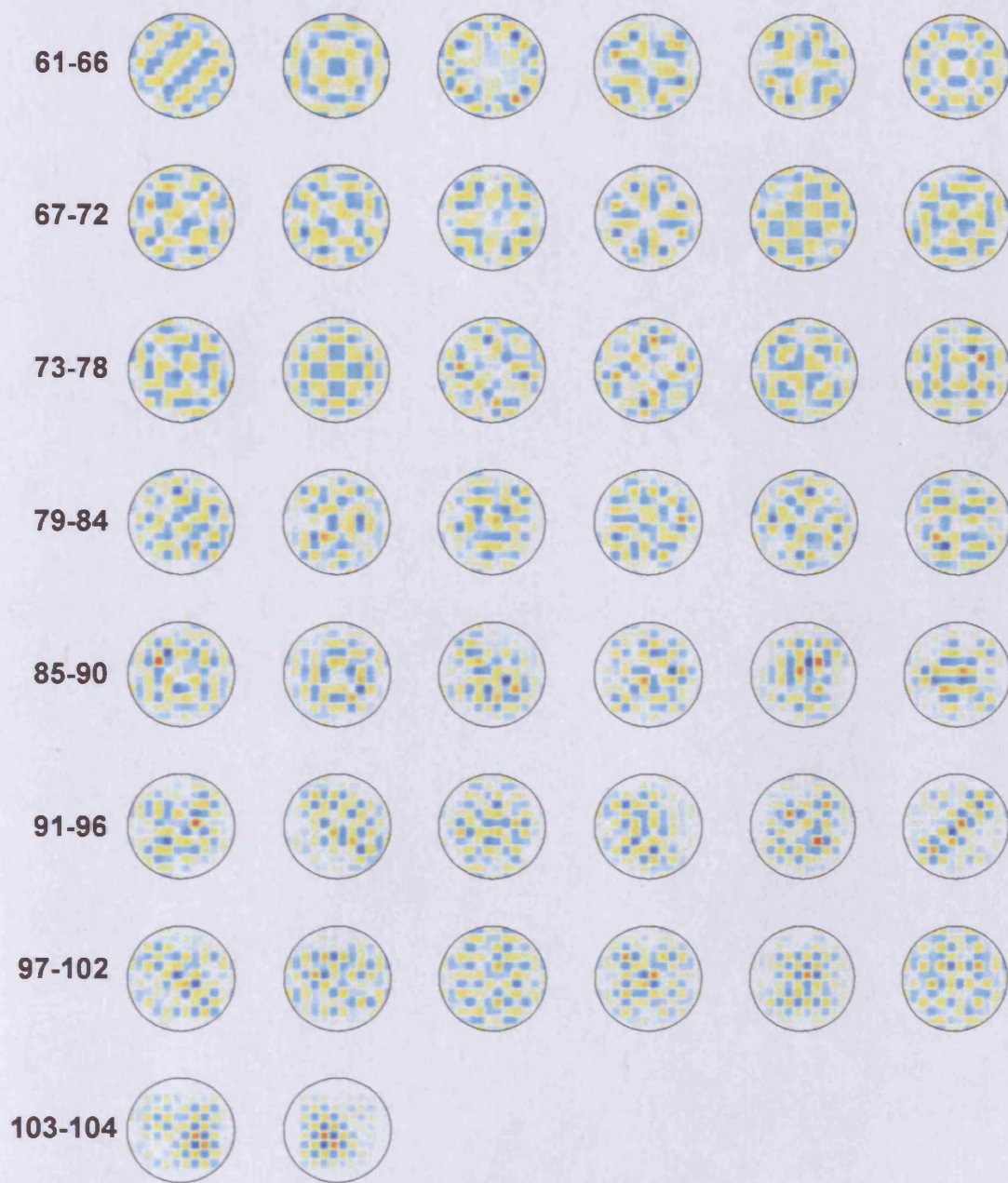


Figure 3.7. EIT basis vectors 61-104.

3.4. Comparing linear image reconstruction in MIT and EIT via simulations

3.4.1. Simulating EIT and MIT measurements

The Cardiff MIT model has been used to simulate both MIT and EIT measurements, for the purpose of testing the linear reconstruction algorithm described previously in this chapter. As mentioned in 3.1, the fact that the model has been used to calculate the sensitivity matrix and simulated measurements is often referred to as an 'inverse crime'. This term is used because the lack of differences that occur between calculated sensitivity matrix elements and experimental measurements results in a deceptively good imaging performance.

It is considered here to represent the most favourable test of the image reconstruction algorithm (mitigating this inverse crime is by the introduction of simulated noise is considered in 4.2.2.3).

3.4.2. Limited height conductivity perturbations

EIT and MIT measurements were simulated for 2cm^3 10% conductivity perturbations located within a 1 S/m conductive cylinder. The perturbations were located at three different positions (A, B, C) in the x-y plane (figure 3.8), and at three different heights; at $z = 0\text{cm}$, 3cm and 6cm above the electrode/coil plane (the mid-point of the cylinder). The z-direction is defined to be out of the plane of the paper. This gave a total of nine different positions within the cylindrical volume. The same simulation parameters (e.g. finite-

difference grid size, coil positions) were used as for the calculation of the sensitivity matrices in 3.3.2.

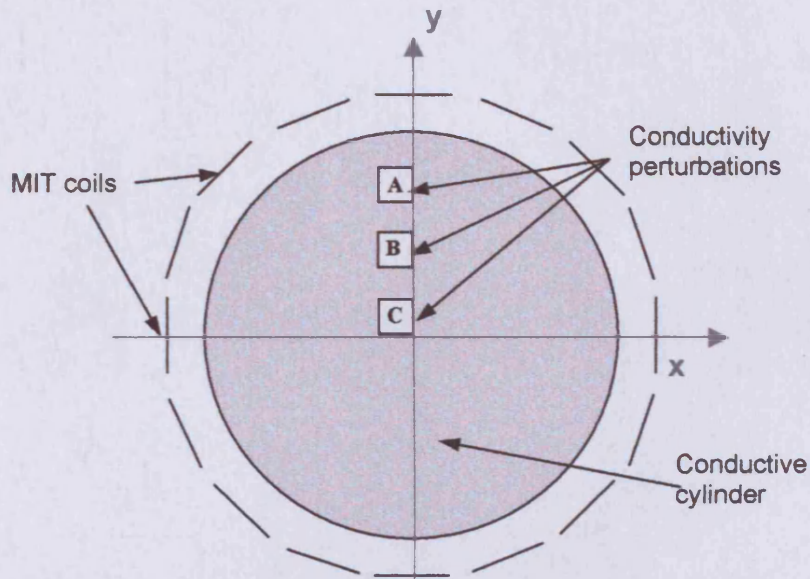


Figure 3.8. The x-y positions A, B and C of the 10 % conductivity perturbations.

The images reconstructed from the simulated EIT measurements are shown in figure 3.9. The top row of images is for x-y positions A, B and C at height 0cm, the next row for height 3cm and the next for 6cm. 70 singular values are used in all of the reconstructions. For the perturbation in the plane of the electrodes (top row), the perturbation is reconstructed clearly at position A, but becomes more blurred for positions B and C. As the perturbation is located further out of the electrode plane (2nd and 3rd rows), the reconstructed feature is shifted toward the centre of the image.

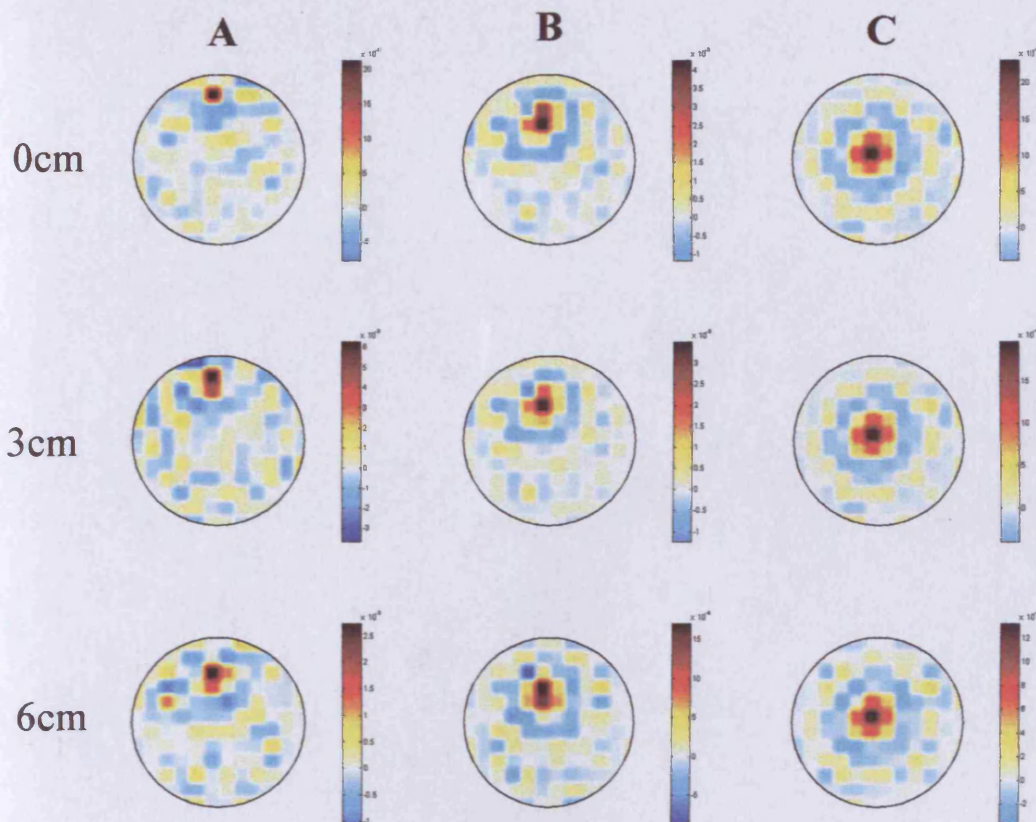


Figure 3.9. EIT conductivity images of a 10% perturbation located at positions A, B and C in the x-y plane (left to right), and at heights of 0cm, 3cm and 6cm above the plane of the electrodes. 70 singular values were used in all images.

The corresponding images for MIT are shown in figure 3.10. Here, 65 singular values were used for all images. Unlike the EIT simulations, the MIT perturbation is of comparable magnitude to the image artefacts, and cannot be clearly distinguished in any of the images.

This failure of MIT to reconstruct images of limited height conductivity perturbations is perhaps unsurprising given the 'full height' nature of the sensitivity matrix image voxels.

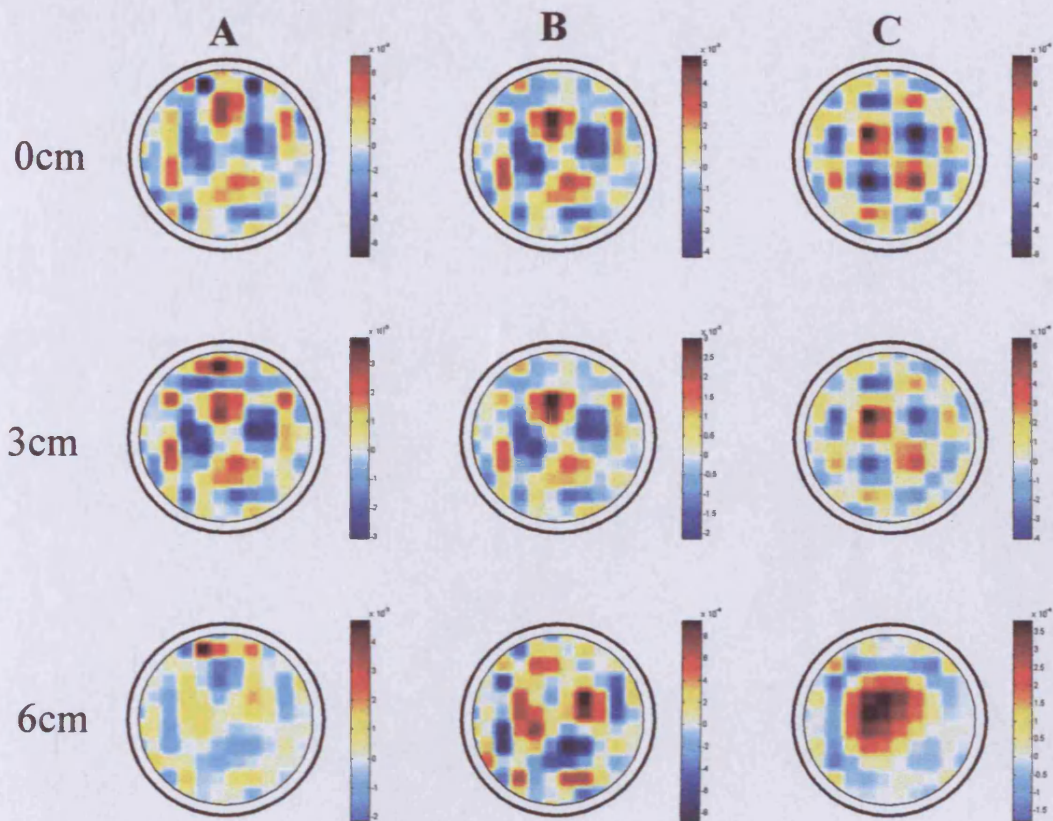


Figure 3.10. MIT conductivity images of a 10% perturbation located at positions A, B and C in the x-y plane (left to right), and at heights of 0cm, 3cm and 6cm above the plane of the coils. 65 singular values were used in all images.

3.4.3. Full height perturbations

As it is not possible to reconstruct MIT images of limited height conductivity perturbations successfully, perturbations which extend the full height of the conductivity cylinder (figure 3.11) are considered here. Again, the positions A, B and C (as defined in figure 3.8) were used.

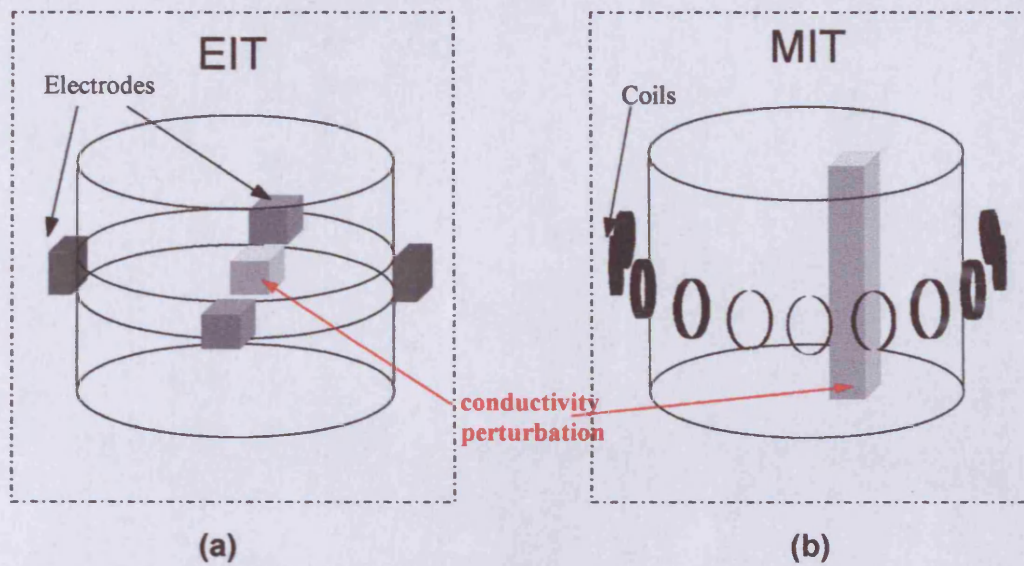


Figure 3.11. (a) Simulated 3D EIT measurements, (b) simulated 'full height perturbation' MIT measurements.

3.4.3.1. Variation of image quality with perturbation position

Images reconstructed from the simulated MIT measurements described above are shown in figure 3.12. The EIT images for the perturbation in the plane of the electrodes (top row, figure 3.9) are reproduced in the top row for convenient comparison. The MIT conductivity images for the 10% perturbation at positions A, B and C occupy the bottom row. 70 singular values were used in all three EIT reconstructions, while 80 were used for MIT. These values were found to give the best all-round reconstructions for EIT and MIT respectively. Each image uses a different conductivity scale.

The MIT images of full height conductivity are much clearer than the limited height perturbation images (3.4.2). As with EIT, the perturbation becomes blurred as its location nears the centre of the detector volume, but the effect is more pronounced for MIT.

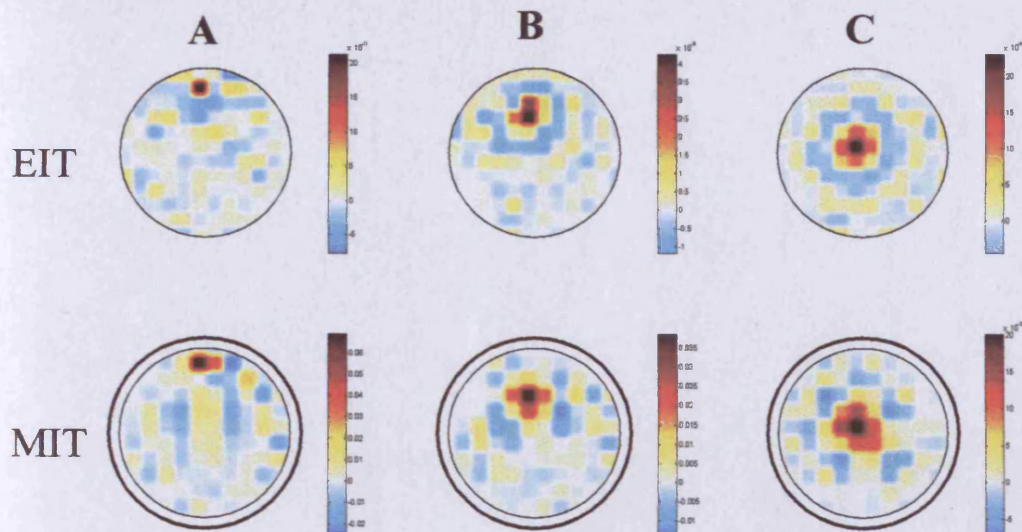


Figure 3.12. Images reconstructed from simulated EIT and MIT conductivity measurements, for a 10% perturbations at positions A, B and C (left to right). The EIT images (top row) are of a 2cm^3 perturbation in the plane of the electrodes, while for MIT (bottom row) the perturbation is the full height (24cm) of the cylinder. 75 singular values were used in the EIT reconstruction, 80 for MIT. Each image has a separate conductivity scale.

3.4.3.2. Variation of image quality with sensitivity matrix regularisation

The removal of some of the singular values from the reconstruction process has a stabilising effect on the image, but this leaves the question of how many singular values should be used. Figure 3.13 shows a 10% perturbation at position B, for MIT, reconstructed using different numbers of singular values (shown on each image). It is evident from this figure that for small numbers of singular values used, the reconstructed perturbation is smeared over its actual position. This is due to the corresponding basis images containing only coarse detail – the finer detail provided by the higher index basis images has been discarded with the zeroing of the corresponding singular value reciprocals. As the number of singular values used is increased, the image of the perturbation becomes sharper; however the image artefacts also become

more prominent. The inclusion of the majority of the singular values leads to the image of the perturbation being swamped by the image artefacts.

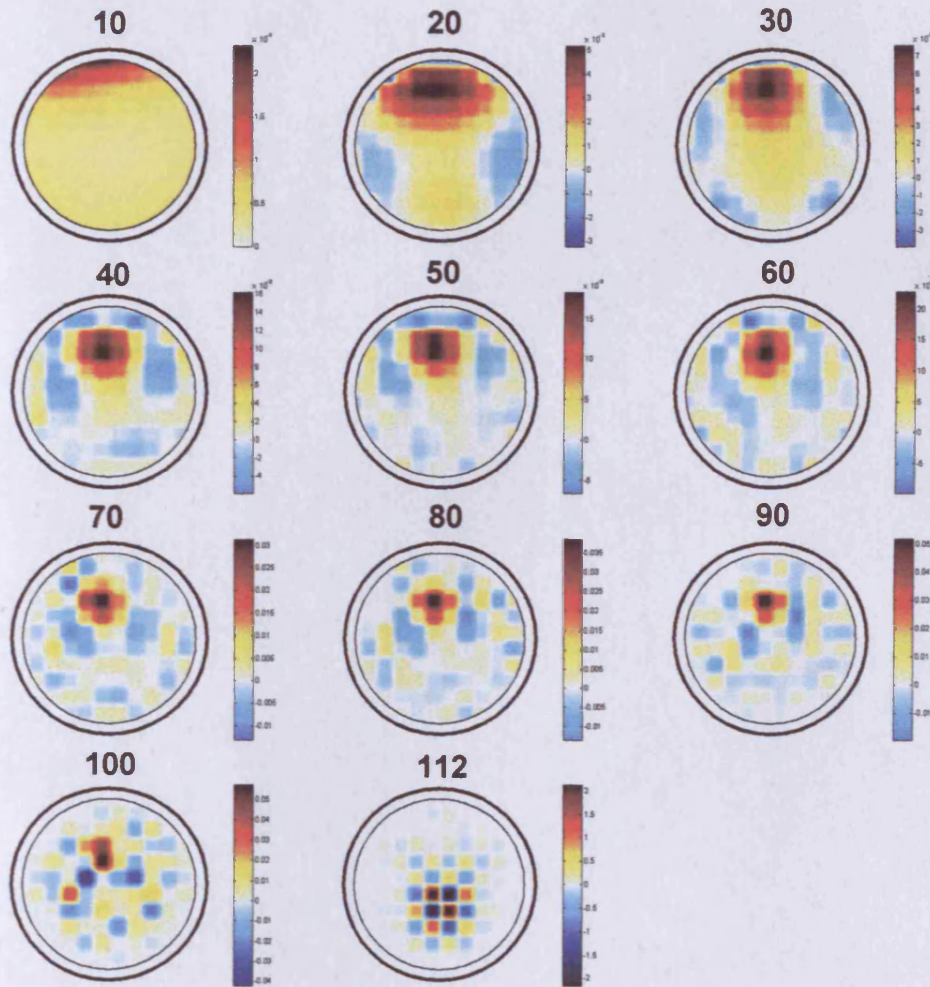


Figure 3.13. MIT images reconstructed using different numbers of singular values (shown on each image), for a 10% column perturbation at position B.

From Figure 3.13, it would appear that 90 singular values is close to the optimum value for a 10% perturbation at position B.

Figure 3.14 shows a 10% EIT perturbation at position B, reconstructed using different numbers of singular values. This illustrates the same trend as MIT, i.e. that of an initially smeared image gradually sharpening before being swamped by image artefacts.

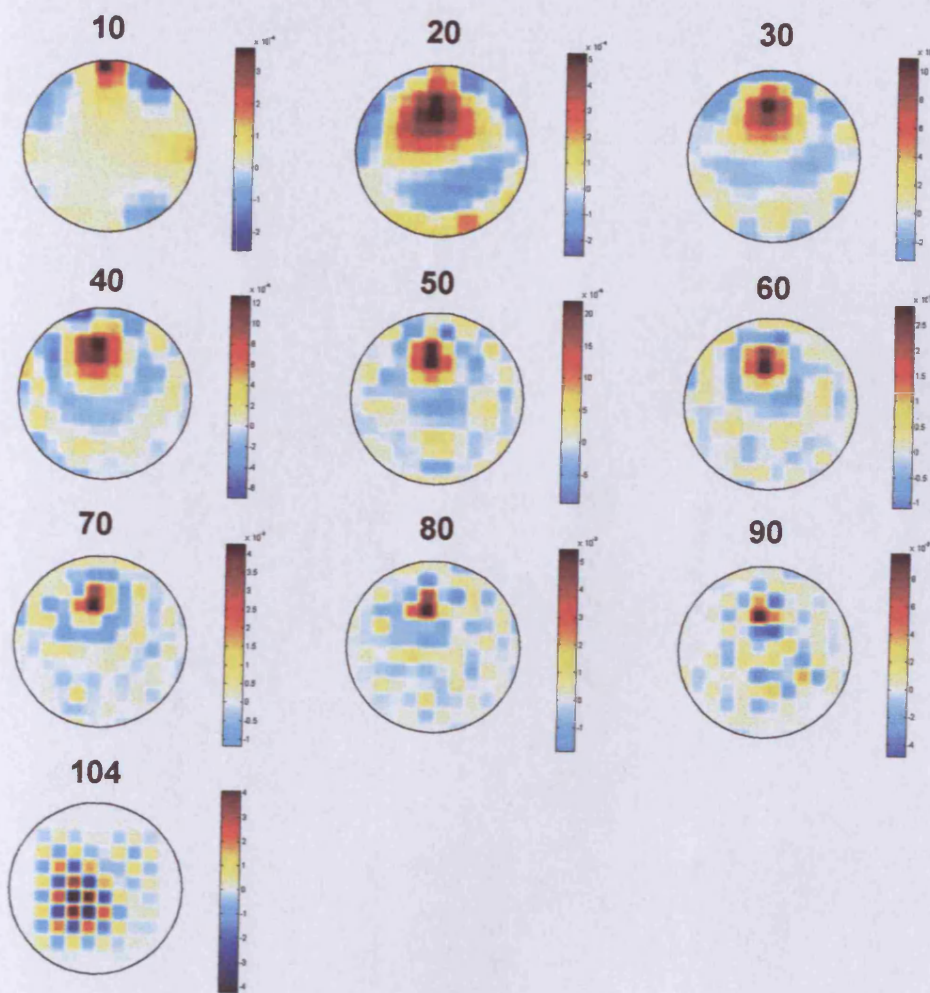


Figure 3.14. EIT images reconstructed using different numbers of singular values (shown on each image), for a 10% perturbation at position B.

3.4.3.3. Variation of image quality with conductivity magnitude

The sensitivity matrix is a linear approximation of the relationship between receiver coil emfs and conductivity, i.e. is valid for small conductivity perturbations. The effect of imaging larger conductivity perturbations is investigated using figure 3.15. This shows MIT images reconstructed for different conductivity amplitudes (shown in % on each image) at position B, using the largest 80 singular values.

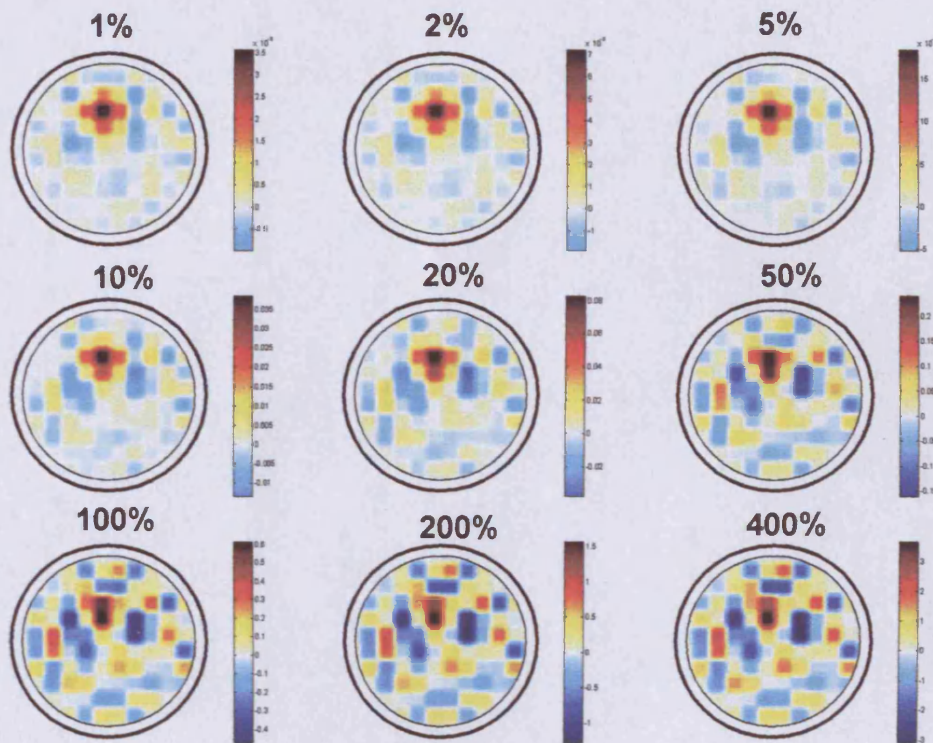


Figure 3.15. MIT images of conductivity perturbations (at position B) of different amplitudes (shown in % on each image), reconstructed using 80 singular values.

For perturbations up to 20%, the perturbation feature is reconstructed with minimal artefacts. Larger perturbations introduce significant image artefacts, due to the departure from the linear region.

It is interesting to note that this is not the case for the equivalent EIT images (figure 3.16). Here, the reconstruction method works as well for 1% perturbations as it does for 400% perturbations, leading to the conclusion that the EIT reconstruction algorithm is much less sensitive to variations in conductivity than the MIT algorithm (and hence more robust).

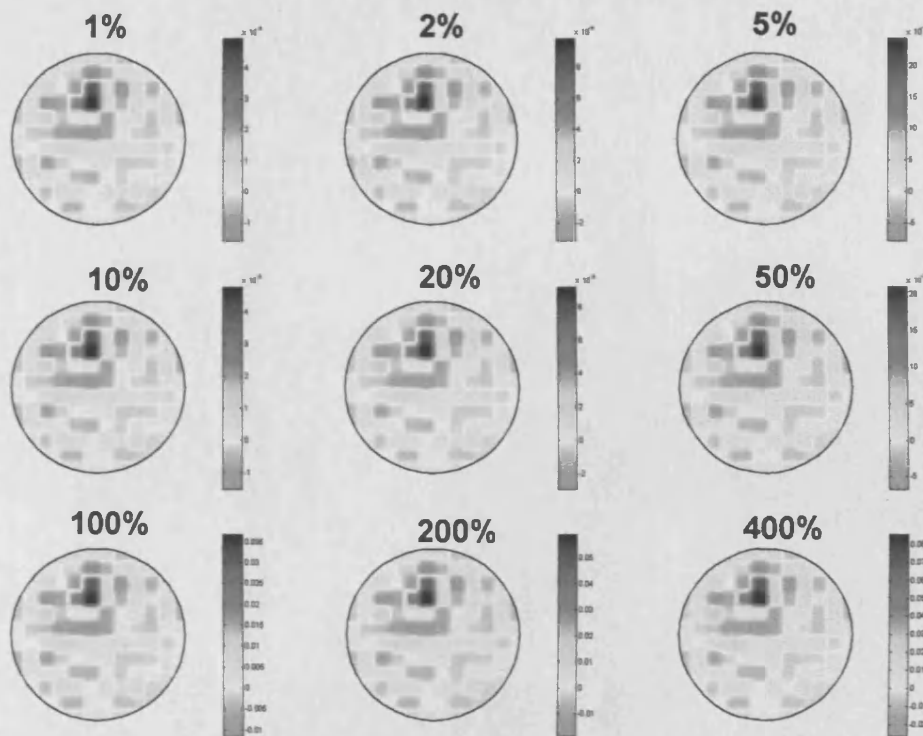


Figure 3.16. EIT images of conductivity perturbations (at position B) of different amplitudes (shown in % on each image), reconstructed using 75 singular values.

3.5. Summary and conclusions

A reconstruction algorithm for MIT (and EIT) has been presented. This algorithm uses the Cardiff MIT model (chapter 2) to calculate a sensitivity matrix, which is a linear approximation of the non-linear relationship between receiver coil emf and sample conductivity.

Inversion of the sensitivity matrix is not trivial, due to the 'ill-posed' nature of electrical imaging problems. A well-posed problem must have the following properties:- it must have only one solution for a particular datum; the solution must exist for all data considered; and a small change in the data should lead to a small change in the solution (Bertero and Boccacci 1998). If any of these three properties is not satisfied, the problem in question is

described as ill-posed. Electrical imaging problems are extremely ill-posed, leading to relatively complicated and computationally intensive methods of image reconstruction, compared with, for example, computerised x-ray tomography. This ill-posedness results in the sensitivity matrix being singular or ill-conditioned (see section 3.3.4). In these cases it does not have a 'conventional' inverse, and a solution produced by conventional matrix inversion loses physical significance.

Singular value decomposition (SVD) is a tool that allows this problem to be analysed, and indeed corrected, such that a useful solution can be obtained. It has been used to produce a pseudo-inverse of the sensitivity matrix that, when multiplied by measured emfs, reconstructs images of conductivity perturbations. Reducing the number of singular values used in the reconstruction process has the effect of regularising the solution, in effect converting an ill-posed problem into a well-posed problem.

Spectral expansion theory has enabled images of basis vectors of EIT and MIT sensitivity matrices to be produced and analysed. For both EIT and MIT, higher index basis vectors were found to include finer, and more centralised detail. A consequence of the regularisation carried out in using SVD is that some of these higher index basis vectors are removed from the image. This reduction in image information, particularly in central image regions, is likely to be the cause of the blurring effects observed in the images described in 3.4.

The images in 3.4 are of conductivity perturbations, reconstructed from simulated EIT and MIT measurements. This work suggests that the MIT sensitivity matrix described in 3.3.2 cannot successfully reconstruct images of

limited height conductivity perturbations, unlike the considered EIT sensitivity matrix. For full height perturbations however, the MIT reconstruction algorithm is able to reconstruct satisfactory images of perturbations of up to 20%.

These initial attempts at MIT image reconstruction illustrate the potential of this imaging method. This is investigated further in chapter 4. The work described in this chapter was presented in Morris and Griffiths (2001).

3.6. References

- Barber DC and Brown BH, 1988, Errors in reconstruction of resistivity images using a linear reconstruction technique. *Clin. Phys. Physiol. Meas.* **9** A101-A104
- Bertero M and Boccacci P, 1998, Introduction To Inverse Problems In Imaging, IOP Press
- Brown BH *et al*, 1999, Medical Physics and Biomedical Engineering, IOP Press
- Geselowitz DB, 1971, An Application of Electrocardiographic Lead Theory to Impedance Plethysmography. *IEEE Trans. Biomed. Eng.* **18** 38 - 41
- Golub GH and Reinsch C, 1970, Singular Value Decomposition and Least Squares Solutions. *Number. Math.* **14** 403 – 420
- Jordan EC, Balmain KG, 1968, Electromagnetic Waves and Radiating Systems, Prentice-Hall
- Meeson *et al*, 1996, Optimal filtering of EIT data in spectral expansion analysis. *Physiol. Meas.* **17** A85-A90
- Metherall P *et al*, 1996, Three-dimensional electrical impedance tomography. *Nature.* **380** 509-512
- Metherall P, 1998, Three Dimensional Electrical Impedance Tomography of the Human Thorax, PhD Thesis, University of Sheffield
- Morris A, Griffiths H, 2001, A comparison of image reconstruction in EIT and MIT by inversion of the sensitivity matrix. *Scientific Abstracts of 3rd*

International Conference of EPSRC Engineering Network on Impedance
Tomography, London, Apr. 4-6

Press WH et al, 1989, Numerical Recipes for Fortran, Cambridge University
Press

Tang M *et al*, 2002, The number of electrodes and basis functions in EIT
image reconstruction. *Physiol. Meas.* **23** 129-140

Zadehkoochak M *et al*, 1991, Spectral expansion analysis in electrical
impedance tomography. *J. Phys. D: Appl. Phys.* **24** 1911-1916

4. The imaging performance of simulated MIT systems

4.1. Introduction

The Cardiff MIT model allows the imaging performance of actual measurement systems to be evaluated, and thus the impact on this performance of any alterations to measurement system design can be easily assessed. In this chapter the Cardiff MIT measurement system (Watson *et al* 2001) is more realistically simulated than in chapter 3, and both absolute and difference images of conductivity distributions are produced using simulated measurements. Simulated random noise is added to the measurement sets, and the resulting image degradation is investigated. The basis vector content of the image reconstruction algorithm described in chapter 3 is increased, and the resulting changes in imaging performance are examined. Also, a planar MIT system is simulated, and the imaging results are compared to previously published simulation results derived from a different numerical model.

4.2. The Cardiff MIT system simulations

The imaging performance of the Cardiff MIT system will be investigated in this section using simulations. The simulated MIT system used in chapter 3 is a simplification of the Cardiff MIT system. That system simulation utilised 16 coils, each of which could transmit and receive, resulting in 120 independent measurements. The Cardiff MIT system has 16 transmit coils and 16 receive coils, mounted on the same plastic former spaced 0.8cm apart (figure 4.1).

The transmit and receive coils are positioned 13.5cm and 14.3cm from the centre of the detector volume respectively. This coil configuration theoretically provides the system with 240 independent measurements (as dictated by the theorem of reciprocity; section 3.3.2), although in practice the close proximity of the transmitter and receiver coils may reduce this value. The influence of these extra measurements on the imaging performance of the system will be investigated in section 4.2.1.1.

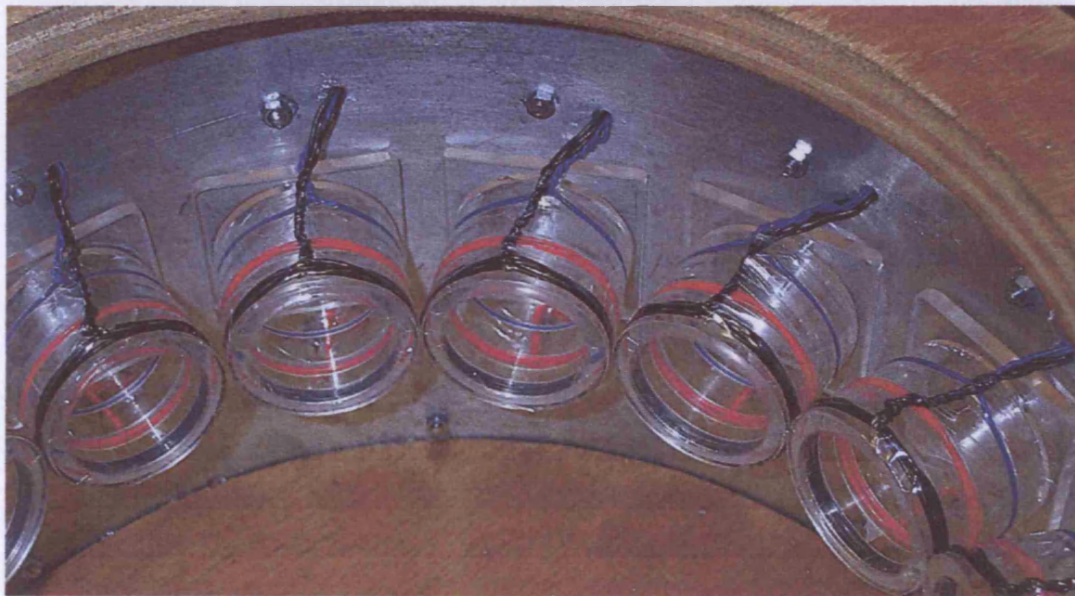


Figure 4.1. Transmit (red) and receive (black) coils wound on plastic formers within the Cardiff MIT measurement system.

An ideal MIT system would operate along the following lines:- a reference set of measurements is made on an empty detector volume; a sample is placed into the detector; measurements are made; an image of the sample's electrical properties is produced. Imaging with reference to empty space (absolute imaging) is the ultimate goal of MIT, to fully exploit its non-contacting nature. This is investigated through simulations in section 4.2.2.

Producing absolute images is challenging, and is likely to require computationally intensive reconstruction algorithms.

Another method of imaging conductivity changes involves taking measurements with reference to a conductive background (difference imaging). This approach has been used in EIT to produce images of resistivity changes in a saline bath caused by the introduction of objects of different conductivities. In MIT, the practical implementation is the same; a tank of saline solution is placed inside the detector volume, reference measurements are taken, the conductivity perturbation is introduced, and a perturbed measurement set is taken. This method can be used, in principle, to image conductivity changes that occur in the human body as a result of physiological functions. Imaging with reference to a conductive background was the method used with the simulations described in chapter 3; this work is expanded in section 4.2.1.

4.2.1. Difference imaging

4.2.1.1. Increasing the number of independent measurements

As mentioned above, the Cardiff MIT system theoretically has 240 independent measurements, twice as many as the 16 dual-coil system studied in chapter 3. However, the transmitter and receiver coils are only 0.8cm away from being at the same position (and hence like the system in chapter 3), so it is important to investigate the difference, if any, that these extra measurements make to the imaging performance of the system.

A sensitivity matrix has been simulated for the Cardiff MIT system, consisting of 16 transmitter and 16 receiver coils, all having a diameter of 5cm, located 13.5cm and 14.3cm from the system centre respectively. The sensitivity matrix was calculated for 1% perturbations on a 24cm diameter region of 1 S/m conductivity. The matrix had dimensions 240 x 112, compared with 120 x 112 for the matrix used in chapter 3. A comparison of the two matrices' log normalised singular values is made in figure 4.2.

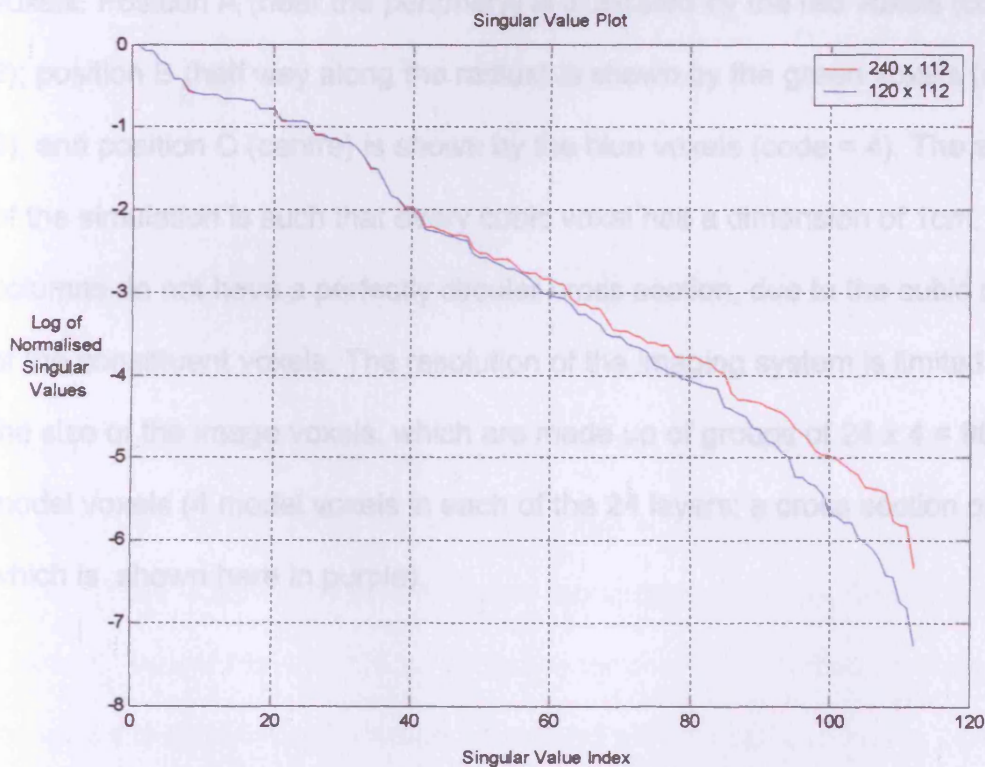


Figure 4.2. Singular value plot for 240 x 112 and 120 x 112 sensitivity matrices.

The singular value plots are practically equal until a singular value index of approximately 40. After this point the 120 x 112 matrix (blue line) singular values fall off slightly faster, indicating a slight comparative improvement in the condition of the 240 x 112 matrix for truncation levels of above 40. This

indicates that images reconstructed using the 240 x 112 matrix should be of a slightly better quality than those utilising the 120 x 112 matrix (when more than 40 singular values are used).

Reconstructions using the two matrices are compared using the following simulation. A 4cm diameter cylindrical column of the conductive region is perturbed by 10%, at three positions along the detector's radius. One layer of the cylinder is shown in figure 4.3. This is an example of part of the material code files used in the model, where numbers are used to represent voxels. Position A (near the periphery) is illustrated by the red voxels (code = 2); position B (half way along the radius) is shown by the green voxels (code = 3); and position C (centre) is shown by the blue voxels (code = 4). The scale of the simulation is such that every cubic voxel has a dimension of 1cm. The columns do not have a perfectly circular cross section, due to the cubic nature of the constituent voxels. The resolution of the imaging system is limited by the size of the image voxels, which are made up of groups of $24 \times 4 = 96$ model voxels (4 model voxels in each of the 24 layers; a cross section of which is shown here in purple).

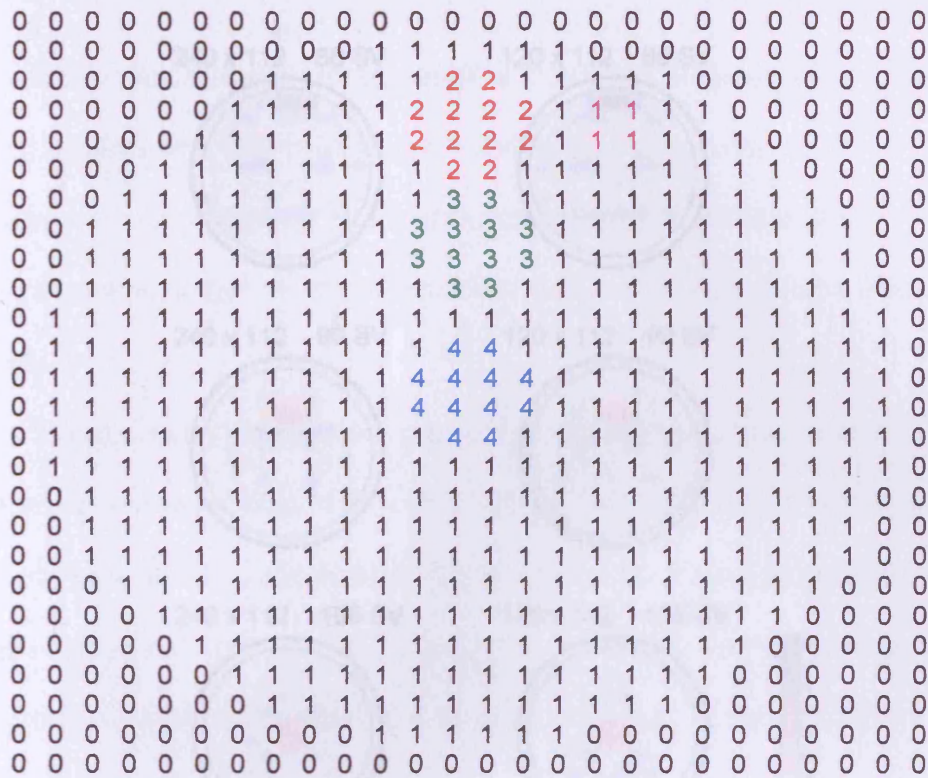


Figure 4.3. A 4cm cylindrical column (shown here as a plan view) of the conductive region is perturbed by 10% at three locations; position A shown in red; position B shown in green; position C shown in blue. A cross section of an image voxel, comprising 4 model voxels, is shown in purple.

Figure 4.4 shows the images for positions A (top row), B (middle row) and C (bottom row), for the 240 x 112 sensitivity matrix (left) and 120 x 112 matrix (right). There is little difference between the images produced by the two matrices, except that the 120 x 112 image for position C suffers from an increased level of image artefacts compared with the corresponding 240 x 112 image. Note that the shape of the cylinder is not reproduced faithfully, as the scale of detail in the cylinder (order of 1 model voxel) is smaller than the image voxel dimension in the x-y plane (4 model voxels – see figure 4.3). The improvement in image quality made by the extra measurements is minimal, as might be expected considering the small difference between the singular value plots of the two matrices (figure 4.2).



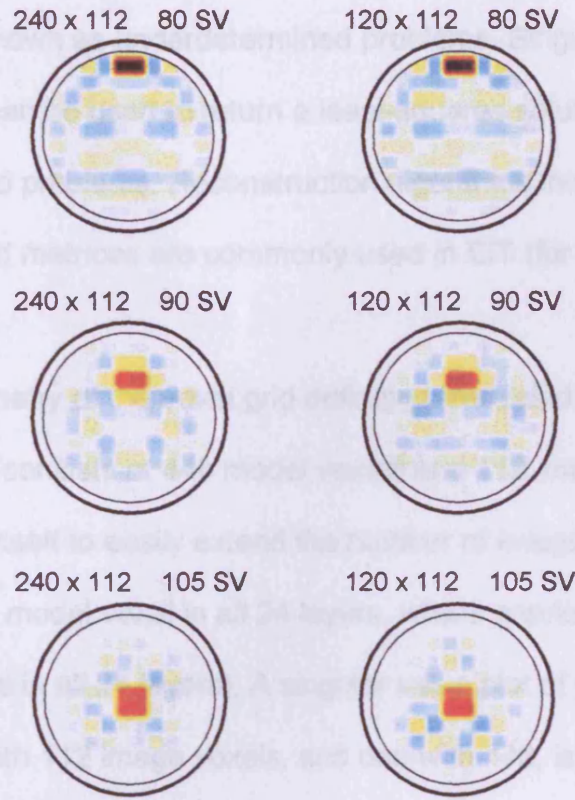


Figure 4.4. Cylinder perturbation images for 240 x 112 matrix (left) and 120 x 112 matrix (right) at three radial positions, using 80, 90 and 105 singular values respectively.

4.2.1.2. Underdetermined sensitivity matrices

By thinking of the matrix inversion problem as a solution of simultaneous equations, it would seem logical that the number of independent measurements dictates the number of basis vectors (i.e. image voxels) that should be incorporated. In other words, there should be at least the same number of equations (independent measurements) as unknowns (basis vectors) to produce a unique solution. This was the reasoning that led to 120 measurements and 112 image voxels being used in chapter 3. However, as the problem is ill-conditioned, it has no unique solution in the conventional sense, and it is possible to use simulations that have more image voxels than independent measurements. Inverse problems having more unknowns than

equations are known as underdetermined problems. Singular value decomposition can be used to return a least-squares solution to underdetermined problems. Reconstruction algorithms incorporating underdetermined matrices are commonly used in EIT (for example Meeson *et al* 1995).

The geometry of the voxel grid definition files used previously (26^3 grid, 1 layer of which consists of 448 model voxels and 112 image voxel cross sections) lends itself to easily extend the number of image voxels to 448 (1 image voxel = 1 model voxel in all 24 layers, where previously 1 image voxel = 4 model voxels in all 24 layers). A singular value plot of two sensitivity matrices, one with 112 image voxels, and one with 448, is shown in figure 4.5.

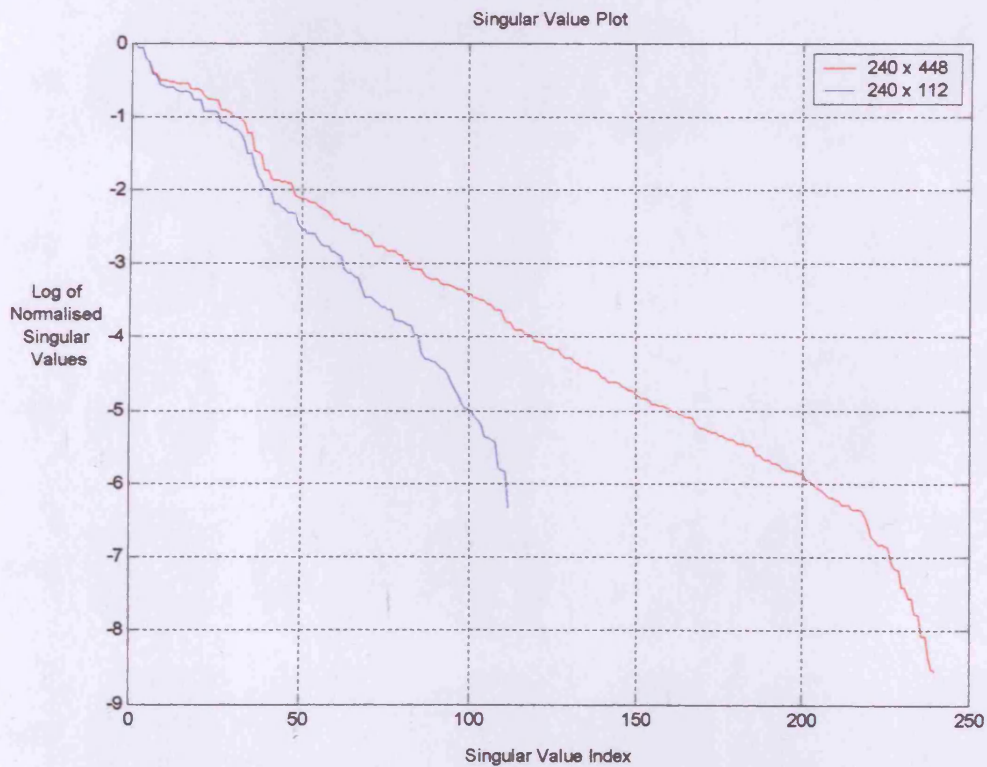


Figure 4.5. Singular value plot for 240 x 112 (blue) and 240 x 448 (red) sensitivity matrices.

The first thing that is evident from figure 4.5 is that the 240 x 448 sensitivity matrix has more singular values, and hence more basis vectors, than the 240 x 112 matrix. The rank of the 240 x 448 matrix is approximately 240, while the rank of the 240 x 120 matrix is approximately 112. The 240 x 448 matrix is of significantly better condition, taking the end of the 240 x 112 singular values (index 112) as the comparison point. An examination of the first 240 basis vectors of the 240 x 448 sensitivity matrix (figures 4.6 to 4.9) reveals much finer detail, compared to the 240 x 112 sensitivity matrix (section 3.3.5, figures 3.8 and 3.9).

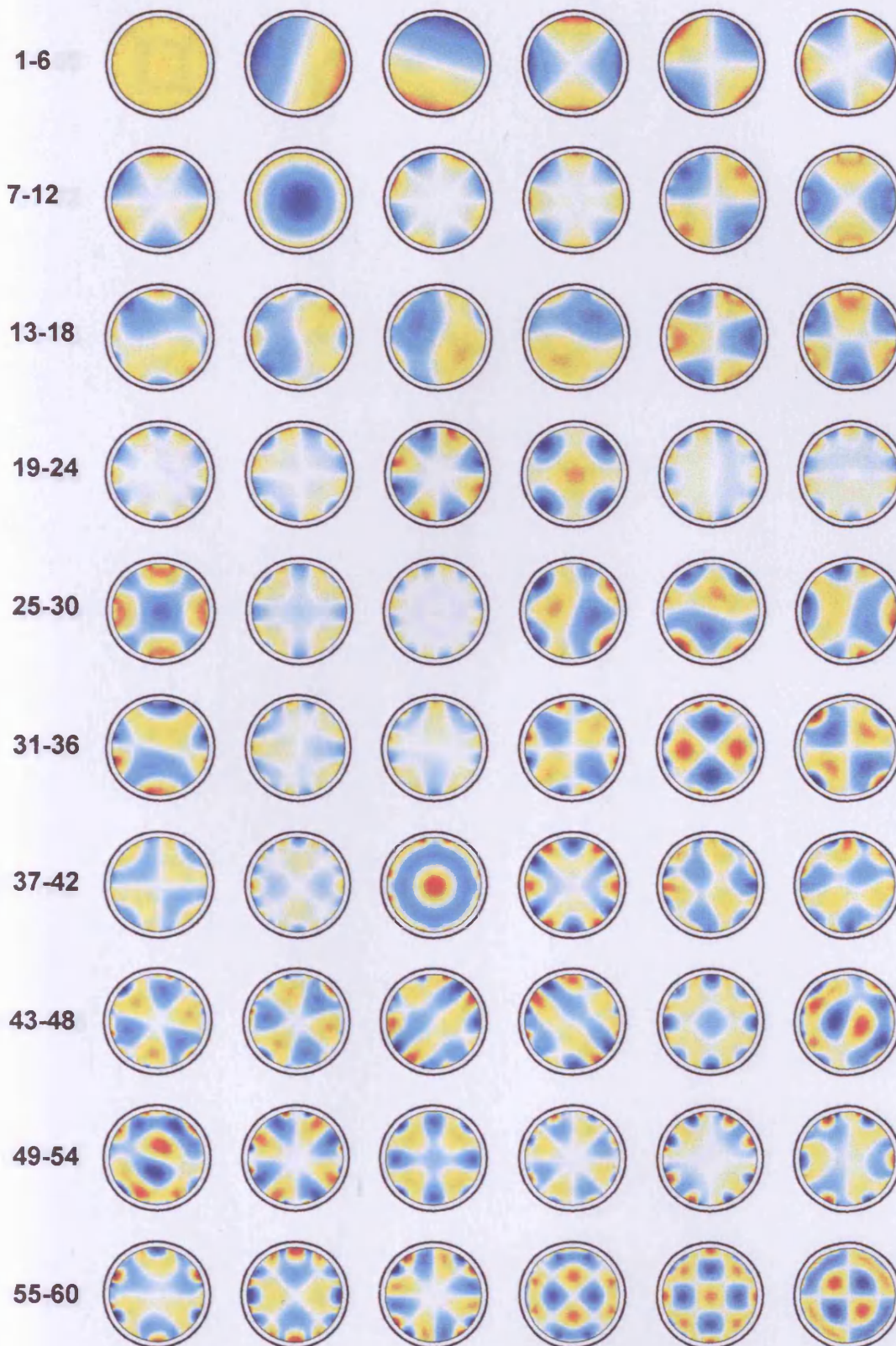


Figure 4.6. Basis vectors 1-60 of the 240 x 448 difference sensitivity matrix.

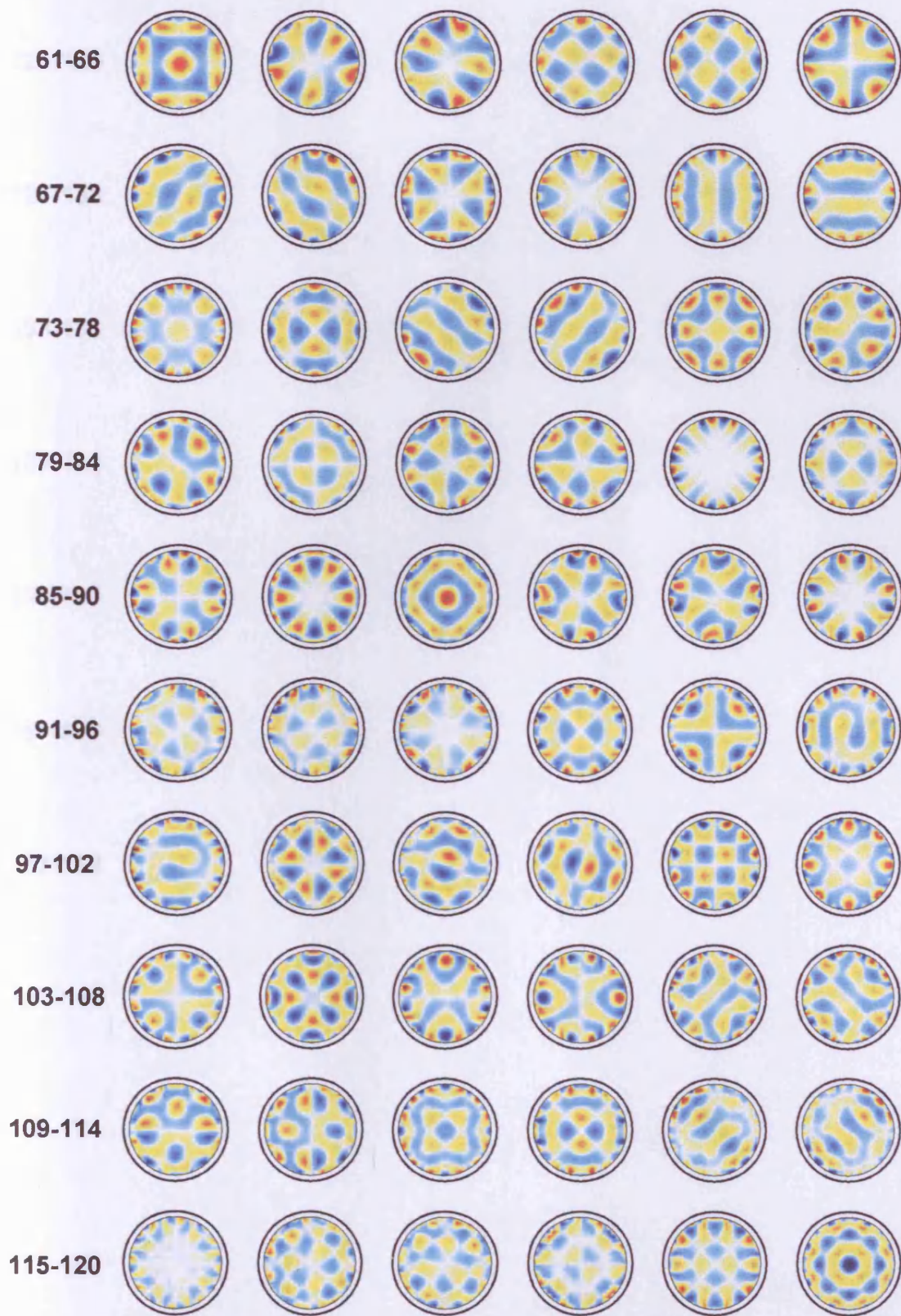


Figure 4.7. Basis vectors 61-120 of the 240 x 448 difference sensitivity matrix.

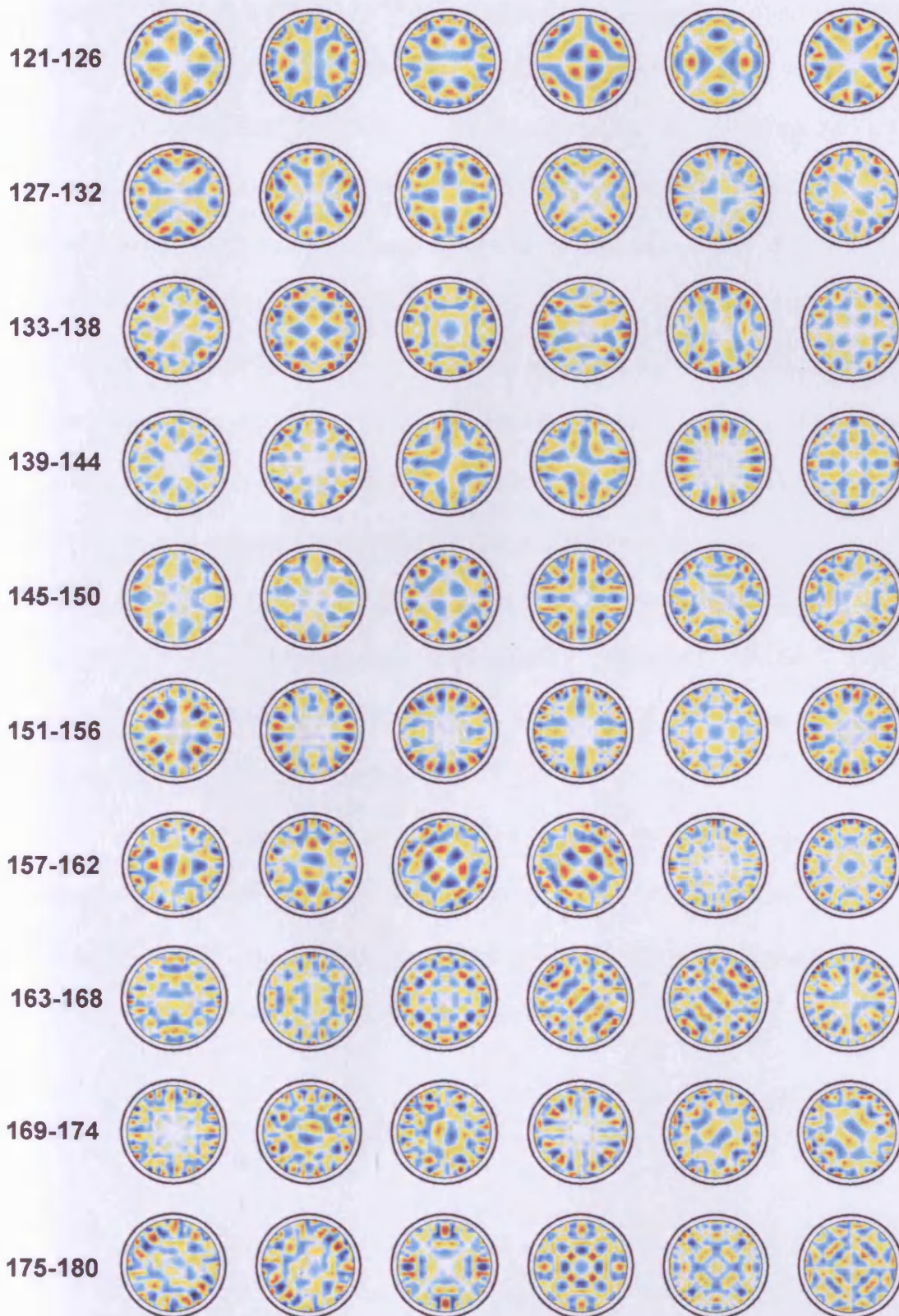


Figure 4.8. Basis vectors 121-180 of the 240 x 448 difference sensitivity matrix.

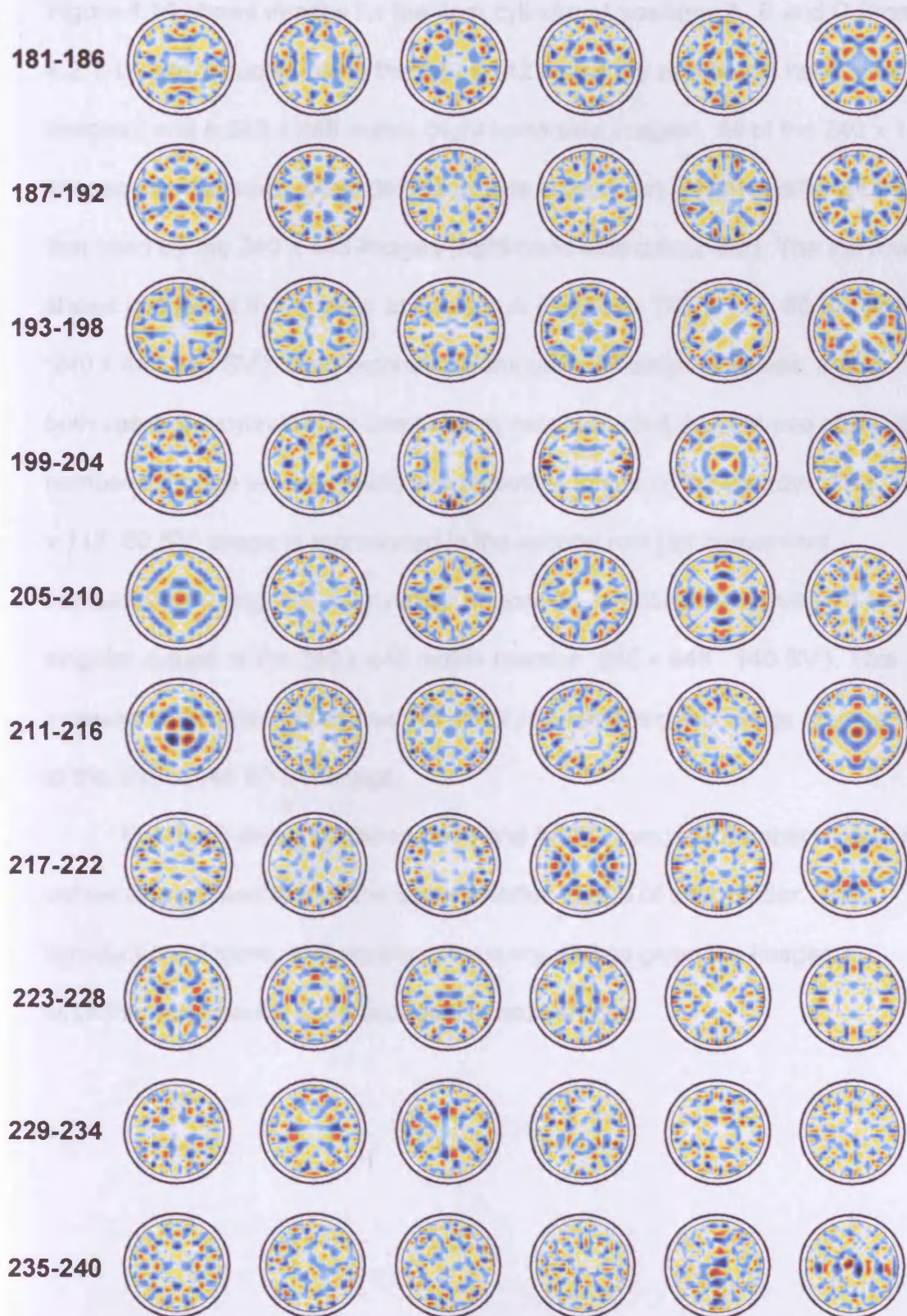


Figure 4.9. Basis vectors 181-240 of the 240 x 448 difference sensitivity matrix.

Figure 4.10 shows images for the 4cm cylinder at positions A, B and C (from 4.2.1.1) reconstructed using the 240 x 112 sensitivity matrix (left hand side images), and a 240 x 448 matrix (right hand side images). All of the 240 x 112 images use the same scale (left hand side colour-bar), which is different from that used by the 240 x 448 images (right hand side colour-bar). The top row shows images of the cylinder at position A (captions '240 x 112 80 SV' and '240 x 448 80 SV'). Both reconstructions used 80 singular values, and in both cases the cylinder has been clearly reconstructed, but the use of a larger number of image voxels results in a smoother image of the cylinder. The '240 x 112 80 SV' image is reproduced in the second row (for convenient comparison), along with the cylinder at position A reconstructed using 140 singular values of the 240 x 448 matrix (caption '240 x 448 140 SV'). This increase in singular values has the effect of sharpening the image (compared to the '240 x 448 80 SV' image).

For the B and C positions (third and fourth rows) the number of singular values was chosen to give the least distorted image of the cylinder. The introduction of more, and smaller, image voxels has given the images a smoother, and hence more acceptable, appearance.

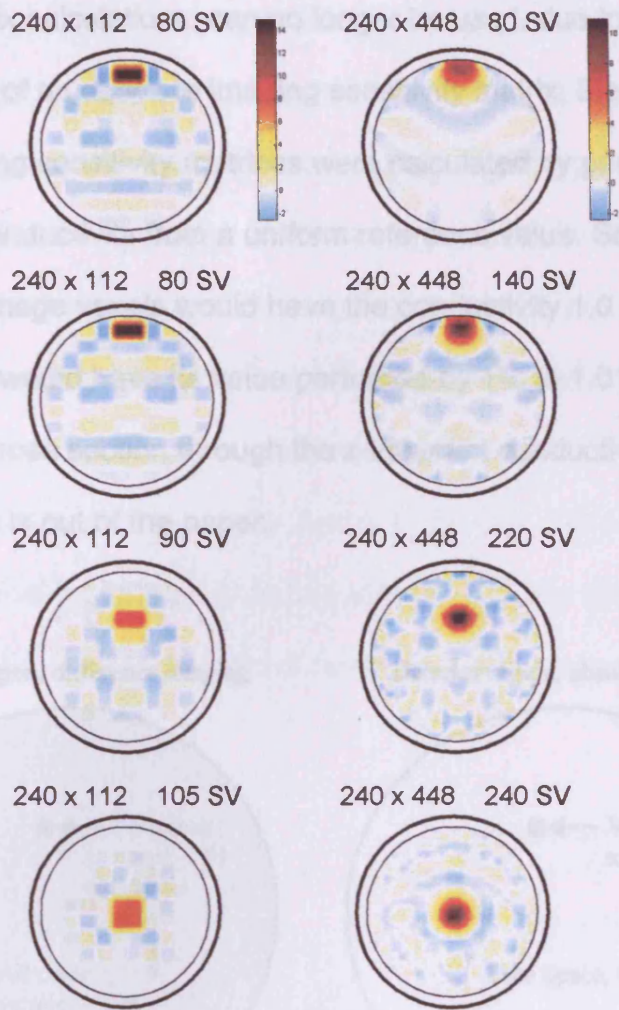


Figure 4.10. Cylinder perturbation images for 240 x 112 matrix (left) and 240 x 448 matrix (right) at positions A (top two rows), B (third row) and C (fourth row), using different numbers of singular values.

4.2.2. Imaging with reference to free-space

4.2.2.1. Introduction

As mentioned in section 4.2, the most useful MIT imaging system would be one that allowed images to be produced with reference to free-space.

Calculating a sensitivity matrix for such a system using the Cardiff MIT Model (in the manner used for the previous simulations) poses certain difficulties.

The method of using 24 model voxels to represent one image voxel, as used in previous matrix calculations, can no longer be used, due to differences in the construction of an absolute imaging sensitivity matrix. Elements of difference imaging sensitivity matrices were calculated by perturbing each image voxel's conductivity from a uniform reference value. So, for example, 447 of the 448 image voxels would have the conductivity 1.0 S/m, while the remaining voxel would have its value perturbed by 1% to 1.01 S/m. Figure 4.11a shows a cross section through the z-invariant conductivity distribution, where the z-axis is out of the paper.

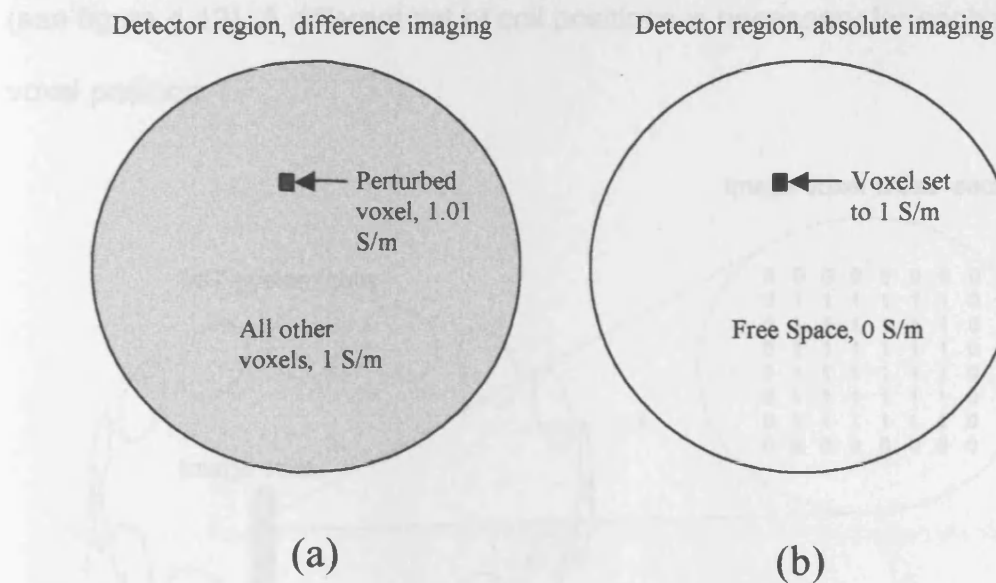


Figure 4.11. Contrast in model configuration for calculating difference (a) and absolute (b) sensitivity matrices.

A free-space sensitivity matrix has a background conductivity of 0 S/m, so the concept of perturbing conductivity values from a background reference value cannot apply here. During the calculation of the free-space sensitivity matrix elements, all image voxels will have a conductivity value of 0 S/m, except one, which will have a typical conductivity value (e.g. 1 S/m) assigned to it (figure

4.11b). This necessity for a solitary conductive voxel, coupled with the method used to calculate the induced eddy currents, excludes using 1 model voxel to represent 1 image voxel. This is because a minimum of 4 model voxels, arranged in a square, are needed to support an eddy current loop.

The solution to this problem is to use the entire grid to model 1 image voxel. This can be achieved by modifying the number of voxels, the grid spacing and the coil positions relative to the grid. The grid is effectively 'shrunk down' to the size of an image voxel. As the centre of the co-ordinate system is always defined to be at the centre of the grid, the coil positions must be altered such that the grid is at the image voxel position relative to the coils (see figure 4.12). A different set of coil positions is necessary for each image voxel position.

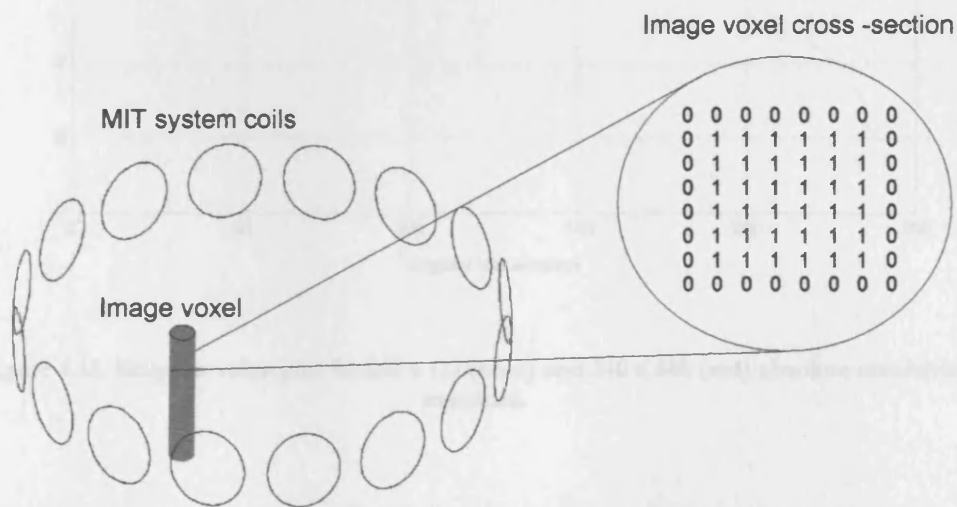


Figure 4.12. Shrinking the grid down to the size of 1 image voxel. A cross-section through one image voxel is shown in the close up.

4.2.2.2. Underdetermined free-space sensitivity matrices

Two sensitivity matrices have been calculated, using the method described above, for the Cardiff MIT system. They are 240×112 , and 240×448 matrices, and a singular value plot of the two is shown in figure 4.13.

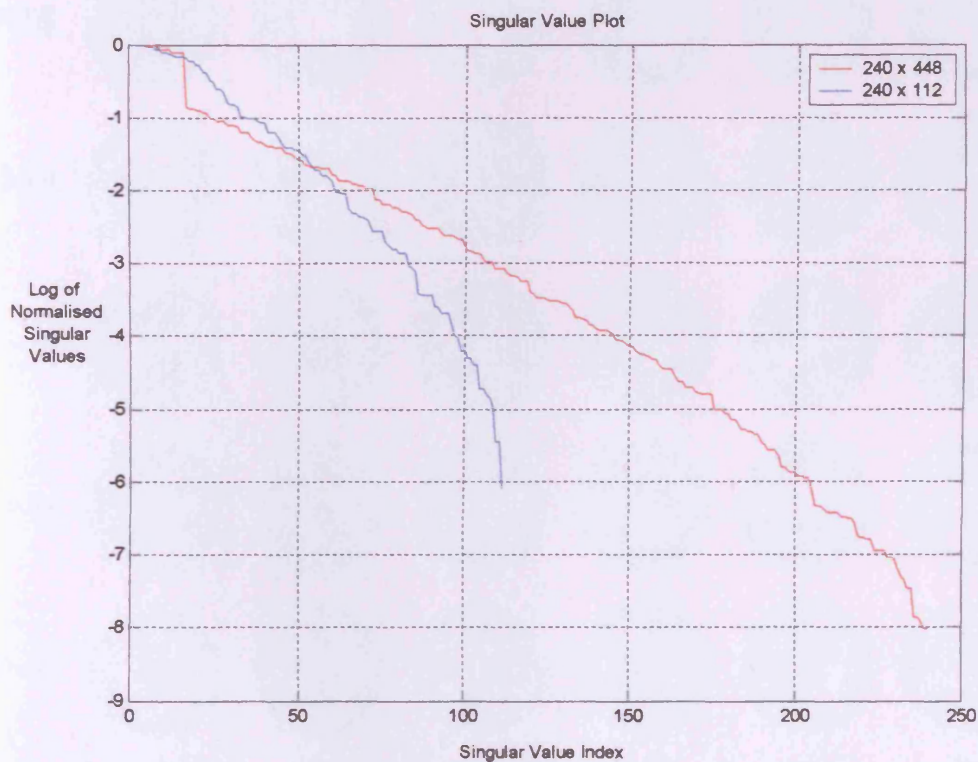


Figure 4.13. Singular value plot for 240×112 (blue) and 240×448 (red) absolute sensitivity matrices.

As was observed in section 4.2.1.2, the increase in the number of image voxels is accompanied by an improvement in the condition of the matrix, although here the 240×112 matrix is better conditioned than the underdetermined matrix for singular values between 10 and 50. Figures 4.14 and 4.15 show the basis image vectors for the 240×112 sensitivity matrix, while figures 4.16-4.19 show the basis images for the 240×448 sensitivity

matrix. The two sets show similarities in the introduction of more centralised information with higher basis indices. However, the 240 x 448 basis images of high index contain finer detail than the 240 x 112 high index images, as would be expected.

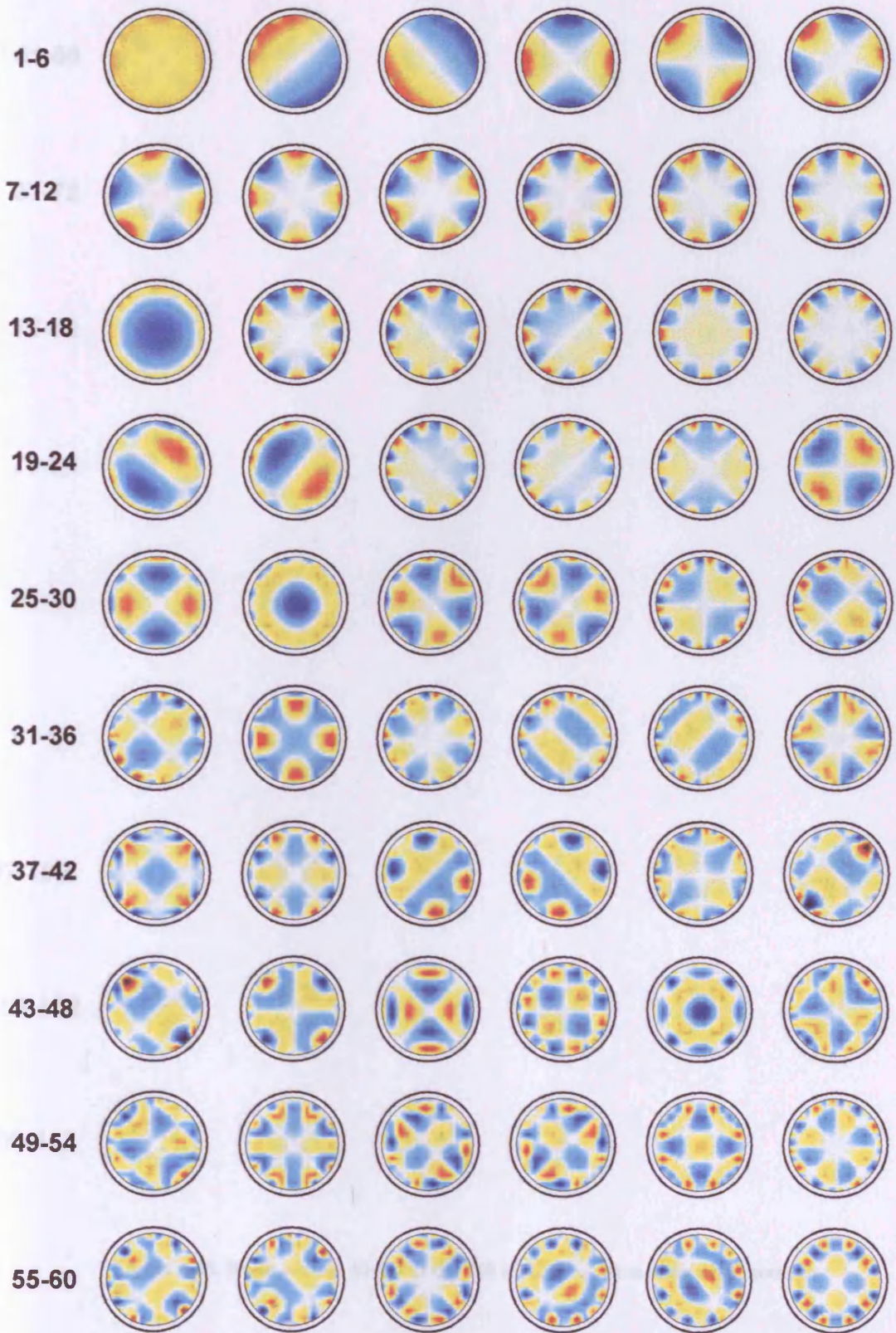


Figure 4.14. Basis vectors 1-60 of the 240 x 112 free-space sensitivity matrix.

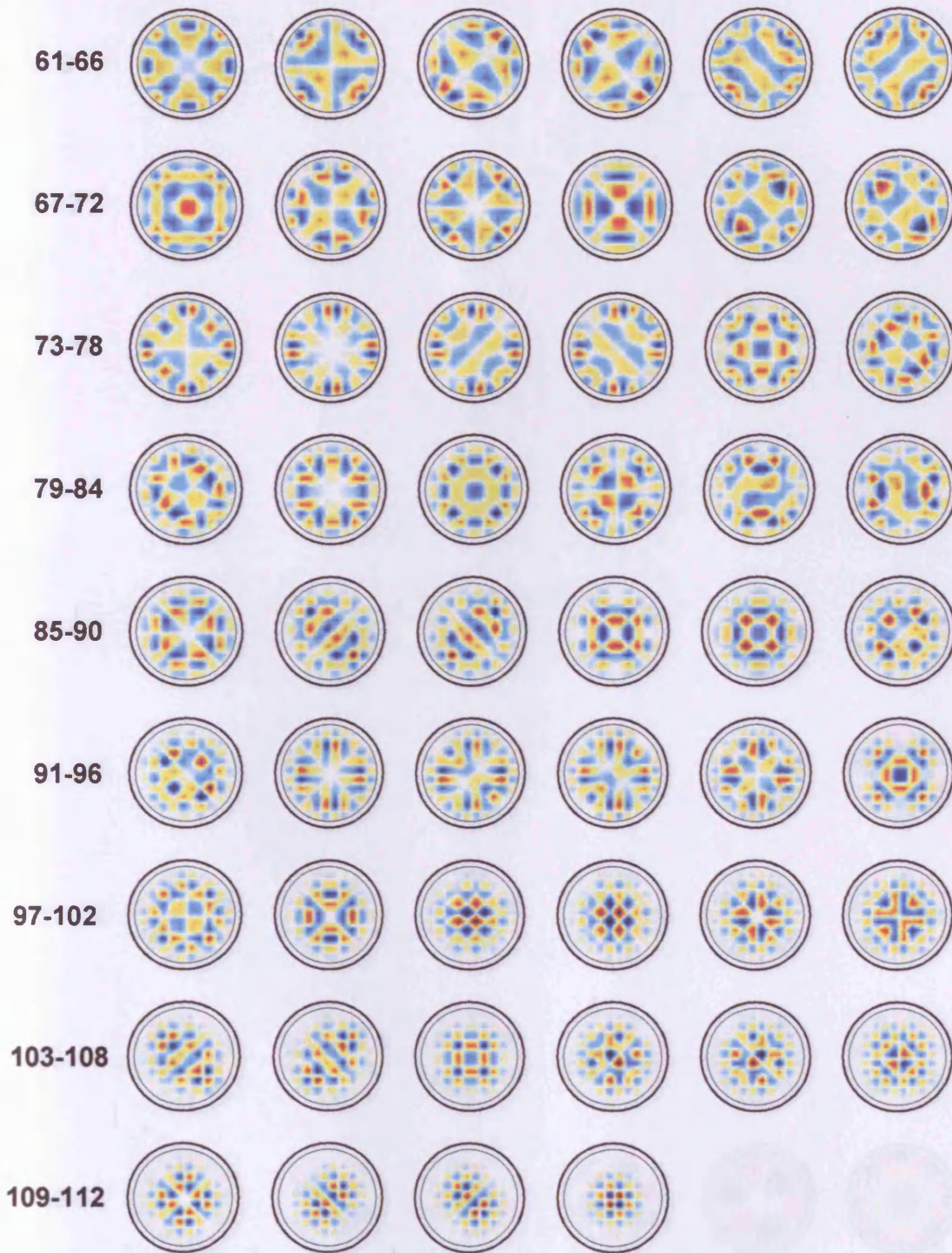


Figure 4.15. Basis vectors 61-112 of the 240 x 112 free-space sensitivity matrix..

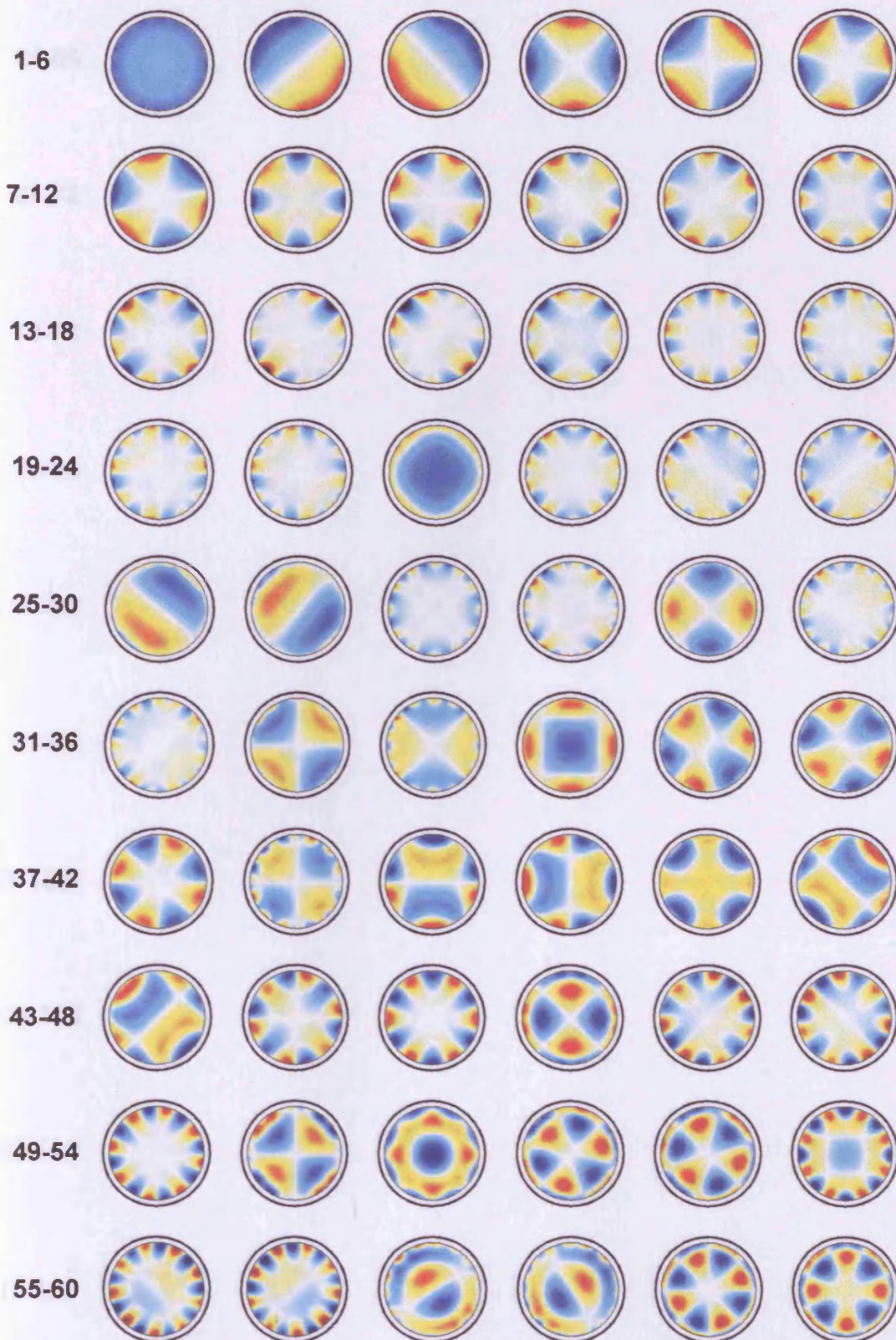


Figure 4.16. Basis vectors 1-60 of the 240 x 448 free-space sensitivity matrix..

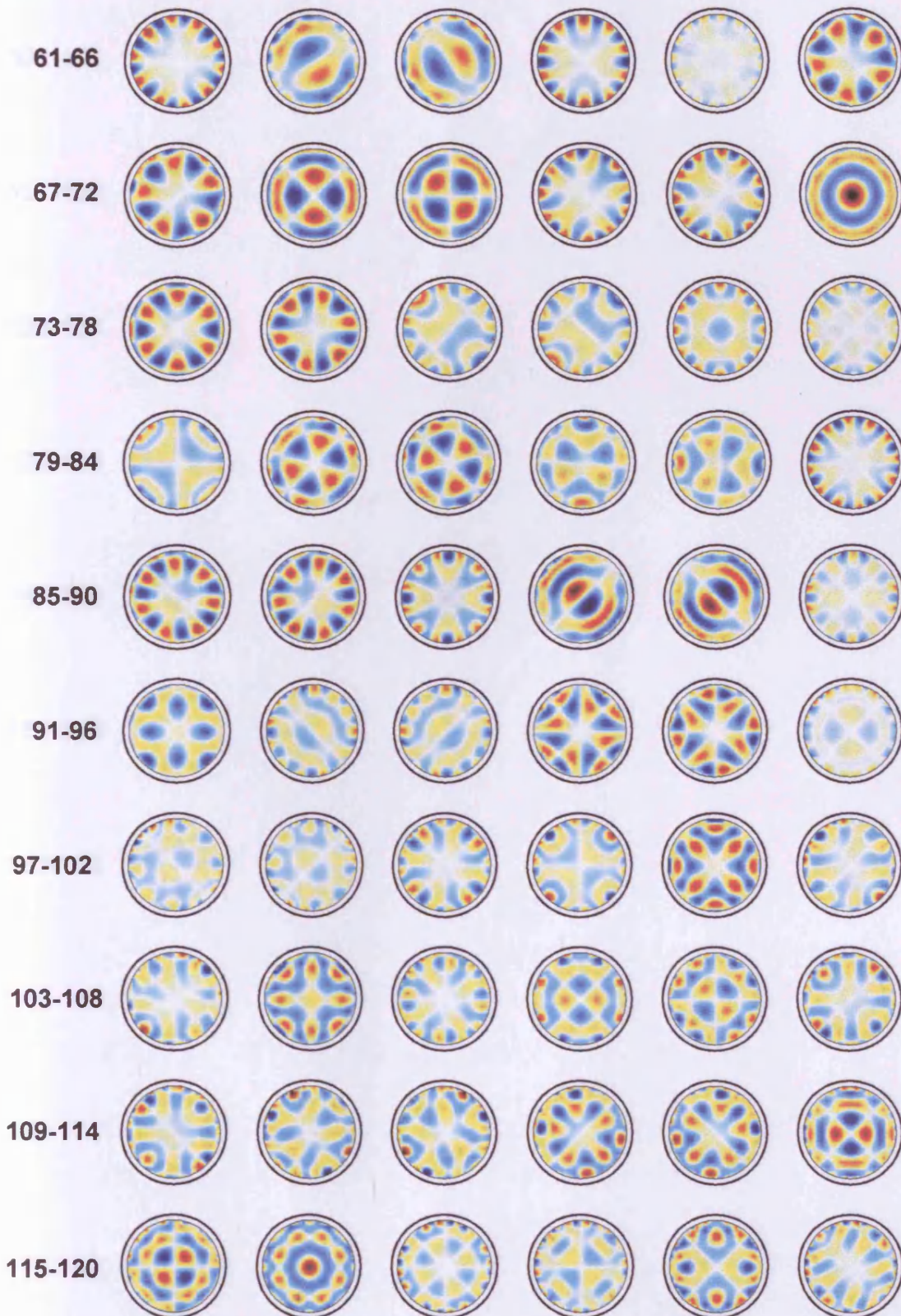


Figure 4.17. Basis vectors 61-120 of the 240 x 448 free-space sensitivity matrix..

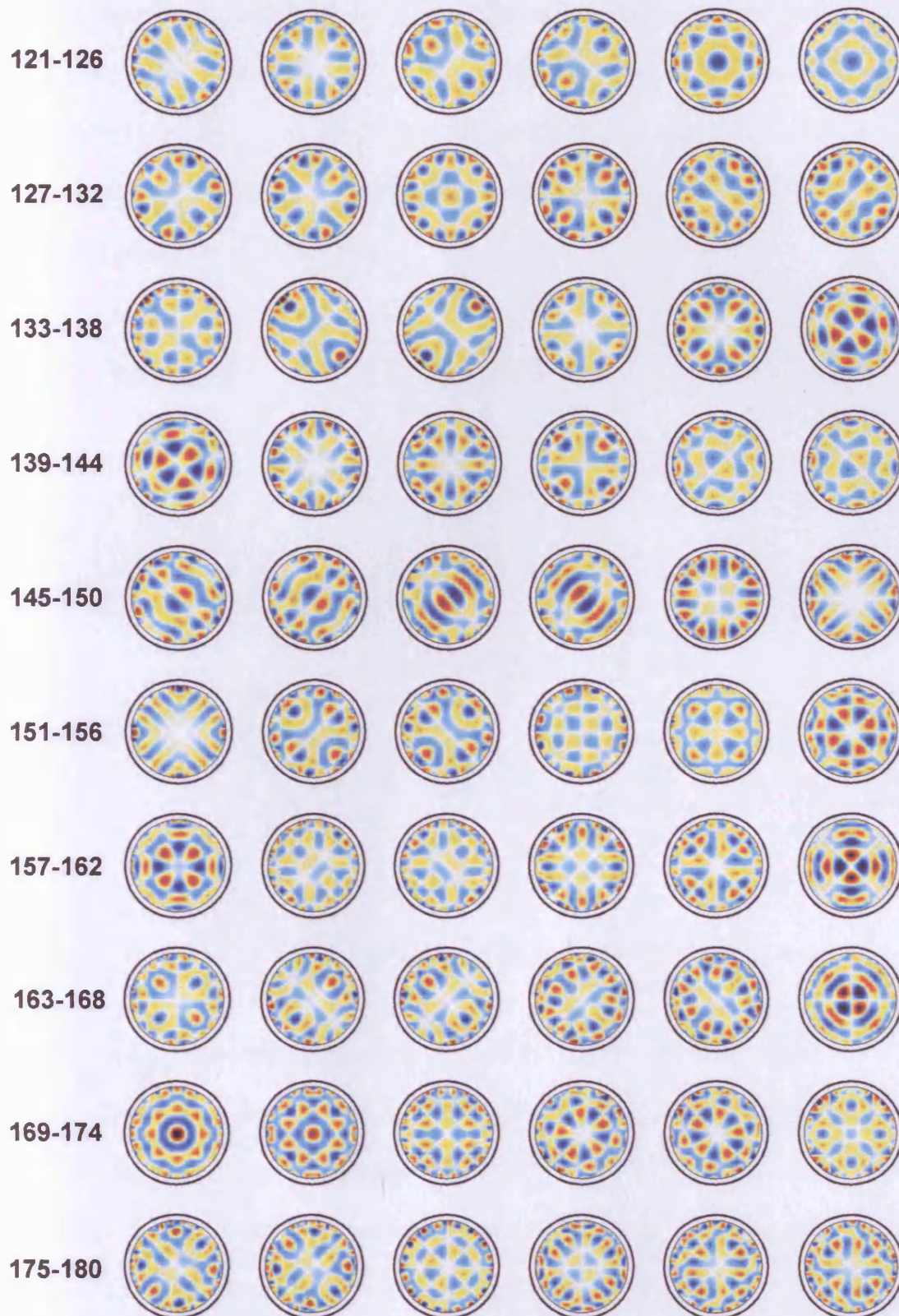


Figure 4.18. Basis vectors 121-180 of the 240 x 448 free-space sensitivity matrix..

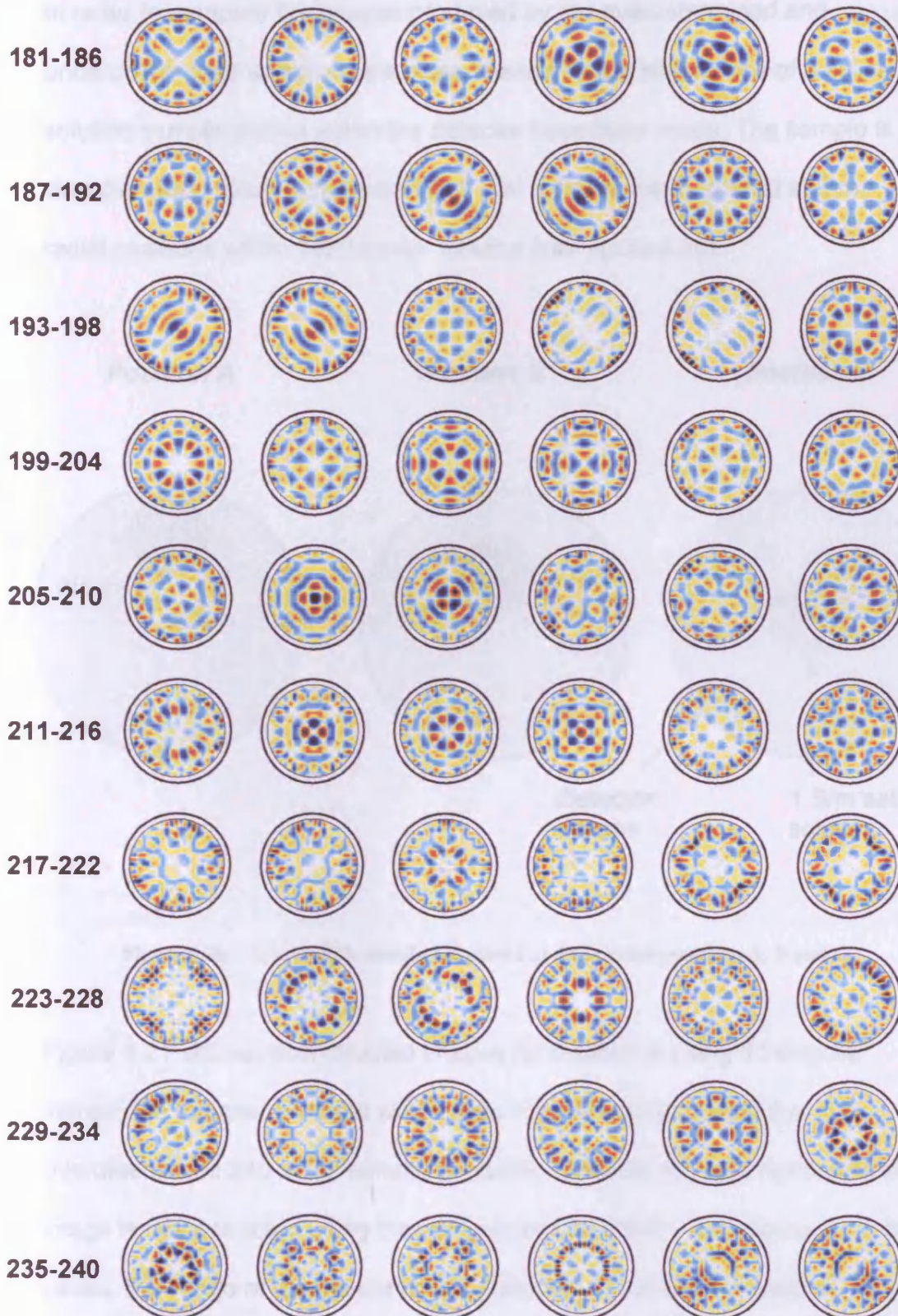


Figure 4.19. Basis vectors 121-240 of the 240 x 448 free-space sensitivity matrix..

In order to compare the images produced by the overdetermined and underdetermined sensitivity matrices, measurement simulations of a saline solution sample placed within the detector have been made. The sample is an 8cm diameter, 12cm high beaker of 1 S/m saline solution, placed at three radial positions within the detector volume (see figure 4.20).

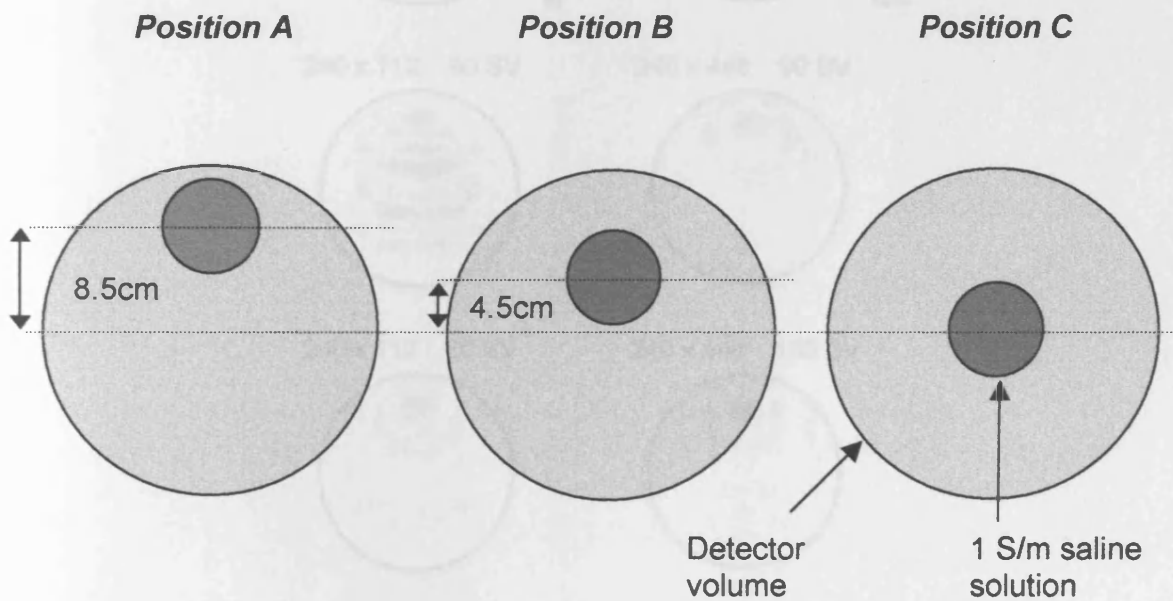


Figure 4.20. 1 S/m sample simulation placed at three radial positions A, B and C.

Figure 4.21 shows reconstructed images for position A using 60 singular values; the top row, left hand side image is reconstructed using the overdetermined 240×112 sensitivity matrix, while the top row, right hand side image is reconstructed using the underdetermined 240×448 matrix. In both cases, the image of the beaker is reconstructed in the correct position. As with the difference images of section 4.2.1.2, the 240×448 matrix produces a smoother reconstruction of the beaker. As the number of singular values used is increased to 90 (second row, figure 4.21), the 240×112 matrix image (left)

becomes distorted. Truncation to the largest 90 singular values clearly does not provide a sufficient level of regularisation in this case.

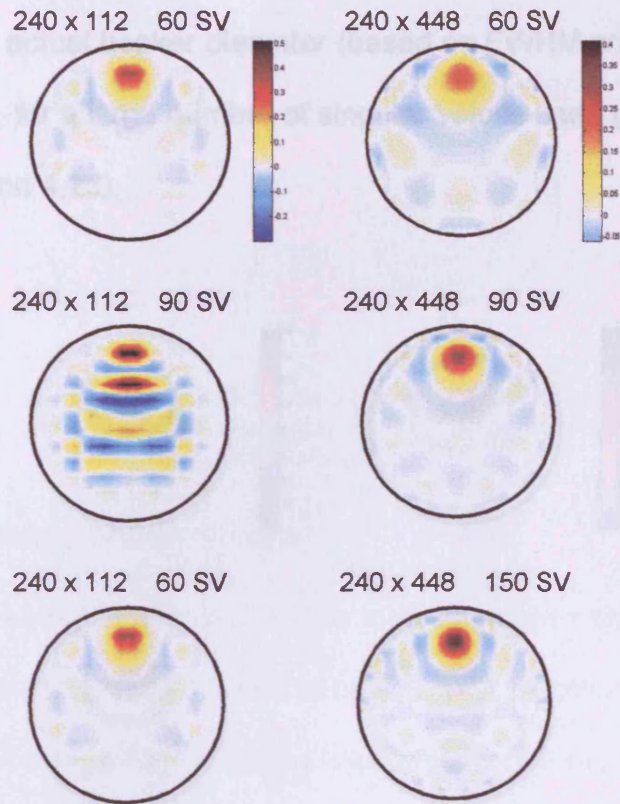


Figure 4.21. Reconstructed images of the 1 S/m saline sample simulation at position A. The 240 x 112 sensitivity matrix (left) and 240 x 448 sensitivity matrix (right) were truncated using different numbers of singular values (noted above each image).

While the largest 90 represent the majority of the singular values for the overdetermined case, this is not so for the underdetermined matrix, where there are a total of 240 singular values. Thus, a larger number of singular values and vectors can be used in the reconstruction (second row, right). By inspection, 60 and 150 are the optimum number of singular values for the overdetermined and underdetermined cases respectively (bottom row).

As the beaker is positioned closer to the centre of the detector volume (positions B and C), the number of singular values required to produce the

optimum image increases (figures 4.22 and 4.23). Again, the 240 x 448 matrix produces images with a more spherical reconstruction of the sample. Also noticeable is the fact that the 240 x 488 matrix reconstructs the sample image smaller than the actual beaker diameter (based on FWHM criterion; compare with figure 4.20), for a large number of singular values used (right, second row in figures 4.22 and 4.23).

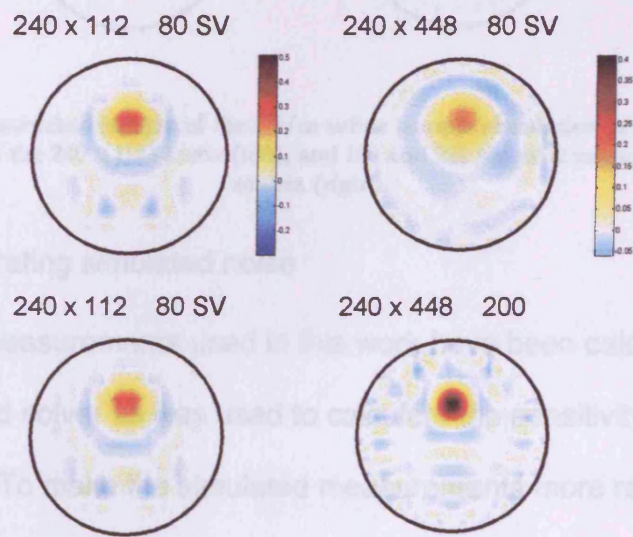


Figure 4.22. Reconstructed images of the 1 S/m saline sample simulation at position B, for 80 singular values of the 240 x 112 matrix (left), and 80 and 200 singular values of the 240 x 448 matrix (right).

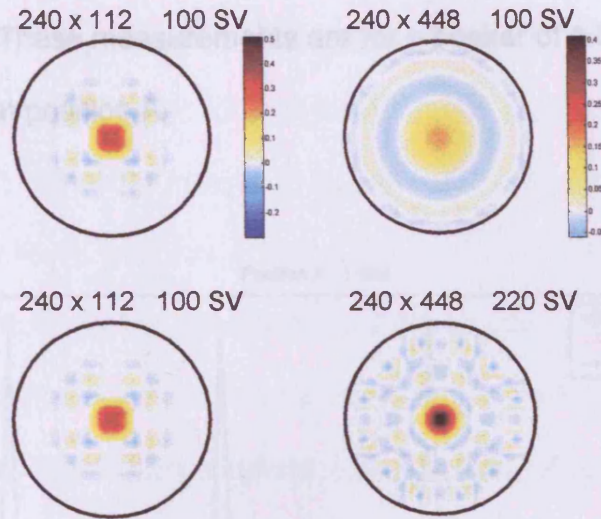


Figure 4.23. Reconstructed images of the 1 S/m saline sample simulation at position C, for 100 singular values of the 240 x 112 matrix (left), and 100 and 220 singular values of the 240 x 448 matrix (right).

4.2.2.3. Incorporating simulated noise

The simulated measurements used in this work have been calculated using the same forward solver as was used to calculate the sensitivity matrix (an 'inverse crime'). To make the simulated measurements more realistic, simulated random noise can be added. This allows the degree of image degradation due to noise to be evaluated, and gives a more realistic expectation of what imaging performance a real system could achieve. The method used to simulate random noise is described in appendix C. A standard deviation of 0.03 degrees has been assumed, as this is the value reported for the Cardiff MIT System (Watson *et al* 2002). The noise was added to the simulated measurements imaged in the previous section, reconstructed using the 240 x 448 matrix. Figure 4.24 displays the a plot of the first 60 of 240 simulated phase changes $\left(\frac{\Delta V}{V}\right)$ for the noise-free phase changes (blue line), noisy phase changes (red line), and the simulated noise

itself (black line). These measurements are for a beaker of 1 S/m saline solution situated at position A.

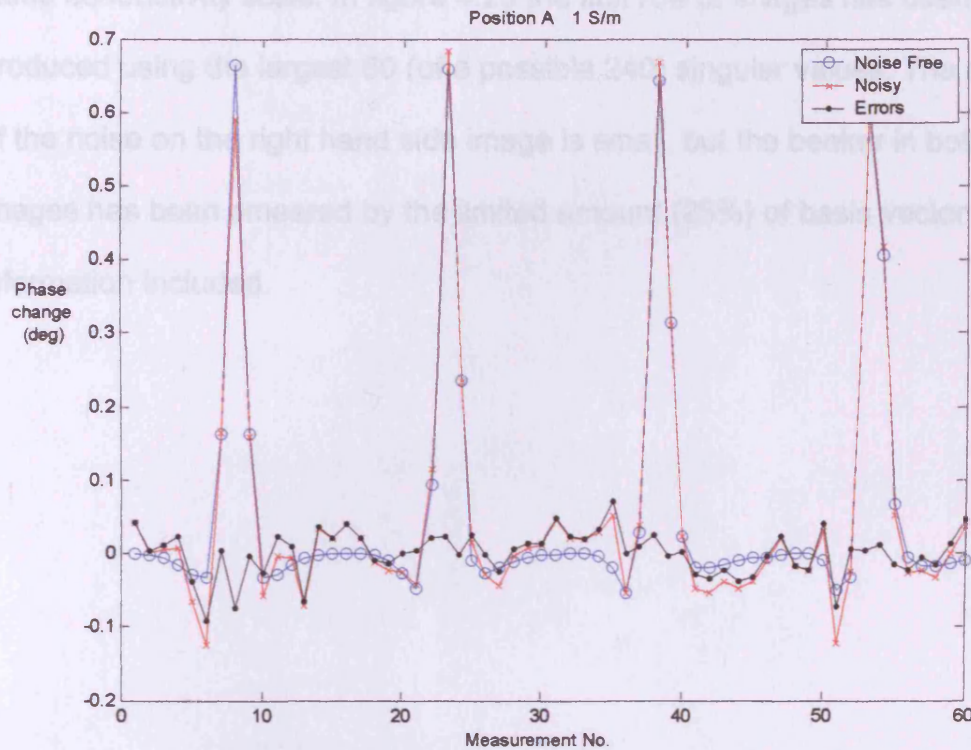


Figure 4.24. Plot of the first 60 simulated measurements for the 1 S/m beaker at position A; noise-free (blue), noisy (red) and the simulated noise itself (black).

The introduction of simulated noise significantly alters the values of the smaller measurements, but has limited impact on the large measurement peaks.

The images reconstructed from these noise-free (left side) and noisy (right side) simulated phase changes are shown in figure 4.25. Note that the same conductivity colour scale is used for the noise free images, but a different scale is used for each of the noisy images. This is to allow both the relatively small regularised conductivity values (at 60 singular values) and

larger noisy conductivity values (at 150 singular values) to be imaged clearly. This convention is also adopted for positions B and C (figures 4.27 and 4.29), such that all of the noise-free images in figures 4.25, 4.27 and 4.29 use the same conductivity scale. In figure 4.25 the first row of images has been produced using the largest 60 (of a possible 240) singular values. The effect of the noise on the right hand side image is small, but the beaker in both images has been smeared by the limited amount (25%) of basis vector information included.

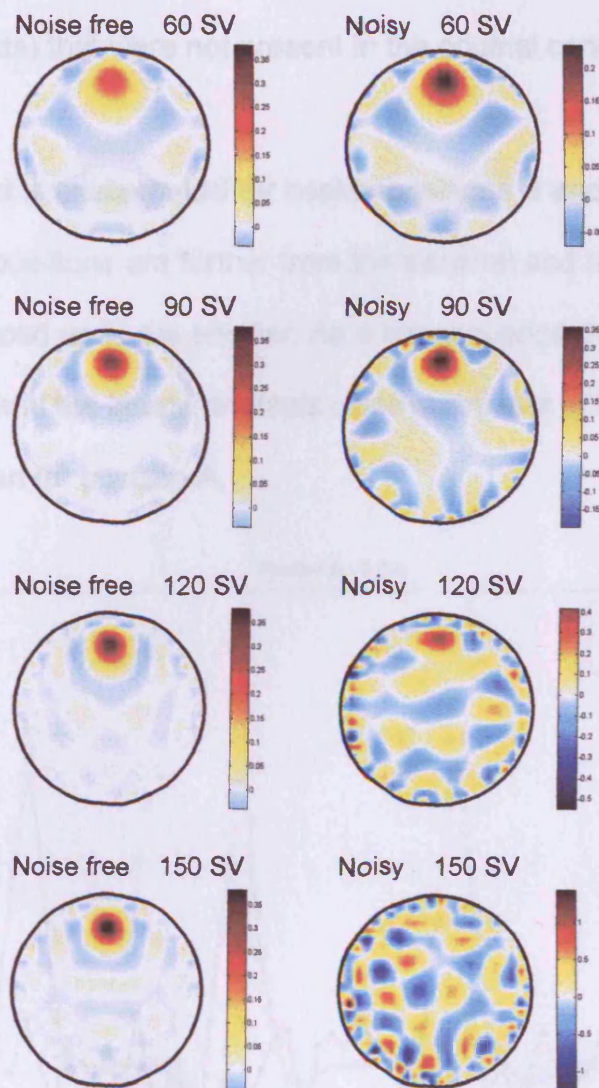


Figure 4.25. Reconstructed images for the noise-free (left) and noisy (right) simulations of a 1 S/m beaker at position A, using different levels of truncation.

Increasing the number of singular values (second to fourth rows of figure 4.25) sharpens the noise-free images, but degrades the noisy images. Using higher index singular values means that measurements more susceptible to noise are included, such as those between measurement numbers 10 and 20 in figure 4.24. These smaller phase changes have been drastically altered by

the noise, and bear little resemblance to their noise-free equivalents. When included in the image reconstruction process they produce undesirable features (artefacts) that were not present in the original conductivity distribution.

This effect is exacerbated for beaker positions B and C (figures 4.26 to 4.29); as these positions are further from the transmit and receive coils, the receive coil induced emfs are smaller. As a consequence the signal to noise ratio is smaller, and the image artefacts more prominent at lower singular value indices than for position A.

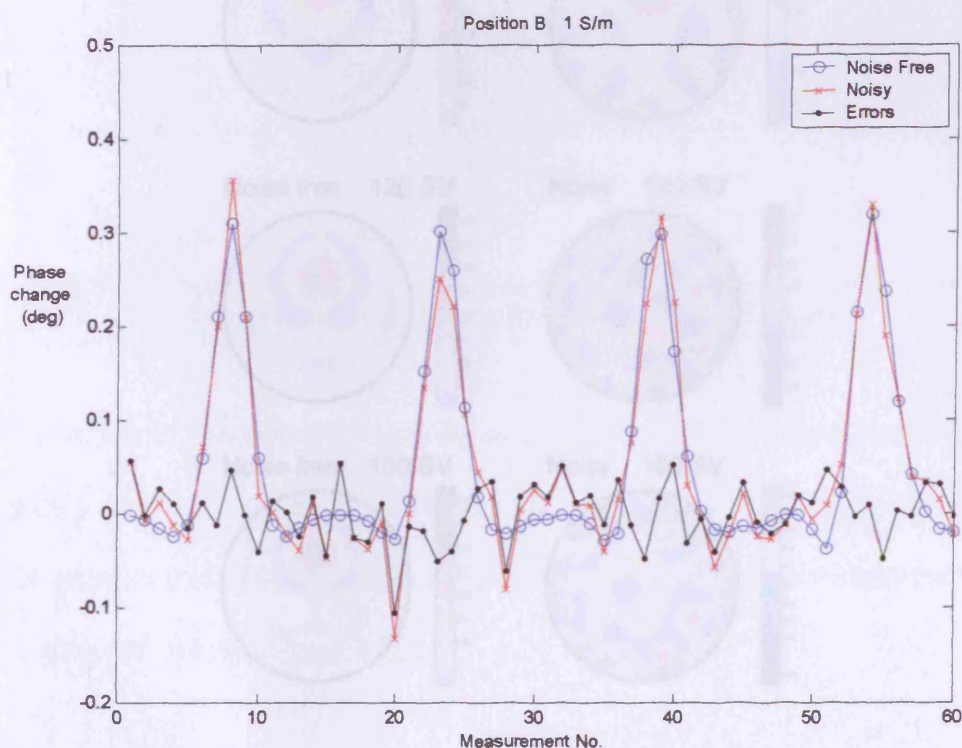


Figure 4.26. Plot of the first 60 simulated measurements for the 1 S/m beaker at position B; noise-free (blue), noisy (red) and the simulated noise itself (black).

The smaller magnitude of the phase change peaks for position B (figure 4.26) (compared to position A), mean that the random noise causes greater

distortion of the measurements that are most significant to the images. Consequently, the images display artefacts even with relatively few singular values included (figure 4.27).

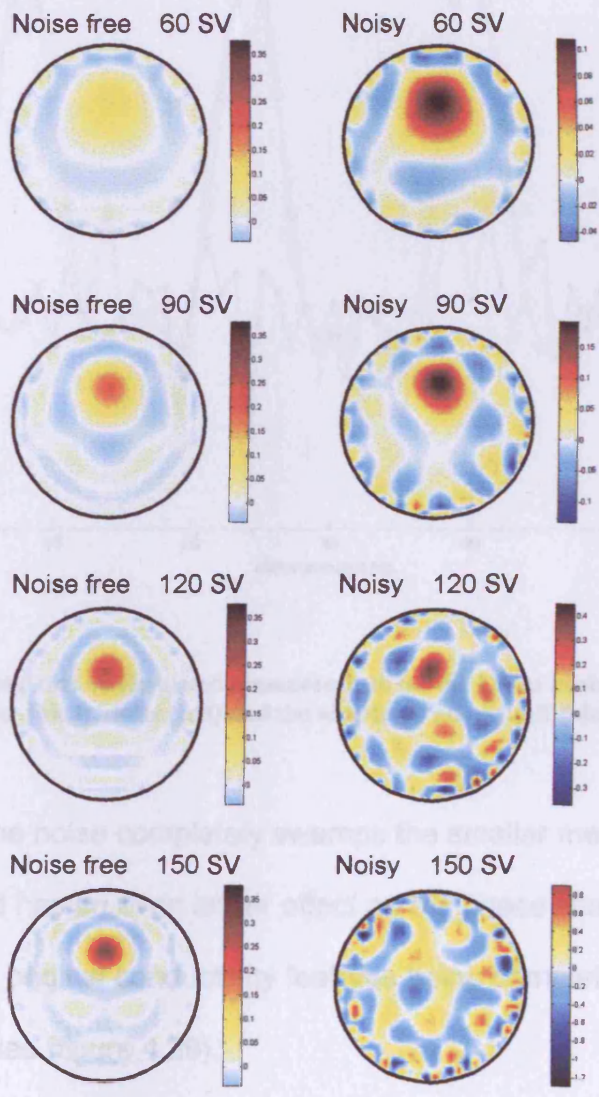


Figure 4.27. Reconstructed images for the noise-free (left) and noisy (right) simulations of a 1 S/m beaker at position B, both truncated to 150 singular values.

As the number of singular values is increased to 120, the original conductivity feature is still visible, but the number of erroneous features has increased dramatically.

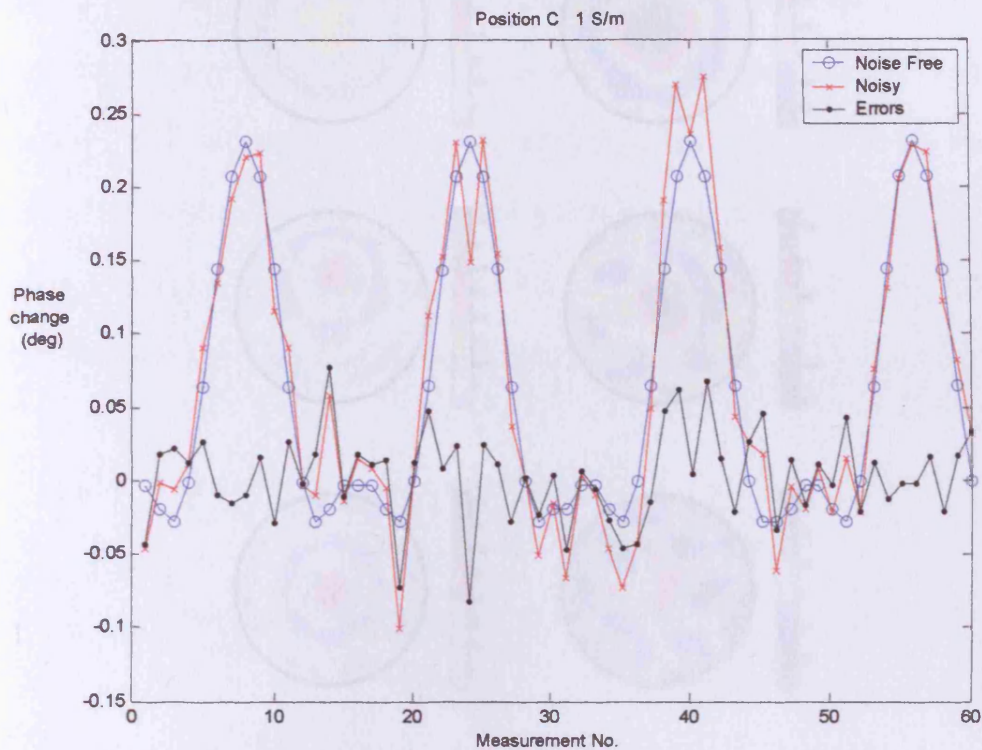


Figure 4.28. Plot of the first 60 simulated measurements for the 1 S/m beaker at position B; noise free (blue), noisy (red) and the simulated noise itself (black).

For position C, the noise completely swamps the smaller measurements (figure 4.28), and has an even larger effect on the phase change maxima.

This leads to the original conductivity features being completely obscured at 120 singular values (figure 4.29).

4.3. Planar array simulation

4.3.1. Introduction

A simulation of a planar MIT system, developed using a finite element solver, has been reported by Gencer and Tak (1998). At the time of writing, this is the only MIT study for biological tissues that has been published with sensitivity

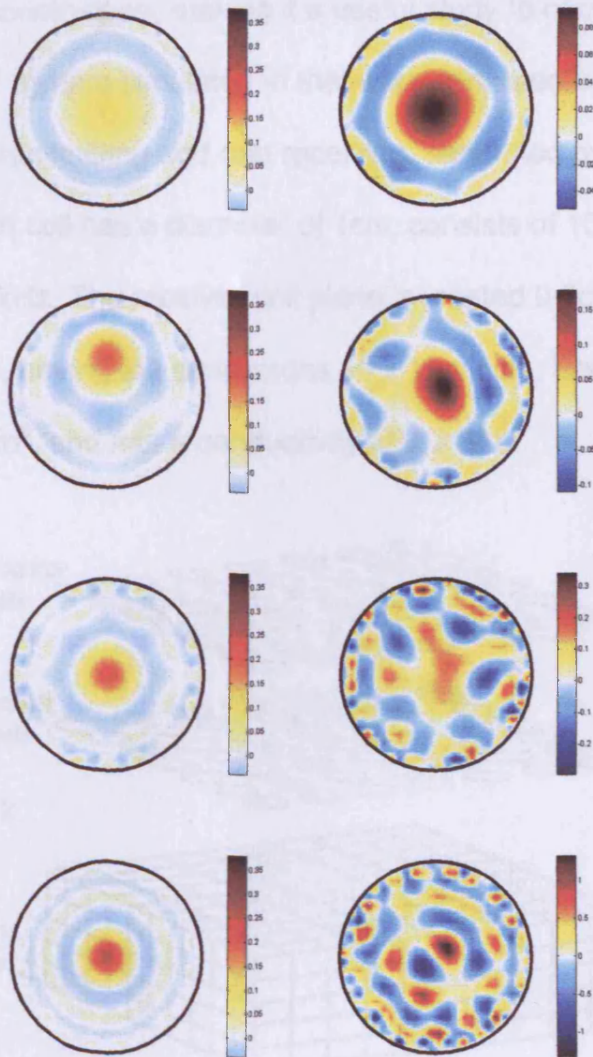


Figure 4.29. Reconstructed images for the noise free (left) and noisy (right) simulations of a 1 S/m beaker at position C, both truncated to 120 singular values.

4.3. Planar array simulation

4.3.1. Introduction

A simulation of a planar MIT system, developed using a finite element solver, has been reported by Gencer and Tek (1999). At the time of writing, this is the only MIT study for biological tissues that has been published with sensitivity

matrix based reconstruction, making it a useful study to compare our methods against. The MIT system simulated in that work consisted of two planar arrays of 49 coils, one transmitting and one receiving, separated by 0.5 cm (see figure 4.30). Each coil has a diameter of 1cm, consists of 1000 turns, and carries 1A at 50 kHz. The receiver coil plane is located 0.5cm above a conductive block, having the dimensions 10 x 10 x 5cm. Each voxel in the FEM mesh is 1cm³, and has a conductivity of 0.2 S/m.

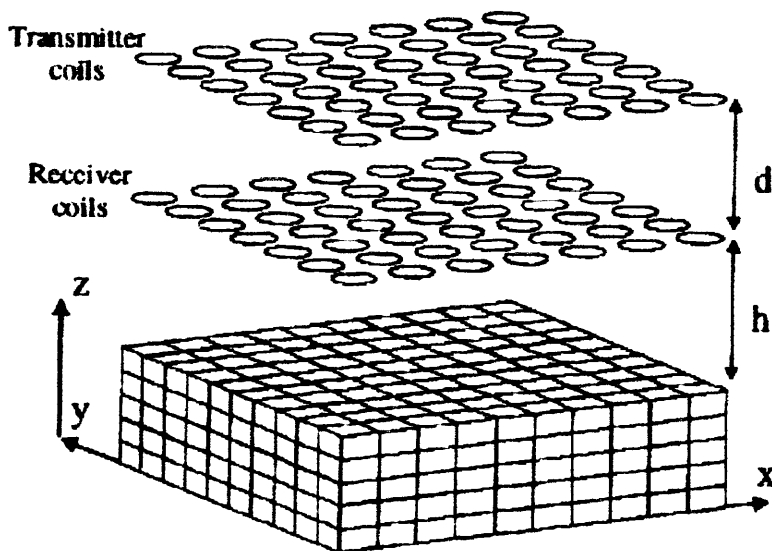


Figure 4.30. Planar coil arrays above conductive block, after Gencer and Tek 1999. The heights of the arrays above the block (d and h) are exaggerated to ease display.

The authors derived a first order relationship for the perturbation in the secondary magnetic field, in terms of the gradient of the electric scalar potential and its derivative with respect to conductivity (within the conductive block). Sensitivity matrix elements are calculated, rather than explicitly calculating the magnetic field at the receiver coils for the perturbed and reference cases. The system configuration allows $49 \times 49 = 2401$ independent

measurements, and as there are 500 voxels in the conductive block; the sensitivity matrix has dimensions of 2401 x 500.

The authors introduce the concept of a resolution matrix, \mathbf{R} , which is used to evaluate the performance of the imaging system. The resolution matrix is the product of the \mathbf{Y} matrix produced by singular value decomposition (section 3.3.4) with its transpose

$$\mathbf{R} = \mathbf{Y}\mathbf{Y}^T \quad (4.3.1)$$

The resolution matrix is used in the equation

$$\Delta\sigma^* = \mathbf{R}\Delta\sigma \quad (4.3.2)$$

to produce reconstructed images without the need for simulating measurements, which can be time consuming. It is a mapping between the actual conductivity distribution ($\Delta\sigma$), and the reconstructed conductivity ($\Delta\sigma^*$), that describes the loss of information that occurs in the reconstruction process. When all basis images (columns of \mathbf{Y}) are used in a reconstruction, \mathbf{R} is the identity matrix, and the system is able to reconstruct the original conductivity exactly (in an 'ideal' noise-free situation). However, there is likely to be a need to restrict the number of basis images used, to counter the effects of measurement noise swamping the image reconstruction. This removal of basis information alters the imaging capabilities of the system, and consequently the values in \mathbf{R} .

Gencer and Tek propose the Newton-Raphson method for image reconstruction, but only include images of rows of the resolution matrix (reproduced in 4.3.3). It should be noted, however, that the resolution matrix does not take into account the effects of non-linearity, and thus if used to

produce reconstructions of significant conductivity perturbations (>50%) it is likely to produce misleading results.

4.3.2. Cardiff MIT model simulation

The planar MIT system described above has been simulated using the Cardiff MIT model. There are two key differences between the Cardiff MIT model and the method of Gencer and Tek. Firstly, a finite-difference method is used for the Cardiff model, while a finite-element method is used by Gencer and Tek. Secondly, the Cardiff model explicitly calculates the change in receiver coil induced emf, while Gencer and Tek calculate changes in magnetic field via scalar potential gradients. These differences are significant, and agreement between simulation results will promote confidence in the validity of the Cardiff MIT model.

The results of the Cardiff MIT model planar array simulation are compared to those described by Gencer and Tek (reproduced to aid comparison) in section 4.3.3.

4.3.3. Simulation results comparison

4.3.3.1. Singular value plots

A plot of the log-normalised singular values, reproduced from Gencer and Tek (1999), is shown in figure 4.31(a). The corresponding plot calculated by the Cardiff MIT model is shown in figure 4.31(b). The two figures show good agreement, although the curve in 4.31(a) decays more rapidly at higher singular values. The condition number of the sensitivity matrices for Gencer

and Tek's study and the Cardiff study are 7.41×10^6 and 1.56×10^7 respectively.

The sensitivity pattern for a particular transmit-receive coil pair (one row of the sensitivity matrix) is reproduced in figure 4.32(a), and again the shape of the two curves agrees well, although the magnitude of the sensitivity matrix elements for Gencer and Tek's study ($\sim 10^{-17}$) is vastly smaller than for the Cardiff simulation ($\sim 10^{-7}$).

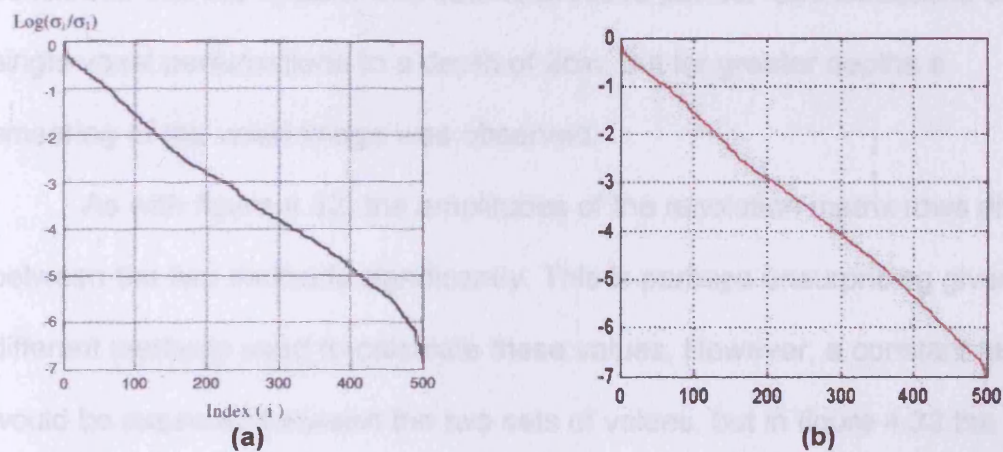


Figure 4.31. Plot of log normalised singular values; left (a) after Gencer and Tek 1999, right (b) calculated using Cardiff MIT model.

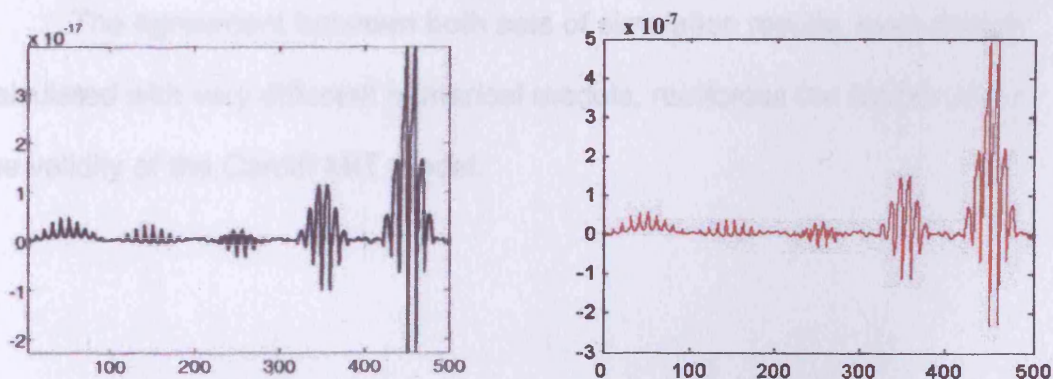


Figure 4.32. Sensitivity pattern for a particular transmit-receive coil pair (one row of the sensitivity matrix); left after Gencer and Tek 1999, right (b) calculated using Cardiff MIT model.

The authors plotted rows of the resolution matrix \mathbf{R} , which are effectively reconstructions of conductivity for individual voxel perturbations. These are reproduced here in figure 4.33 (left side), and compared with the corresponding Cardiff model values. Indices 1-100 correspond to the bottom layer of the block (on figure 4.30), 2-200 the second-to-bottom layer, etc. The first 300 basis vectors were used in the reconstruction, which the authors equated to a measurement signal-to-noise ratio (SNR) of 80dB. It was concluded that the system was able to produce perfect reconstructions of single voxel perturbations to a depth of 2cm, but for greater depths a smearing of the voxel image was observed.

As with figure 4.32, the amplitudes of the resolution matrix rows differ between the two methods significantly. This is perhaps unsurprising given the different methods used to calculate these values. However, a constant factor would be expected between the two sets of values, but in figure 4.32 the difference is $\sim 10^{10}$, while in figure 4.33 it is $\sim 10^{-5}$. The cause of this discrepancy is unknown.

The agreement between both sets of simulation results, even though calculated with very different numerical models, reinforces the confidence in the validity of the Cardiff MIT model.

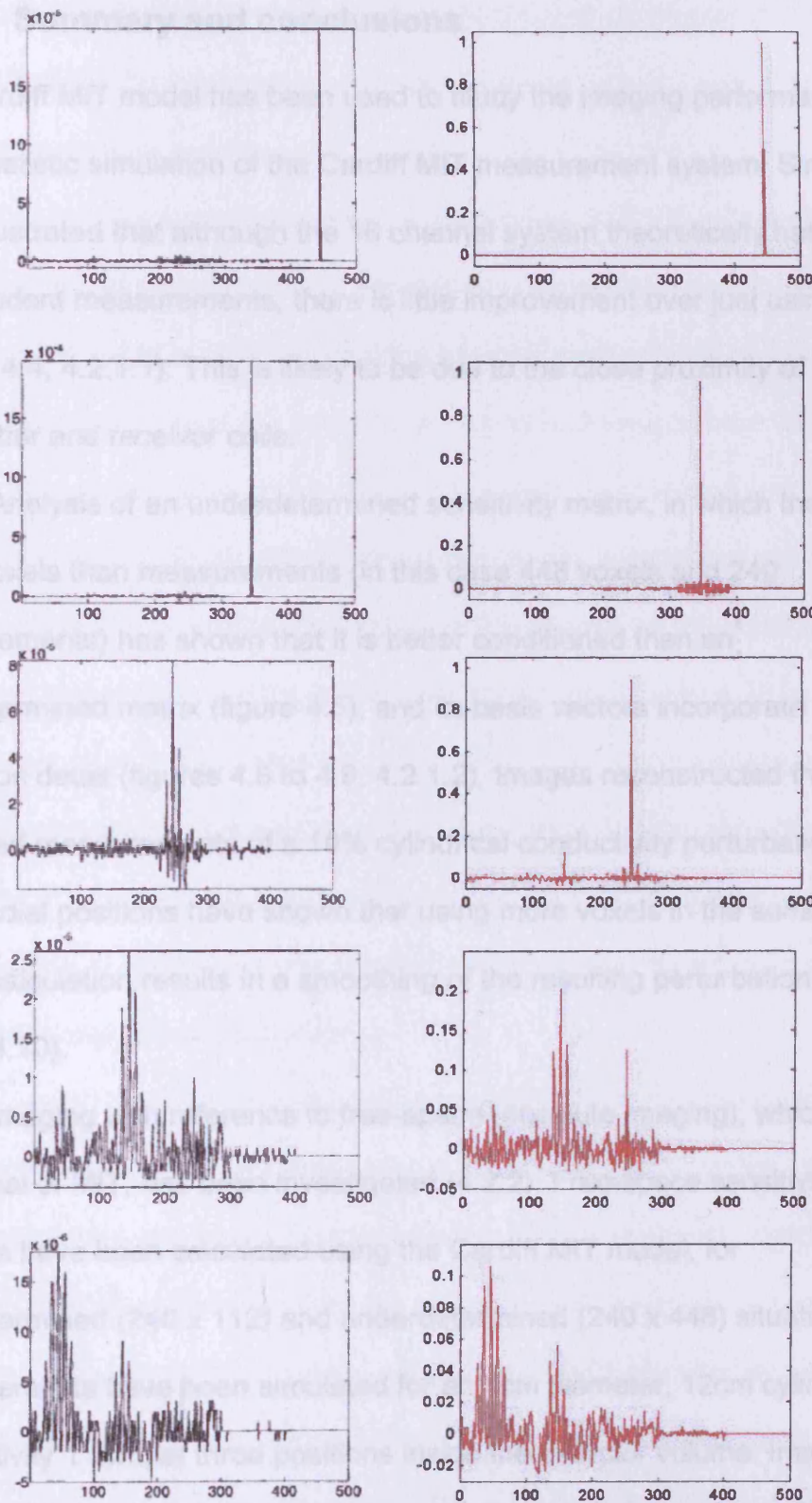


Figure 4.33. Row of resolution matrix for voxel 'depths' of (top row to bottom row); left (a) after Gencer and Tek 1999b, right (b) calculated using Cardiff MIT model.

4.4. Summary and conclusions

The Cardiff MIT model has been used to study the imaging performance of a more realistic simulation of the Cardiff MIT measurement system. Simulations have illustrated that although the 16 channel system theoretically has 240 independent measurements, there is little improvement over just using 120 (Figure 4.4, 4.2.1.1). This is likely to be due to the close proximity of the transmitter and receiver coils.

Analysis of an underdetermined sensitivity matrix, in which there are more voxels than measurements (in this case 448 voxels and 240 measurements) has shown that it is better conditioned than an overdetermined matrix (figure 4.5), and its basis vectors incorporate finer resolution detail (figures 4.6 to 4.9, 4.2.1.2). Images reconstructed from simulated measurements of a 10% cylindrical conductivity perturbation at three radial positions have shown that using more voxels in the sensitivity matrix calculation results in a smoothing of the resulting perturbation images (figure 4.10).

Imaging with reference to free-space (absolute imaging), which is the main goal of MIT, has been investigated (4.2.2). Free-space sensitivity matrices have been calculated using the Cardiff MIT model, for overdetermined (240×112) and underdetermined (240×448) situations. Measurements have been simulated for an 8cm diameter, 12cm cylinder of conductivity 1 S/m, at three positions inside the detector volume. Images reconstructed from these simulated measurements using the 240×112 and 240×448 free-space sensitivity matrices again show that the underdetermined sensitivity matrix produces smoother images. These images

also show that the sample diameter is reconstructed as smaller than the actual diameter, for increasing numbers of singular values used. The reason for this feature is uncertain.

The introduction of simulated random noise (4.2.2.3), of a level representative of an experimental measurement system (standard deviation 0.03 degrees), significantly reduced the imaging performance of the system studied. However, it was still possible to reconstruct images from 'noisy' measurements that gave reasonable representations of the original conductivity distributions, but was necessary to use a smaller number of singular values. This led to a smearing of the images as the distribution was positioned closer to the centre of the detector region (figures 4.25 to 4.29). The incorporation of simulated random noise is vital in any realistic estimation of the imaging performance of an MIT system, as is illustrated by the difference in noise-free and noisy images. Inclusion of noise mitigates the inverse crime of using the same forward solver for sensitivity matrix and simulated measurement calculation.

A useful comparison has been made (4.3) between simulation results produced by the Cardiff MIT model and finite-element MIT system model results published previously. The two models differ significantly in their approach to solving the governing equations of MIT. A sensitivity matrix was calculated for a planar MIT system, consisting of 49 transmitter and 49 receiver coils. A resolution matrix R was calculated from the singular decomposition of the sensitivity matrix. Rows of R were compared with those calculated by the finite-element model. Despite the differences in the two models, the results agreed closely, providing further evidence (along with

analytical and experimental comparisons in 2.3 and 2.4) that the Cardiff MIT model provides reasonable MIT simulations.

The work presented in this chapter facilitates the selection of appropriate sensitivity matrices to be used to reconstruct images from practical MIT measurements. In the following chapter, images will be reconstructed from practical MIT measurements using the 240×448 difference sensitivity matrix (4.2.1.2) truncated to 60 singular values, and the 240×448 free-space sensitivity matrix truncated to 70 singular values. These truncation levels were chosen after consideration of the effects of including simulated noise in 4.2.2.3.

4.5. References

Gencer NG, Tek MN, 1999, Electrical conductivity imaging via contactless measurements. *IEEE Trans. Medical Imaging*, vol. 18, no. 7, p. 617-627

Meeson S, Killingback ALT, Blott BH, 1995, The dependence of EIT images on the assumed initial conductivity distribution: a study of pelvic imaging.

Phys. Med. Biol., vol. 40, p. 643-657

Watson S, Williams RJ, Gough W, Morris A, Griffiths H, 2001, The Cardiff magnetic induction tomography system. *Proc. Int. Med. Fed. Biol. Eng.*

EMBEC02, Vienna, Austria, Dec. 4-8, ISBN 3-901351-62-0, vol. 3 (1), p. 116-

117

5. Imaging experimental measurements

5.1. Introduction

In this chapter, the image reconstruction method described in chapters 3 and 4 will be used to reconstruct images from experimental measurements made with the Cardiff MIT system (Watson *et al* 2002). This system (figure 5.1) consists of 16 transmitter and 16 receiver coils arranged in an equiangular circular configuration. Each transmitter-receiver pair is mounted on the same plastic former, attached to an electromagnetic confinement screen (aluminium) of diameter 35cm. Each coil consists of 2 turns and has a diameter of 5cm. The transmitter and receiver circuits for each coil are located on the exterior of the confinement screen.

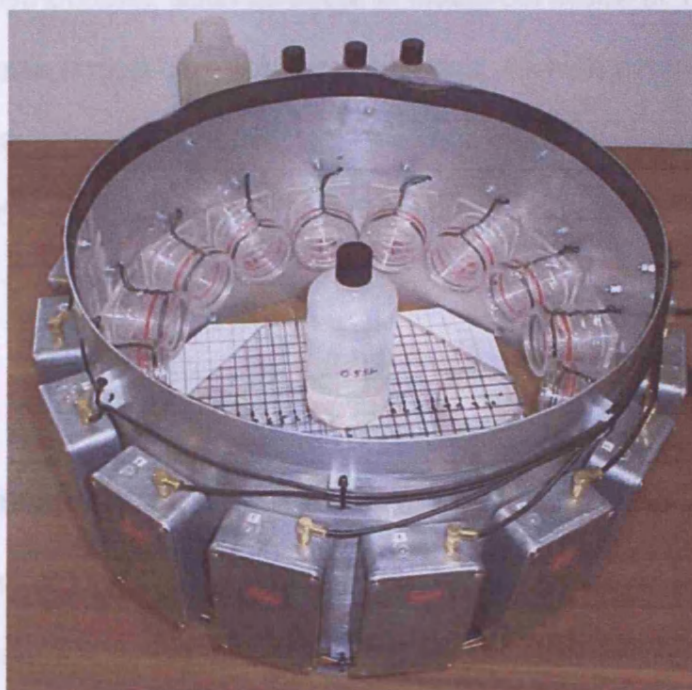


Figure 5.1. The Cardiff MIT system front end (photograph taken by S. Watson).

The operating frequency of 10 MHz is downconverted to 10 kHz by appropriate mixer circuitry, before demultiplexing and demodulation, in order to provide high phase stability. The real and imaginary parts of the receiver signal are measured using a digital lock-in amplifier employing phase sensitive detection. Measurement protocol involves first taking a reference data frame, followed by a frame with the sample in place. A complete measurement frame consists of $16 \times (16-1) = 240$ measurements, rather than $16 \times 16 = 256$ measurements, as 'same-former' measurements are not performed due to the large primary signals involved. Gathering one frame of data takes approximately 135 seconds. Images of the conductivity distribution σ within the coil array are reconstructed using equation 9 from chapter 3.

Although medical MIT attempts to image relatively low contrast conductivity distributions, such as occur in biological tissue at 10 MHz, it is instructive to also image high contrast situations. As high contrast conductivity MIT images have been previously reported (e.g. Korjenevsky *et al* 2000), attempting similar scenarios will allow comparison between different MIT systems.

5.2. High-contrast conductivity distributions

The task of imaging high-contrast conductivity distributions has been investigated using saline-filled plastic bottles placed within the detector volume, and Perspex rods immersed in a saline tank. The former provides a conducting region within an insulating background (air), while the latter provides an insulating region inside a conducting background. The 240 x 448

sensitivity matrix described in 4.2.2.2 is used in the reconstruction process. This matrix was calculated with reference to free-space; for each transmitter-receiver combination (matrix rows), one voxel was assigned a conductivity of 1 S/m while all others were set to 0 S/m, and this was repeated for all voxels (matrix columns). The matrix element is the $\frac{\Delta V}{V}$ value calculated in this situation. The largest 70 singular values have been used in all image reconstructions. The reconstructed conductivity values in each image have been normalised to the largest positive or negative value (noted in each legend) encountered in all images within the same figure.

5.2.1. Absolute imaging

Absolute imaging involves taking a reference set of measurements with the detector volume empty, followed by a set with the sample in place. Any negative values of conductivity have been removed from the reconstructions, by setting such values equal to zero. This is justified by the fact that absolute negative conductivity is physically meaningless, and therefore such features can be unequivocally considered to be reconstruction errors. This is in contrast to reconstructing difference images (5.2.2), in which negative changes in conductivity are displayed.

5.2.1.1. Image variation with position

The variation of image quality with radial position was investigated using a plastic bottle, of diameter 7.4cm and height 11.4cm, and containing saline solution of conductivity 0.9 S/m. This sample was positioned such that its centre was at (0, 1.2), (0, -3.7) and (0, -8.7) cm respectively (with the origin

defined to be at the centre of the detector region). Figure 5.2 shows the reconstructed images for each of the three sample positions. The x and y coordinate axes are shown in grey in 5.2(a), while the z axis is out of the plane of the paper.

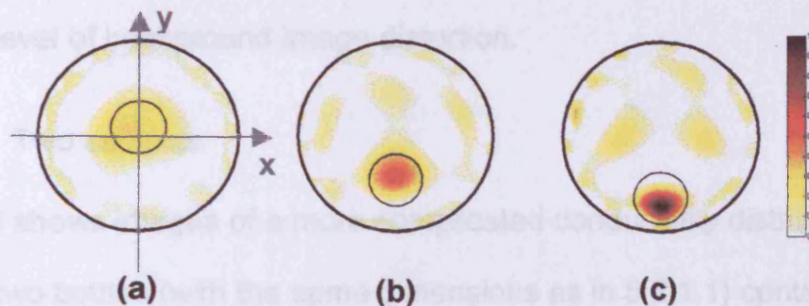


Figure 5.2. ABSOLUTE MEASUREMENTS, FREE-SPACE SENSITIVITY MATRIX. Images reconstructed from measurements made on a plastic bottle containing saline of conductivity 0.9 S/m. The sample is displaced from the centre along the y-axis by 1.2cm (a), -3.7cm (b) and -8.7cm (c). The actual position and size of the sample is shown by the small black circles, while the larger circles represent position of the receiver coils. All three images are normalised to the maximum reconstructed conductivity value of 26.2 S/m.

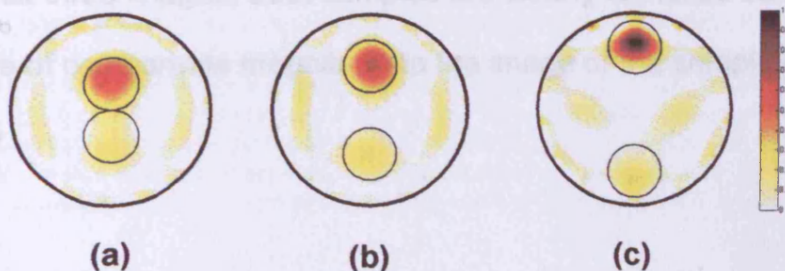


Figure 5.3. ABSOLUTE MEASUREMENTS, FREE-SPACE SENSITIVITY MATRIX. Images of two plastic bottles, containing saline of conductivity 0.9 S/m and 2.4 S/m. The samples are positioned along the y-axis with 0cm (a), 5cm (b) and 10cm (c) separation. The actual position and size of the sample is shown by the small black circles, while the larger circles represent position of the receiver coils. All three images are normalised to the maximum reconstructed conductivity value of 74.6 S/m.

This co-ordinate system is used for all of the images in this chapter. In each image, the smaller black circles mark the original sample size and position, while the larger circles mark the circumference on which the receiver coils lie.

In all three images, the sample is reconstructed at approximately the original position.

As the sample gets closer to the periphery (figures 5.2(a) to 5.2(c)), the image is spatially compressed. The magnitude of the reconstructed conductivity also increases as the sample is positioned closer to the coils, as does the level of background image distortion.

5.2.1.2. Two samples

Figure 5.3 shows images of a more complicated conductivity distribution, featuring two bottles (with the same dimensions as in 5.2.1.1) containing saline solution, one of conductivity 0.9 S/m and another of conductivity 2.4 S/m. The positioning corresponding to the images is as follows; the samples were positioned along the y-axis, equidistant from the centre with a separation of 0cm (a), 5cm (b) and 10cm (c). The 2.4 S/m sample was located in the +y region. For all three images, both samples are clearly identified but the image artefacts are of comparable magnitude to the image of the sample of lower conductivity.

5.2.2. Difference imaging

Another high-contrast conductivity distribution is that of an insulating region embedded within a conducting region. This scenario has been realised experimentally by immersing a Perspex rod (diameter 3.8cm and height 8cm) in a tank of saline solution. The tank had a diameter of 24cm and was filled with saline of conductivity 1 S/m, to a depth of 8cm. The measurement protocol here involved taking a 'reference' set of measurements with the

saline tank in place, followed by a 'perturbed' measurement set with the insulating rod inserted into the tank. The phase angles calculated from the reference set were subtracted from the perturbed phase angles. The insulating rod was placed at five positions on the positive y-axis; 0cm (a), 2cm (b), 4cm (c), 6cm (d) and 8cm from the centre of the detector.

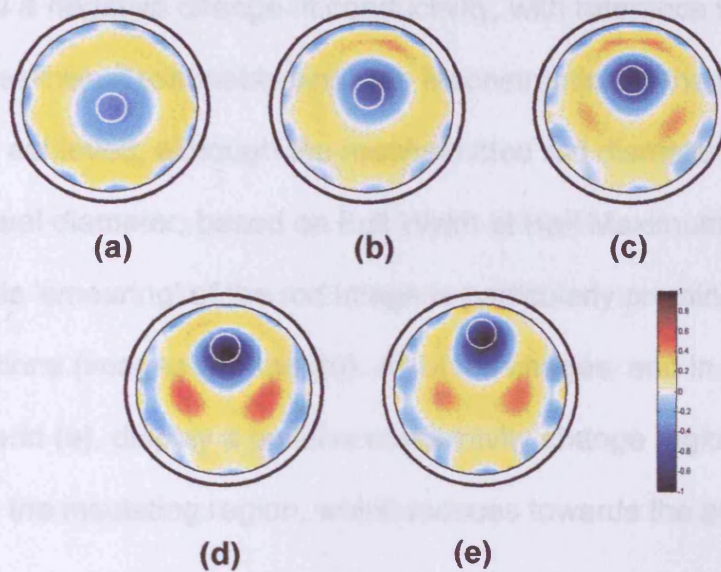


Figure 5.4. DIFFERENCE MEASUREMENTS, FREE-SPACE SENSITIVITY MATRIX.

Images reconstructed from measurements made on a saline filled tank (1 S/m) containing an insulating rod (< 0.01 S/m). The rod was positioned along the y-axis at displacements of 0cm (a), 2cm (b), 4cm (c), 6cm (d) and 8cm (e) from the centre. In each image, the actual position of the rod is denoted by the small white circle, the tank boundary is represented by the inner large black circle, while the thicker outer circle represents the position of the receiver coils. All five images are normalised to the greatest magnitude conductivity value, 13.6 S/m.

The images reconstructed from these measurements are shown in figure 5.4. The small white circle shows the position of the rod, the larger thin black circle denotes the tank boundary, while the thick outer circle represents the receiver coil positions. Although the measurements made were with reference to the saline tank, the free-space sensitivity matrix has been used to reconstruct images. This is because the 'difference' sensitivity matrix described in chapter

4 is unsuitable for use with high-contrast conductivity distributions, as it was calculated for 1% perturbations on a 1 S/m uniform background.

The images in figure 5.4 show the rods as regions of negative conductivity, coloured blue/black. This is due to the influence of the saline tank being removed by including it in reference measurements (the insulating rod provides a negative change in conductivity, with reference to the conducting saline). Reasonably accurate reconstruction of the positioning of the rod was achieved, although the reconstructed rod diameter was larger than the actual diameter, based on Full Width at Half Maximum (FWHM) criterion. This 'smearing' of the rod image is particularly prominent for more central positions (images (a) and (b)). All of the images, and in particular images (d) and (e), display a positive conductivity change region immediately surrounding the insulating region, which reduces towards the periphery.

5.2.3. Discussion

Reasonable imaging performance has been achieved for high-contrast conductivity distributions. Absolute imaging of individual samples (5.2.1.1) exhibited an compression of the image as the sample was positioned closer to the edge of the detector region (figure 5.2). The magnitude of the reconstructed conductivity also increased as the sample was positioned closer to the edge of the detector region.

The calculation of the sensitivity matrix incorporated the fact that received signal sizes increase as the sample gets closer to the coils. Therefore, if 'perfect' image reconstruction were possible, the magnitude of the reconstructed conductivity would be independent of position. However, the

truncation of the sensitivity matrix removes basis information from the centre of the image, and so it is plausible that central perturbations are in fact reconstructed with smaller magnitudes.

Images of absolute measurements made on two saline samples, of different conductivity (0.9 S/m and 2.4 S/m), have shown that it is possible to distinguish between the two located 5cm apart (figure 5.3(b)). However, the magnitude of the conductivity of the weaker of the two saline samples is comparable with image artefact levels.

The difference images of an insulating rod in a conductive background (figure 5.4) feature a region of positive conductivity immediately surrounding the image of the rod. As the saline filled tank was included in the reference measurements, its positive contribution to the reconstructed conductivity should have been negated. One possible explanation is that the truncation of the sensitivity matrix (and hence removal of some basis information) is the cause.

5.3. Low-contrast distributions

The conductivity of biological tissue at 10 MHz spans the range 0.01 to 2 S/m (chapter 1). The wide range of different tissue types can be broadly classified into two categories:- low water content ($\sigma < 0.1$ S/m) and high water content tissue (0.1 S/m $< \sigma < 2$ S/m). Biological samples will exhibit lower conductivity contrasts than considered in section 5.2, which will result in smaller changes in measured magnetic field phase. This poses less of a challenge for linear reconstruction algorithms (which are more effective for smaller perturbations),

but more of a challenge for the MIT hardware to achieve the larger required signal-to-noise ratio.

Low-contrast conductivity phantoms have been constructed by immersing agar columns into a saline-filled tank. The columns were created by mixing agar powder (Novara Group Ltd) with saline, and placing in a cylindrical mould until set. The agar columns were stored in saline solution of the same conductivity; columns of conductivity 0.2, 0.5, 0.8, 1.2, 1.5, and 2.0 S/m were created.

5.3.1. Absolute imaging

As in 5.2.1, the free-space sensitivity matrix described in chapter 4 has been used for low-contrast absolute images (truncated to the largest 70 singular values), along with a non-negativity condition. The same conductivity normalisation scheme used in 5.2 was used here.

5.3.1.1. Agar conductivity phantoms 1

A low-contrast conductivity phantom was created using a 20cm diameter tank filled with saline of conductivity 0.3 S/m to a depth of 8cm. Into this was placed an 8cm high, 4cm diameter agar column of conductivity 1.0 S/m, at five different displacements along the negative y-axis; 0cm, 2cm, 4cm, 6cm and 8cm from the centre. The conductivity values of the saline and the agar are loosely representative of white matter (0.2 S/m) and blood (1.5 S/m) at 10 MHz respectively (chapter 1). This phantom contains a conductivity contrast of roughly the magnitude encountered in a brain haemorrhage.

The images reconstructed for absolute measurements made on the phantom described above are shown in figure 5.5. The original positions of the columns are shown by the white circles, the tank perimeter is represented by the thin black circles, and the position of the receiver coils is shown by the thicker black circle. All reconstructed features outside the tank region have been set to zero.

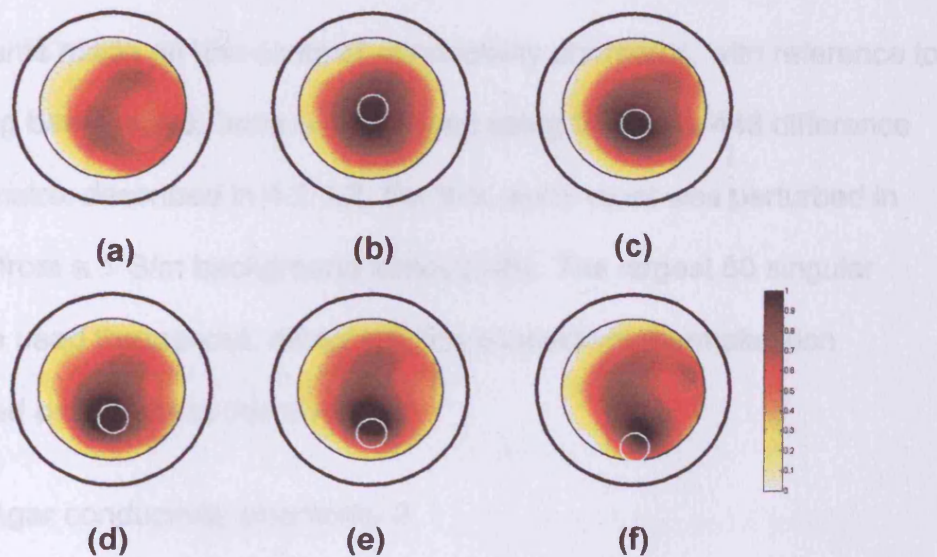


Figure 5.5. ABOLUTE MEASUREMENTS, FREE-SPACE SENSITIVITY MATRIX. Absolute images of a 20cm diameter saline-filled tank (0.3 S/m) containing an agar column (1.0 S/m) of diameter 4cm. The column was positioned along the y-axis at displacements of 0cm (b), -2cm (c), -4cm (d), -6cm (e) and -8cm(f) from the centre. Image (a) is of the saline tank without the column. All six images are normalised to the greatest magnitude conductivity value, 17.5 S/m.

The blacker regions of the image represent the agar column, while the saline tank is the surrounding red/yellow region. For the more centrally located perturbations (images b and c) the agar is reconstructed in approximately the original position, but the diameter is reconstructed as larger than the actual column diameter (based on FWHM). As the perturbation is positioned closer to the periphery (images d, e and f), the original location is less accurately

reconstructed, although the reconstructed column diameter becomes smaller. Image (a) is of the tank without the agar column. In all images, to varying extents, there are areas of zero conductivity (shown as white) inside the left side tank perimeter. The reconstructed images are asymmetrical about both the x and y axes.

5.3.2. Difference imaging

Measurements made on low-contrast conductivity phantoms, with reference to a conducting background, have been imaged using the 240 x 448 difference sensitivity matrix described in 4.2.1.2. For this, each voxel was perturbed in turn by 1% from a 1 S/m background conductivity. The largest 60 singular values were used throughout, along with the conductivity normalisation scheme used previously in this chapter.

5.3.2.1. Agar conductivity phantoms 2

Low-contrast conductivity phantoms were constructed, incorporating the range of conductivity values exhibited by high water content biological tissue at 10 MHz ($0.1 \text{ S/m} < \sigma < 2 \text{ S/m}$). A 24cm diameter tank was filled to a depth of 8cm with 1 S/m saline solution. Agar cylinders of diameter and height 8cm were created having conductivities 0.2, 0.5, 0.8, 1.2, 1.5, and 2.0 S/m. When inserted into the saline filled tank, these agar columns represented conductivity perturbations of -80%, -50%, -20%, +20%, +50% and +100%. For each case, the agar cylinders were positioned at displacements of 0cm, 4cm and 8cm along the +x-axis from the centre of the tank. Reference measurements were made with the saline-filled tank in place. Figure 5.6

shows the images reconstructed from these measurements. For each row of images, the original displacement of the agar sample is (left to right) 0cm, 4cm, and 8cm along +x-axis (shown on the images by the small black circles).

As with previous images, the smallest black circle represents agar column size and position, the perimeter of the 24cm diameter tank is shown by the larger inner circle, while the receiver coil positions are illustrated by the thicker outer circle.

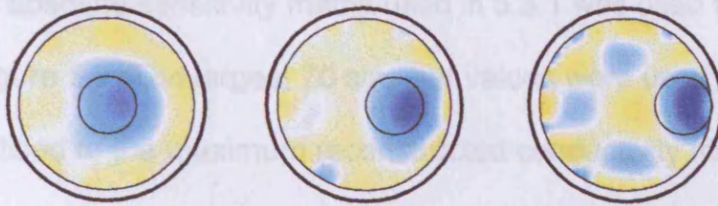
5.3.3. Difference imaging with a free-space sensitivity matrix

Another variation on the previously investigated methods of reconstructing images exists; that of using difference measurements (as considered in 5.3.2) with a free-space sensitivity matrix (as used in 5.3.1).

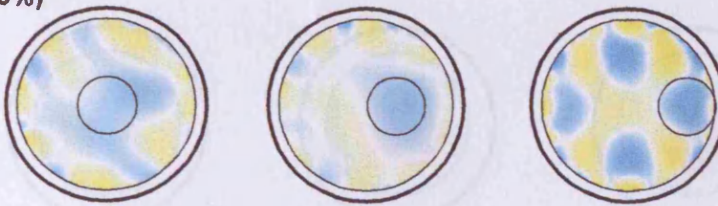
5.3.3.1. Agar conductivity phantoms 1

The phantoms used in 5.3.1 (figure 5.5) to produce a 1 S/m column perturbation within a 0.3 S/m conductivity background have been used to produce difference images, with reference to the 0.3 S/m background. The 1% difference sensitivity matrix used in section 5.3.2 was unsuitable for reconstructing images from these measurements due to the relative magnitude of the perturbation (+233%), even though it was previously used to reconstruct +100% perturbations.

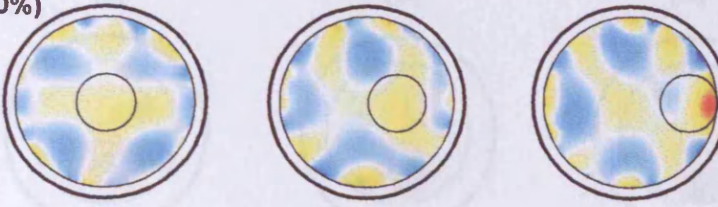
0.2 S/m (- 80%)



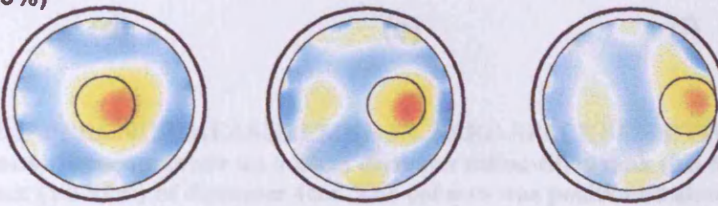
0.5 S/m (- 50%)



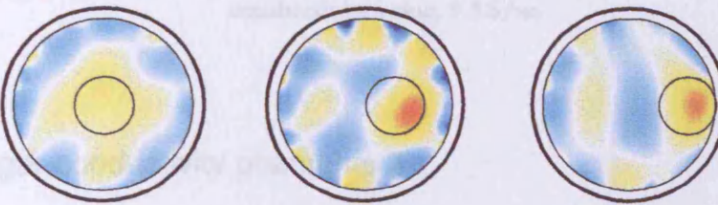
0.8 S/m (- 20%)



1.2 S/m (+ 20%)



1.5 S/m (+ 50%)



2.0 S/m (+ 100%)

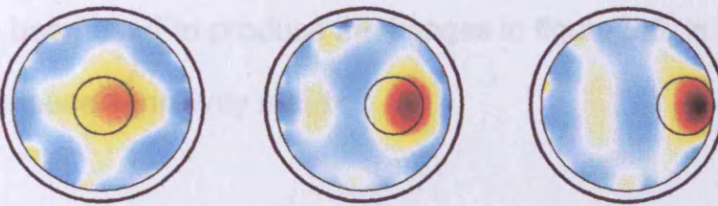


Figure 5.6. DIFFERENCE MEASUREMENTS, DIFFERENCE SENSITIVITY MATRIX. Conductivity images reconstructed from experimental measurements made on an agar cylinder, of diameter and height 8cm, at three positions within a 1 S/m saline tank. Each row of images corresponds to a different conductivity value, from top to bottom: 0.2, 0.5, 0.8, 1.2, 1.5 and 2.0 S/m. All images are normalised to the greatest magnitude conductivity value, 2.95 S/m.

Instead, the absolute sensitivity matrix used in 5.3.1 was used to produce the images in figure 5.7. The largest 70 singular values were used, and all images were normalised to the maximum reconstructed conductivity magnitude.

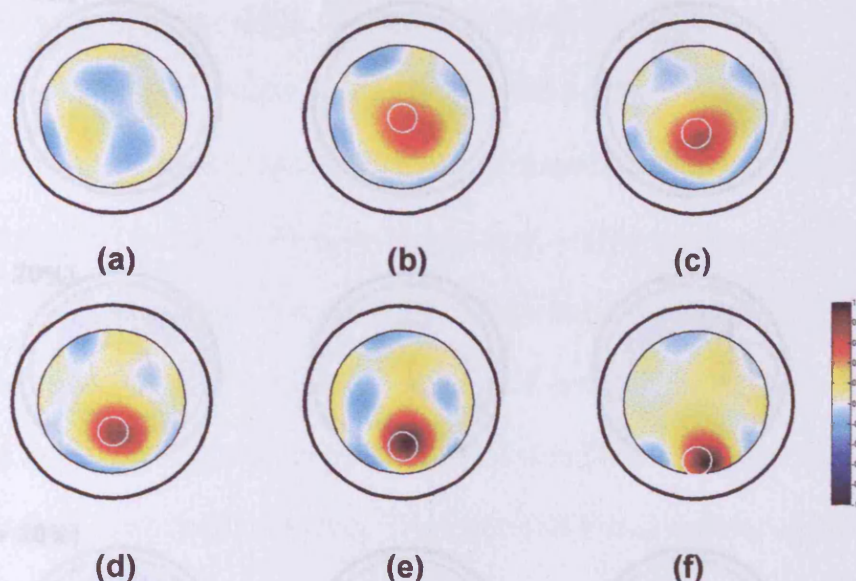


Figure 5.7. DIFFERENCE MEASUREMENTS, FREE-SPACE SENSITIVITY MATRIX . Images from measurements made on a 20cm diameter saline-filled tank (0.3 S/m) containing an agar column (1.0 S/m) of diameter 4cm. The column was positioned along the y-axis at displacements of 0cm (b), -2cm (c), -4cm (d), -6cm (e) and -8cm (f) from the centre. Image (a) is of the saline tank without the column. All six images are normalised to the greatest magnitude conductivity value, 9.3 S/m.

5.3.3.2. Agar conductivity phantoms 2

The difference measurements made on the conductivity phantom discussed in 5.3.2.1 have been used to produce the images in figure 5.8, in conjunction with the free-space sensitivity matrix.

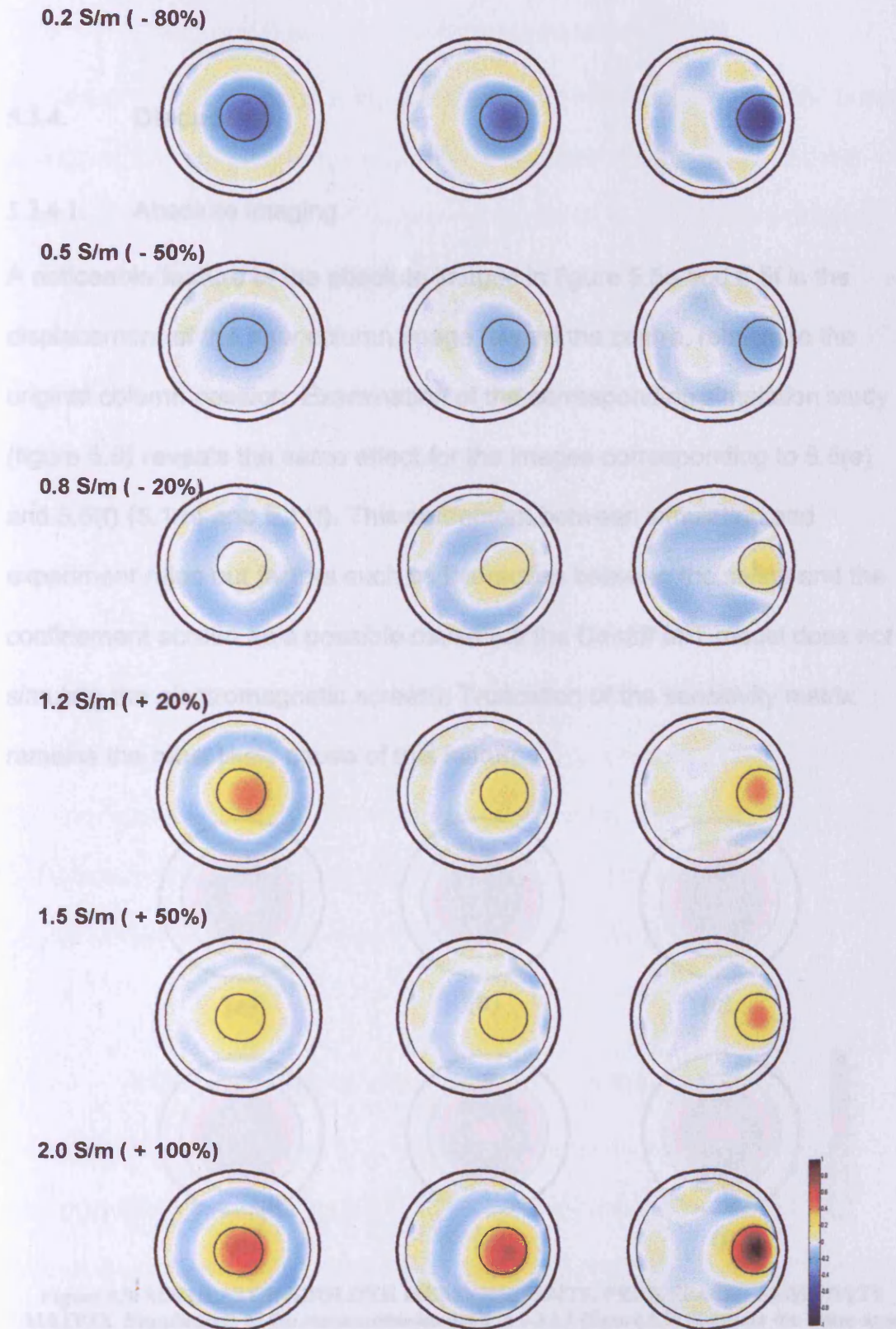


Figure 5.8. DIFFERENCE MEASUREMENTS, FREE-SPACE SENSITIVITY MATRIX . Images of the same measurements used to produce figure 5.6, but here the free-space sensitivity matrix is used to reconstruct the images. All images are normalised to the greatest magnitude conductivity value, 30 S/m.

5.3.4. Discussion

5.3.4.1. Absolute imaging

A noticeable feature of the absolute images in figure 5.5e and 5.5f is the displacement of the agar column image toward the centre, relative to the original column position. Examination of the corresponding simulation study (figure 5.9) reveals the same effect for the images corresponding to 5.5(e) and 5.5(f) (5.11e and 5.11f). This agreement between simulation and experiment rules out factors such as interaction between the saline and the confinement screen as a possible cause (as the Cardiff MIT model does not simulate the electromagnetic screen). Truncation of the sensitivity matrix remains the most likely cause of this feature.

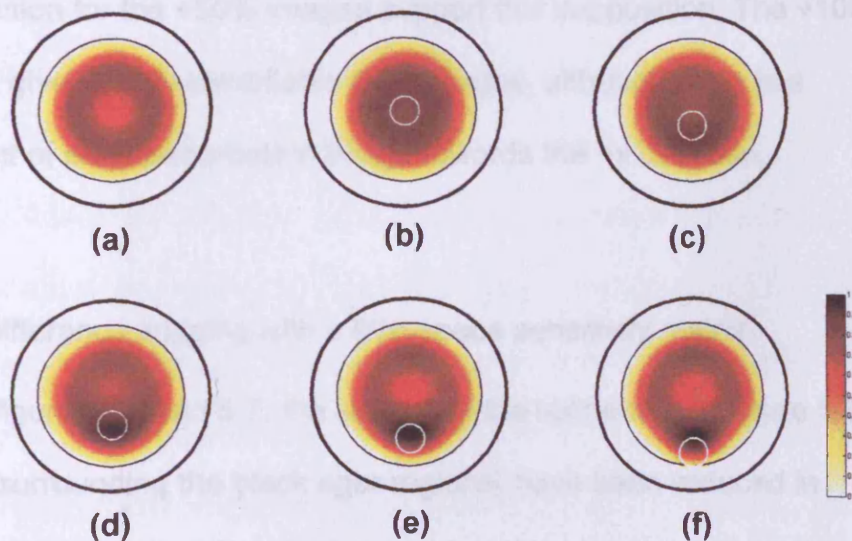


Figure 5.9. SIMULATED ABOLUTE MEASUREMENTS, FREE-SPACE SENSITIVITY MATRIX. Simulations of the measurements used in 5.3.1.1 (figure 5.5) illustrate the same agar image displacement towards the centre of the detector volume. All images are normalised to the maximum value of 9.0 S/m.

5.3.4.2. Difference imaging with difference sensitivity matrix

Considering the difference images in figure 5.6, the -80% perturbation images represent the original conductivity distribution reasonably well, at all three positions. However, the agar images are displaced slightly from their actual positions. As encountered in previous sections in this chapter, there is some reduction in the magnitude of the agar image as its location becomes more central. The -50% and -20% images were less than satisfactory. For the -50% case, only the 8cm position displayed an image of the agar perturbation; however the image contained artefacts of comparable magnitude. The '8cm' image of -20% case appears to display small positive conductivity changes, contrary to the phantom's composition. The quality of the $+50\%$ images is poorer than for the $+20\%$ case, suggesting that random measurement noise was more significant in the former set. The image artefacts at the periphery of the 4cm position for the $+50\%$ images support this supposition. The $+100\%$ perturbation gives easily identifiable agar images, although there is a displacement of each perturbation image towards the $+x$ direction.

5.3.4.3. Difference imaging with a free-space sensitivity matrix

Comparing figures 5.5 and 5.7, the images of the saline tank in figure 5.5 (the red regions surrounding the black agar regions) have been reduced in magnitude in figure 5.7 by making the reference measurements with the tank present. Consequently, there is a greater contrast between the agar column and surrounding region in figure 5.7 compared with figure 5.5. Also, the displacement of the agar image towards the tank centre in 5.5(e) and (f) is not a feature of 5.7(e) and (f). The possibility that the displacement effect may

have been a consequence of screen-saline interaction (and that having the saline tank present for both reference and perturbed measurement sets removed that influence from the difference images), must be ruled out by the fact that the same displacement effect is present in images of simulated absolute measurements (5.3.4.1) that do not model the confinement screen.

Use of the free-space sensitivity matrix in reconstructing images from the difference measurements described in 5.3.2.1 (originally reconstructed using a difference sensitivity matrix) results in a number of small imaging improvements, manifested in the images in figure 5.8. Comparison with figure 5.6 shows that the 0.2 S/m perturbation images for the 0cm and 4cm positions represent the original agar positions more accurately. Also, the image distortion for the 8cm position is significantly reduced when the free-space sensitivity matrix is used.

The ability of the free-space sensitivity matrix to produce difference images of superior quality than the difference sensitivity matrix can be investigated with the aid of phase change versus measurement number (transmitter-receiver combination) plots. Figure 5.10 shows a sample of the experimental absolute phase changes ('EXP ABS') described in 5.3.1.1 (a 1 S/m agar column in a 0.3 S/m saline-filled tank – figure 5.5f), along with simulated absolute phase changes ('SIM ABS') for the same conductivity distribution. Random noise was added to 'SIM ABS', as in chapter 4. To allow comparison of the general shape of the profiles, both sets have been normalised to their respective greatest magnitude values (the ratio of the largest magnitude experimental value to the corresponding simulated value is 2.11). For clarity, only 120 of the 240 measurements have been shown.

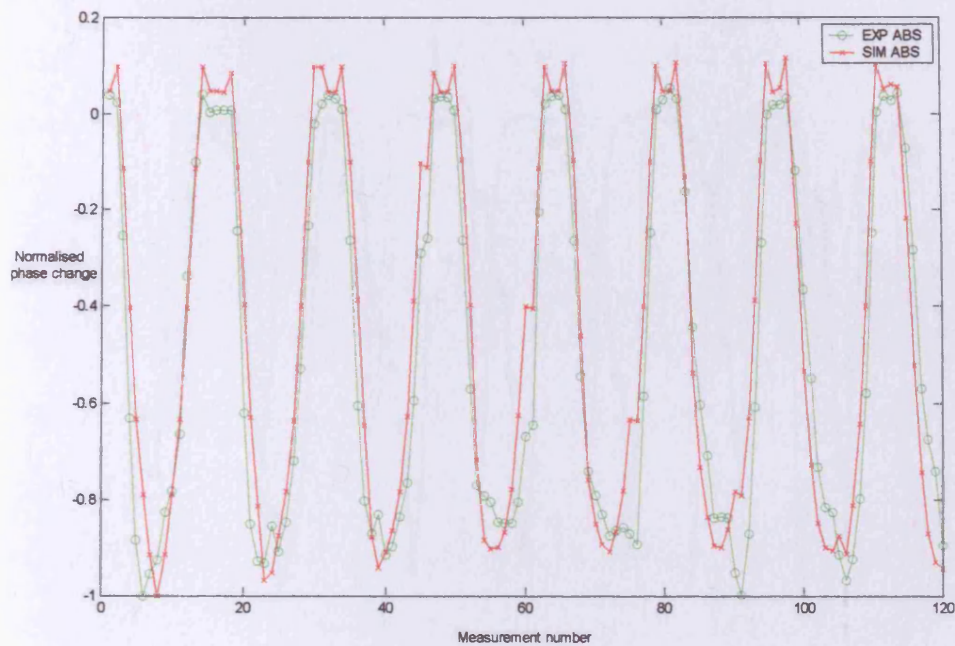


Figure 5.10. Experimental (EXP ABS) and simulated (SIM ABS) absolute normalised phase changes (including simulated noise) for images used in 5.3.1.1.

The shape of the measurement profiles are in good agreement, i.e. the measurements with the greatest magnitude occur at approximately the same measurement number (and hence transmitter-receiver combination). On comparing the experimental difference measurements described in 5.3.3.1 with simulations of the same scenario (normalising as previously, the ratio of the maximum values is 3.83), it becomes apparent that there is some discrepancy between the two sets (figure 5.11). The simulated values of greatest magnitude appear at significantly different transmitter-receiver combinations than their experimental counterparts.

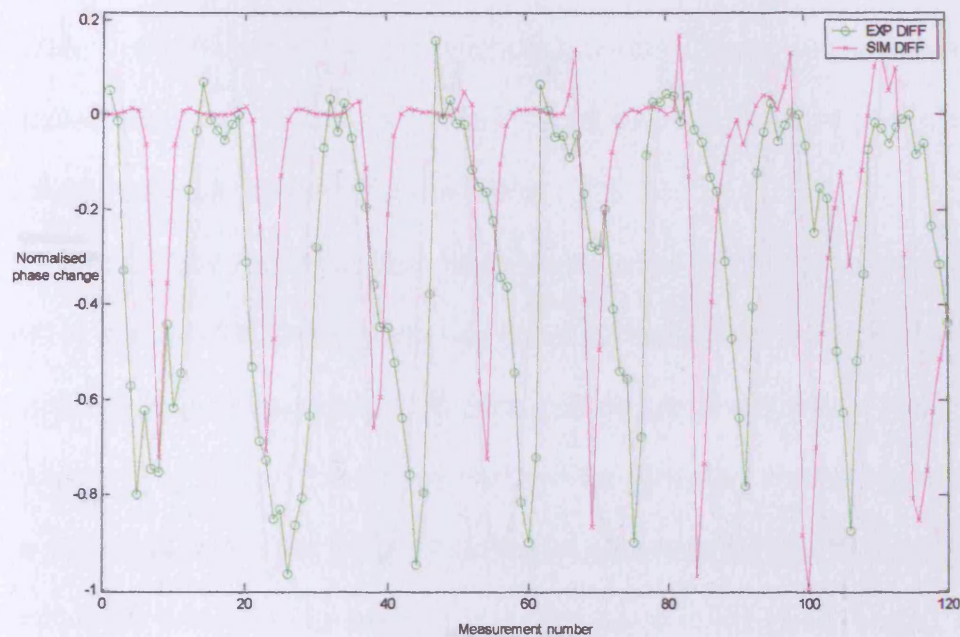


Figure 5.11. Experimental (EXP DIFF) and simulated (SIM DIFF) difference normalised phase changes for images used in 5.3.1.1.

Placing the simulated absolute measurements (red plot in figure 5.10) and experimental difference measurements (green plot in figure 5.11) on the same graph (figure 5.12) suggests a possible reason why the absolute sensitivity matrix reconstructs difference images more effectively than the difference matrix; there is a closer correlation between the experimental difference and simulated absolute measurements than between the experimental and simulated difference measurements. However, the agreement is still poor, and further research is needed before any firm conclusions can be made.

5.3.2.1 will be investigated in this section. Simulation studies presented in chapter 3 illustrated that successful image reconstructions were only possible when conductivity distributions that were of the same extent in the z-direction as the sensitivity matrix voxels

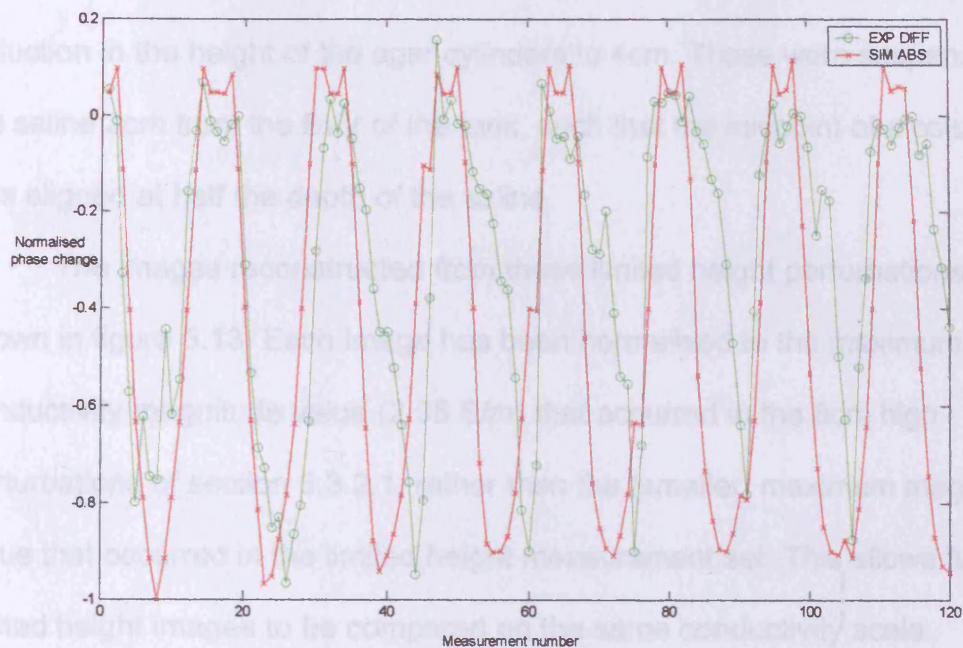


Figure 5.12. Experimental (EXP DIFF) difference and simulated (SIM ABS) absolute normalised phase changes for images used in 5.3.1.1.

It is possible that factors not included in the Cardiff MIT model are the cause of the discrepancies between experimental and simulated difference measurements; the aluminium confinement screen being one possibility.

5.3.5. Limited height perturbations

5.3.5.1. Difference imaging with a difference sensitivity matrix

The effect of reducing the height of the agar perturbations used in section 5.3.2.1 will be investigated in this section. Simulation studies presented in chapter 3 illustrated that successful image reconstructions were only possible with conductivity distributions that were of the same extent in the z-direction as the sensitivity matrix voxels.

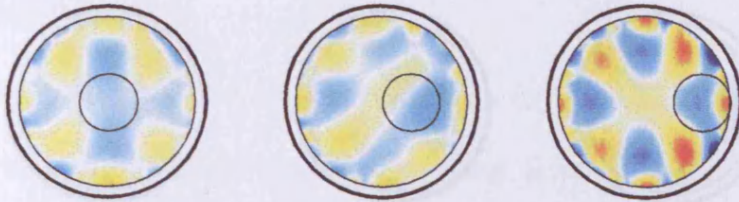
The phantoms used in 5.3.2.1 were reproduced identically, except for a reduction in the height of the agar cylinders to 4cm. These were suspended in the saline 2cm from the floor of the tank, such that the midpoint of a column was aligned at half the depth of the saline.

The images reconstructed from these limited height perturbations are shown in figure 5.13. Each image has been normalised to the maximum conductivity magnitude value (2.95 S/m) that occurred in the 8cm high perturbations of section 5.3.2.1, rather than the (smaller) maximum magnitude value that occurred in the limited height measurement set. This allows full and limited height images to be compared on the same conductivity scale.

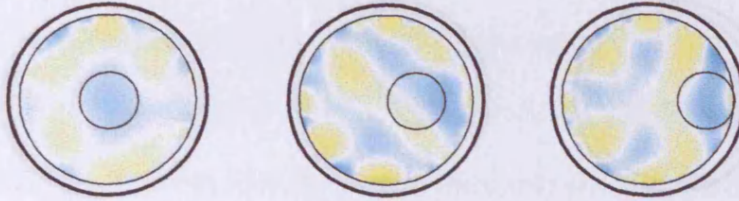
5.3.5.2. Difference imaging with a free-space sensitivity matrix

The difference measurements made on limited height perturbations, used in the previous section, have been used with the absolute sensitivity matrix to produce the images in figure 5.10. The images have been normalised to the maximum conductivity magnitude value that occurred in the full height perturbation measurement set, in section 5.3.3.2 (30 S/m).

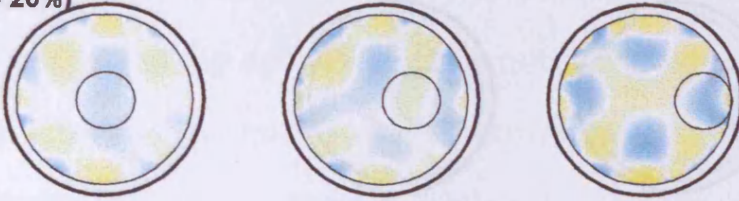
0.2 S/m (- 80%)



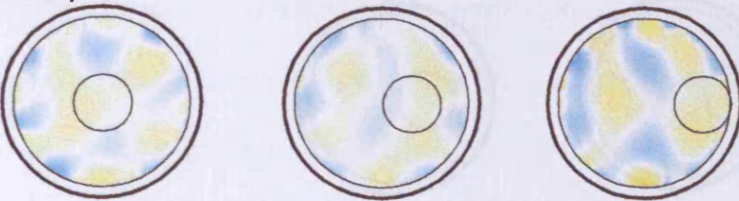
0.5 S/m (- 50%)



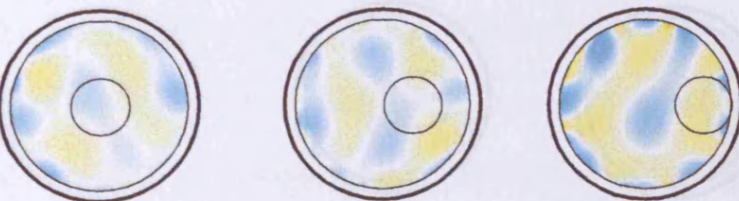
0.8 S/m (- 20%)



1.2 S/m (+ 20%)



1.5 S/m (+ 50%)



2.0 S/m (+ 100%)

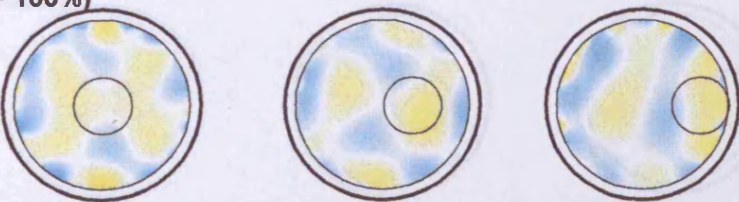
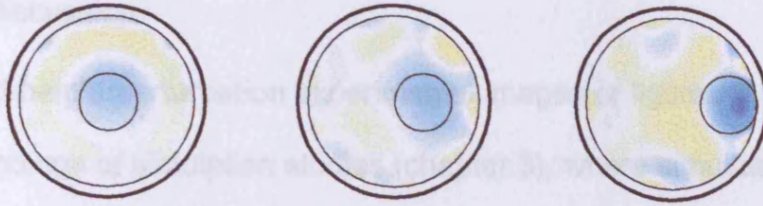
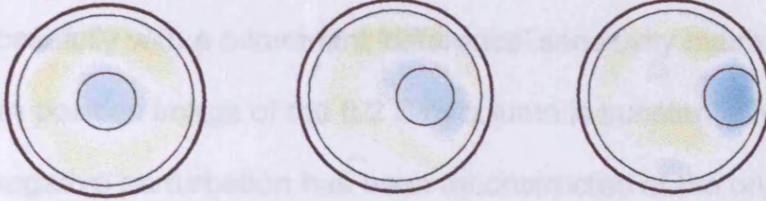


Figure 5.13. DIFFERENCE MEASUREMENTS, DIFFERENCE SENSITIVITY MATRIX. Conductivity images reconstructed from experimental measurements made on an agar cylinder, of diameter 8cm and height 4cm, at three positions within a 1 S/m saline tank. Each row of images corresponds to a different conductivity value, from top to bottom: 0.2, 0.5, 0.8, 1.2, 1.5 and 2.0 S/m.

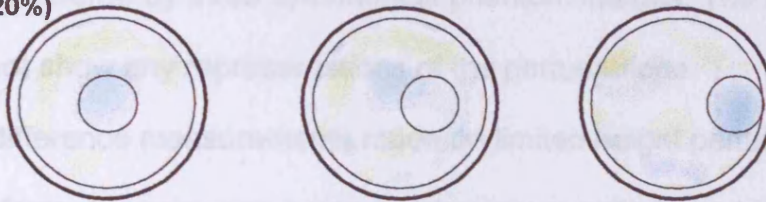
0.2 S/m (- 80%)



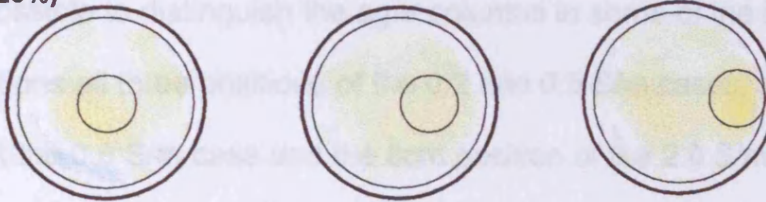
0.5 S/m (- 50%)



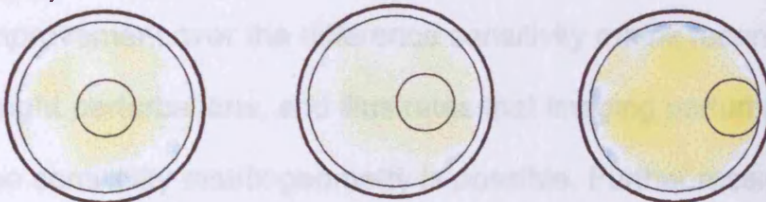
0.8 S/m (- 20%)



1.2 S/m (+ 20%)



1.5 S/m (+ 50%)



2.0 S/m (+ 100%)

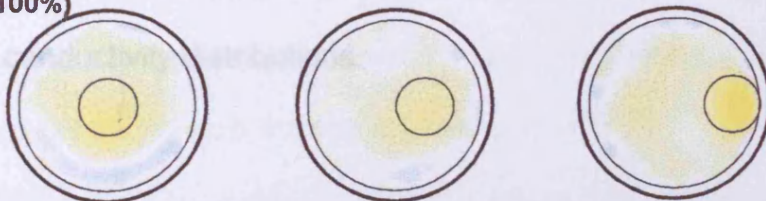


Figure 5.14. DIFFERENCE MEASUREMENTS, FREE-SPACE SENSITIVITY MATRIX.
Images of the limited height perturbation measurements used to produce figure 5.13.

5.3.5.3. Discussion

The reduced height perturbation experimental images of figures 5.13 and 5.14 mimic the findings of simulation studies (chapter 3), where simulated measurements made on limited height conductivity perturbations could not be imaged successfully with a z-invariant 'difference' sensitivity matrix. In figure 5.13, the 8cm position image of the 0.2 S/m column is substantially distorted; although a negative perturbation has been reconstructed at the original agar position, it is mirrored by three symmetrical phantom images. The remaining images do not show any representations of the perturbations.

The difference measurements made on limited height perturbations also benefit from reconstruction using an absolute sensitivity matrix (figure 5.14). It is possible to distinguish the agar columns in some of the images, namely positions all three positions of the 0.2 and 0.5 S/m cases, and to a lesser extent the 0.8 S/m case and the 8cm position of the 2.0 S/m case. The use of the free-space sensitivity matrix in the reconstruction process shows a significant improvement over the difference sensitivity matrix reconstructions for limited height perturbations, and illustrates that imaging perturbations that differ from the sensitivity matrix geometry is possible. Further research is needed to determine how successful this method is in reconstructing more complicated conductivity distributions.

5.3.6. Summary and conclusions

The Cardiff MIT measurement system has been used, in conjunction with a linear reconstruction algorithm, to produce images of various conductivity phantoms. Normalised absolute and difference images of high and low contrast conductivity distributions were reconstructed using a sensitivity matrix method reconstruction algorithm. One notable outcome of the investigation was that the absolute sensitivity matrix (calculated for isolated columns of 1 S/m) produced reasonable conductivity images for both absolute and difference measurements. In fact, it produced better quality images of difference measurements (5.3.3.2) for low contrast perturbations than the difference sensitivity matrix (calculated for 1% perturbations on a 1 S/m background, 5.3.2.1).

Even though the image voxels used in the sensitivity matrix calculations were extended in the z-direction, it was still possible to reconstruct images from some experimental measurements made on perturbations with limited 'height' (5.3.5.3). However, this constraint is a limiting factor, and should be addressed in future studies by calculation of three-dimensional sensitivity matrices. The volume resolution possible with a 16 channel system may be limited, and additional measurement channels may be required to increase the number of independent measurements available (and hence improve the volume resolution).

The ability to image conductivity perturbations that are representative of a brain haemorrhage (5.3.1.1) is encouraging, particularly as this was achieved with reference to free-space. However, conductivity phantoms that

represent the human anatomy more realistically need to be used in future studies.

The magnitude of the absolute conductivity reconstructed using the free-space sensitivity matrix in 5.2.1.1 (26.2 S/m) was approximately 30 times larger than the original conductivity (0.9 S/m). This was also true for the difference images in 5.3.3.2; the largest reconstructed value was 30 S/m for a conductivity change of 1 S/m. In both cases, the sample diameter was approximately 8cm. When the volume of the perturbations used in 5.3.3.2 were reduced to half (5.3.5.2), the largest reconstructed conductivity value fell by approximately one-third to 10 S/m. The largest conductivity values reconstructed from experimental (5.3.1.1) and simulated (5.3.4.1) absolute measurements of the distribution described differed by a factor of approximately 2 (9.0 S/m compared with 17.5 S/m respectively).

The relationships between actual and reconstructed conductivity magnitude and spatial extent need to be characterised for difference and free-space sensitivity matrices in further research.

5.4. References

Korjenevsky A, Cherepenin V, Sapetsky S, 2000, Magnetic induction tomography : experimental realisation. *Physiol. Meas.*, vol. **21**, no. 1, p. 89-94

Watson S, Williams RJ, Gough W, Morris A, Griffiths H, 2002, The Cardiff magnetic induction tomography system. *Proc. Int. Med. Fed. Biol. Eng. EMBEC02, Vienna, Austria, Dec. 4-8*, ISBN 3-901351-62-0, vol. **3** (1), p. 116-117

6. Wave propagation delays in MIT

6.1. Introduction

MIT images of a sample's conductivity are effectively reconstructed from measurements of magnetic field phase change. With no sample present in the detector, the transmitter coils will induce an emf in the receiver coils, known as the primary signal. When a sample is placed in the detector, the transmitter coils induce eddy currents within the sample. These eddy currents produce their own magnetic fields, which in turn induce an emf in the receiver coils. There is a contribution to this emf from the permittivity of the sample (which is in phase with the primary emf), and its conductivity (which lags the primary field by 90°).

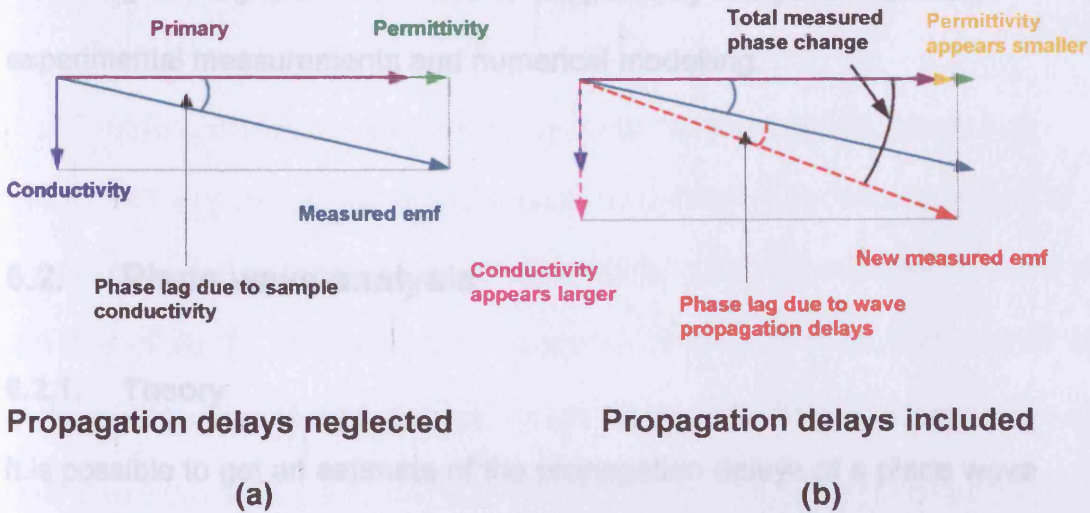


Figure 6.1. Phasor diagrams of receiver emfs without (a) and with (b) propagation delays included. The phase lag introduced by propagation delays cause the contributions from the conductivity and permittivity of the sample to appear different to their actual values.

The phase difference between the resulting emf and the primary emf can be used to reconstruct the original conductivity distribution. The phasor diagram shown in figure 6.1(a) illustrates this concept (note that the sizes of the permittivity and conductivity emf contributions are exaggerated for clarity). There will also be a phase lag due to the fact that electromagnetic waves travel more slowly in biological tissue than in air (as tissue has a larger permittivity than air). This propagation delay phase lag is indistinguishable from the phase lag due to conductivity, and so significant propagation delays would cause an incorrect representation of conductivity and permittivity, as illustrated by figure 6.1(b).

The purpose of this chapter is to estimate the magnitude of phase lags due to wave propagation delays encountered in biomedical MIT, and to comment on the suitability of the widespread, quasi-static approach to modelling MIT signals. This will be investigated by analytical methods, experimental measurements and numerical modelling.

6.2. Plane wave analysis

6.2.1. Theory

It is possible to get an estimate of the propagation delays of a plane wave travelling in a material, relative to the propagation delays in air, using the elementary analysis described below.

Consider a plane wave propagating over a distance r in air ($\epsilon_r = 1$, $\mu_r = 1$), at a phase velocity $c = 3 \times 10^8$ m/s. The time taken to travel this distance is given by

$$t_{air} = \frac{r}{c} \quad (6.2.1)$$

This corresponds to a phase delay of

$$\theta_{air} = \frac{\omega r}{c} = \frac{r}{\lambda} \quad (6.2.2)$$

where λ is the wavelength divided by 2π . For a plane wave travelling through a material with relative permittivity ϵ_r (magnetic permeability is considered to be 1, as for biological tissue), the propagation is slowed by a factor of the square root of ϵ_r .

$$t_{material} = \frac{r\sqrt{\epsilon_r}}{c} \quad (6.2.3)$$

$$\theta_{material} = \frac{r\sqrt{\epsilon_r}}{\lambda} \quad (6.2.4)$$

The phase lag between propagation in air and propagation in a material is

$$\theta_{diff} = \frac{(\sqrt{\epsilon_r} - 1)r}{\lambda} \quad (6.2.5)$$

This simple analysis can be used to estimate the propagation delays in a typical MIT application. Biological tissues have relative permittivity values of as much as 400 at 10MHz (Gabriel *et al* 1996). Using an economical value of 80 (that of water), and assuming propagation through a 10cm thickness of this material, equation (6.2.5) predicts a phase lag of 10° . This is substantially more than the equivalent conductivity eddy current phase (approximately 1° for 1 S/m; Griffiths *et al* 1999). This theoretical value of propagation delay is in stark contrast to single channel experimental measurements made on a 9cm thickness of de-ionised water reported by Griffiths *et al* (1999), in which no

phase change was detected above the 0.1° uncertainty due to baseline drifting.

6.2.2. Previous Work

The subject of wave propagation delays in MIT has been considered by Gencer and Tek (1998). The authors presented the governing electromagnetic equations (chapter 2), and derived a solution for the magnetic vector potential \mathbf{A} due to a current density \mathbf{J} , of the form

$$\mathbf{A} = \frac{\mu}{4\pi} \int \frac{\mathbf{J} e^{j\left(\omega t - \frac{r}{\lambda}\right)}}{r} dV \quad (6.2.6)$$

where r is the distance between the source and field point. This is referred to as the retarded potential, due to the propagation delay effect being described by the $e^{-j\frac{r}{\lambda}}$. Replacing this delay term by unity results in the magnetic vector potential for the quasi-static case. The authors calculated the percentage difference of the exponential term from unity, for typical biological values of conductivity and permittivity at frequencies up to 100 kHz. The resulting values of this percentage error seemed to indicate that, for a propagation distance of 20cm, the 'delay effect' exponential term could be replaced by unity for frequencies up to 100 kHz. In other words, propagation delays could be neglected in biomedical applications of MIT, for operating frequencies up to 100 kHz. This analysis is misleading in that it does not consider the 'r' term in the denominator of equation (6.2.6). The full integral needs to be evaluated in order to obtain an accurate understanding of the situation.

6.3. Near field analysis

6.3.1. Introduction

The simple analysis used in section 6.2 considered the propagation of plane waves. The approximation to plane waves is valid for most sources in the far-field ($r \gg \lambda$). However, the wavelength of electromagnetic waves at 10MHz in free space is 30m, and in biological tissue can be as little as 1.5m. The maximum distance between transmitter and receiver coils likely to be encountered in biomedical MIT is 30cm, which is therefore in the near-field ($r \ll \lambda$). Thus the plane wave assumption has no validity, and a more realistic analysis is required.

6.3.2. Magnetic dipole radiation

A convenient starting point for a near-field analysis is the equation for magnetic-dipole radiation to be found in most standard texts. Considering a transmitter coil as a magnetic dipole of moment $\mathbf{m}_0 e^{j\omega t}$, the magnetic vector potential at a distance r from the coil is

$$\mathbf{A} = \frac{\mu_0}{4\pi} \frac{\mathbf{m}_0 \times \mathbf{r}_1}{r\lambda} \left(\frac{\lambda}{r} + j \right) e^{j\left(\omega t - \frac{r}{\lambda}\right)} \quad (6.3.1)$$

where \mathbf{r}_1 is the unit vector in the direction of r (Lorrain and Corson 1970). For the near field case ($r \ll \lambda$), the exponential term $e^{-\frac{jr}{\lambda}}$ can be replaced by a Taylor series expansion (Gough 2001)

$$1 - j \frac{r}{\lambda} - \frac{r^2}{2\lambda^2} + \dots \quad (6.3.2)$$

Substituting into equation (6.3.1) gives

$$\mathbf{A} = \frac{\mu_0}{4\pi} \frac{\mathbf{m}_0 \times \mathbf{r}_1}{r^2} \left\{ \left(1 + \frac{r^2}{2\lambda^2} \right) - j \frac{r^3}{3\lambda^3} \right\} \quad (6.3.3)$$

and neglecting the second order term leaves

$$\mathbf{A} \approx \frac{\mu_0}{4\pi} \frac{\mathbf{m}_0 \times \mathbf{r}_1}{r^2} \left\{ 1 - j \frac{r^3}{3\lambda^3} \right\} \quad (6.3.4)$$

The phase change due to the propagation delay is given by the imaginary term, which has an $\frac{r^3}{\lambda^3}$ dependence. In the near field, the first order imaginary terms in equations (6.3.1) and (6.3.2) cancel, leaving a much smaller phase change due to the propagation delay than was indicated in 6.2.1. In fact, this leads to the surprising conclusion that the phase velocity is greater than c in the near field, and that the propagation speed approaches infinity as r approaches zero. Similar behaviour is described by Feynman *et al* (1964), in an analysis, developed from first principles, of the magnetic field of an electric dipole.

This analysis is expanded by Gough (2002), who describes a more general treatment by considering the propagation of non-spherically symmetric waves relevant to electric and magnetic dipole radiation¹.

¹ It should be noted that Gough also analysed the propagation of a step function, and found that it travelled at the speed of light. This is consistent with the theory that information cannot be transmitted faster than light.

6.3.3. Transmitter coil radiation

In MIT, the spatial extent over which electromagnetic field interactions are relevant is usually of the same order as the diameter of the coils involved. It is therefore more realistic to consider the finite size of the coils in any analysis, rather than an approximation to a magnetic dipole.

For a circular coil of radius 'a' carrying steady current 'I', the magnetic vector potential **A** at a position (r, θ) from the coil centre is

$$A = -\frac{\mu_0 I a}{\pi \sqrt{(a^2 + r^2 + 2ar \sin \theta)}} \left(\frac{(2 - k^2)K(k) - 2E(k)}{k^2} \right) \quad (6.3.5)$$

where $k^2 = 4ar \sin \theta (a^2 + r^2 + 2ar \sin \theta)$, and K(k) and E(k) are the complete elliptic integrals of the first and second kinds respectively (Jackson 1988). If the steady current is replaced by an alternating current of frequency ω, the equation for A is

$$A = \frac{\mu_0 I a}{4\pi} e^{j\omega t} \int_0^{2\pi} \frac{\cos \phi}{\rho} e^{-\frac{j\omega \rho}{c}} d\phi \quad (6.3.6)$$

where $\rho = \sqrt{a^2 + r^2 - 2ar \sin \theta \cos \phi}$. Assuming the near field case $\left(\rho \ll \frac{c}{\omega} \right)$,

and expanding the exponential term to third order gives

$$A = \frac{\mu_0 I a}{4\pi} e^{j\omega t} \int_0^{2\pi} \frac{\cos \phi}{\rho} \left(1 - \frac{\rho^2}{2\lambda^2} + j \frac{\rho^3}{6\lambda^3} \right) d\phi \quad (6.3.7)$$

Considering each term separately; the first term is equation (6.3.6) multiplied by $e^{-j\omega t}$, the second term can be neglected (as it is much smaller than the first), and the third term (which is the quadrature first term, and hence describes the phase change) again has a cubed relationship with the distance from the coil. This third term can be integrated to give

$$-\frac{\mu_0 I a^2 r \sin \theta}{12 \lambda^3} j e^{j \alpha t} \quad (6.3.8)$$

and dividing this by the integrated first part of (6.3.7), and taking the inverse tangent gives the phase change α

$$\alpha = \tan^{-1} \left[\frac{ar \pi \sin \theta \sqrt{(a^2 + r^2 + 2ar \sin \theta)}}{12 \lambda^3 \left(\frac{(2 - k^2)K(k) - 2E(k)}{k^2} \right)} \right] \quad (6.3.9)$$

This equation for the phase change due to wave propagation delays has been evaluated for a typical MIT scenario, by implementing equation (6.3.9) in Matlab. For a coil of diameter 5cm, the phase change across a 20cm² area in an x-y plane through the centre of the coil, is shown in figure 6.2. A relative permittivity value of 80 was used; that of water at 10MHz.

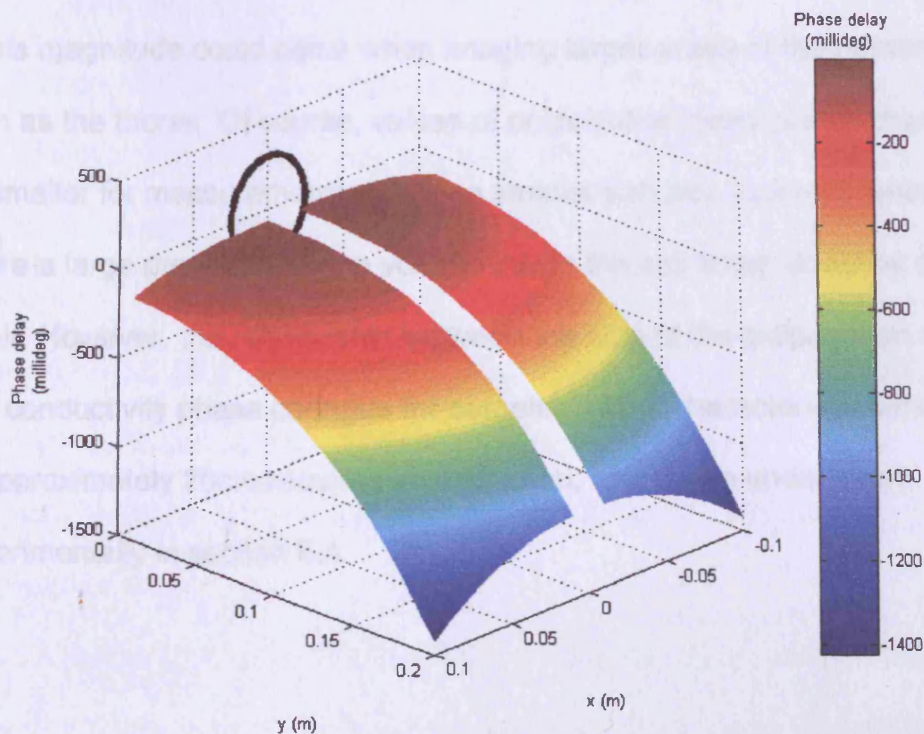


Figure 6.2. The propagation delay phase change in two dimensions due to a 5cm diameter coil (black circle) in water at 10MHz.

Figure 6.2 illustrates the relatively small phase changes that occur in the near field of the coil; approximately 100 millidegrees for a 10cm distance near the coil axis compared with 10° according to the plane wave theory in 6.2.1.

6.3.4. Discussion

Estimating wave propagation delays in MIT using a simple plane wave analysis can lead to order of magnitude errors. The near-field of a 'dipole-like' source leads to significantly smaller propagation delays than would occur in the far-field, i.e. for plane waves. However, the magnitude of these propagation delay phase changes may still be significant when compared with conductivity phase changes. For a propagation distance of 20cm in water, figure 6.2 shows a phase change of greater than 1° ; propagation path lengths of this magnitude could occur when imaging larger areas of the human body such as the thorax. Of course, values of propagation delay phase change will be smaller for measurements made on smaller samples (such as limbs), where a large proportion of the volume inside the coil array would be occupied by air. However, the relationship between the size of the propagation delay and conductivity phase changes for samples with a characteristic dimension of approximately 20cm requires investigation, and this is undertaken experimentally in section 6.4.

6.4. Experimental measurement of propagation delays

6.4.1. Background

As mentioned in section 6.2, single channel measurements (Griffiths *et al* 1999) made on a 9cm diameter beaker of de-ionised water (< 0.001 S/m) did not result in phase changes greater than the 0.1° uncertainty due to baseline drifting. Simulation studies (Morris *et al* 2001) predicted that phase changes due to conduction eddy currents encountered in MIT could be of the order of millidegrees. This leads to a requirement for a more accurate estimation of propagation delays in MIT, as propagation phase changes of 100 millidegrees would seriously affect conductivity measurements.

6.4.2. Description

With this as motivation, measurements have been made on a sample of de-ionised water (< 0.001 S/m) and tap water (0.011 S/m) using a single channel MIT measurement system (for detailed description of the system design, the reader is referred to Gough 2002). This measurement system operates at a frequency of 8.2 MHz, and performs phase measurement by employing analogue multiplier circuitry and phase sensitive detection. This produces a D.C. voltage that is proportional to the phase difference between the source and receiver emfs.

A plastic tank with base dimensions 35cm by 33cm was filled to a depth of 12.5cm, and placed between the coils. The coaxial transmitter (8cm diameter) and receiver (6cm diameter) coils were spaced 16cm apart, with the common axis running through the centre of the tank. Faraday combs were

placed on both coils to reduce the effects of capacitive coupling. A diagram of the experimental set-up is shown in figure 6.3; the blue region represents the tap/de-ionised water. Voltage measurements were recorded with and without the sample present, and the resulting phase changes calculated. The measurement process was repeated three times for both the de-ionised and tap water.

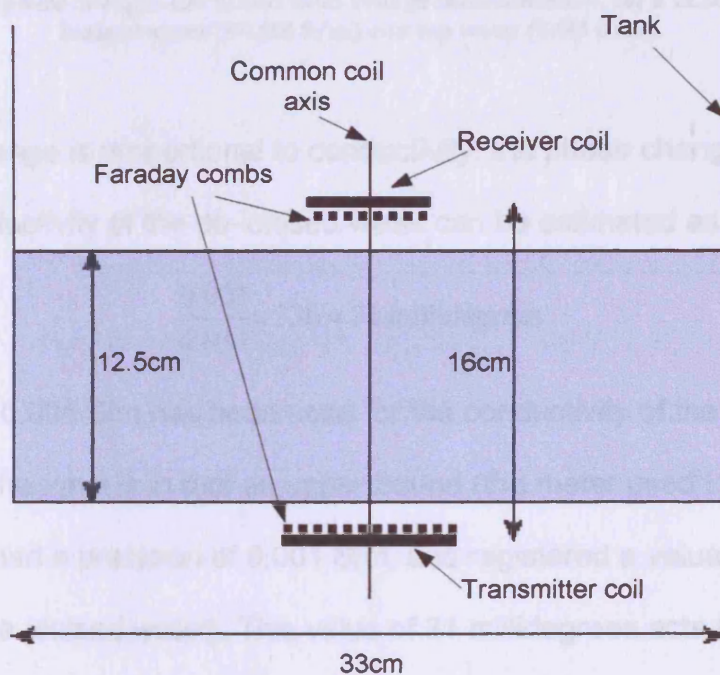


Figure 6.3. A side-on view of the experimental set-up. The blue region represents the tap/de-ionised water.

6.4.3. Results and Discussion

The phase changes calculated from measurements made on the de-ionised water (<0.001 S/m) and tap water (0.011 S/m) are shown in table 6.1. The de-ionised water illustrated an average phase change of -6 millidegrees, while the tap water resulted in the much larger average value of -336 millidegrees

(a negative phase change represents a phase lag between source and receiver).

	Phase changes (millidegrees \pm 4)			
	Measurement 1	Measurement 2	Measurement 3	Average
De-ionised	-5	-5	-8	-6
Tap	-343	-327	-339	-336

Table 6.1. The phase changes calculated from voltage measurements, for a 12.5cm depth of de-ionised water (<0.001 S/m) and tap water (0.011 S/m).

As phase change is proportional to conductivity, the phase change due to the residual conductivity of the de-ionised water can be estimated as

$$\frac{0.001}{0.011} \times 336 = 31 \text{ millidegrees}$$

The value of 0.001 S/m has been used for the conductivity of the de-ionised water, even though it is in fact an upper-bound (the meter used to measure conductivity had a precision of 0.001 S/m, and registered a value of 0.000 S/m for the de-ionised water). This value of 31 millidegrees acts a threshold for detecting propagation delays; the values of phase change measured for the de-ionised water were smaller than this, and so it can be concluded that this experiment did not observe propagation delays of the magnitude predicted by theory (approximately 200 millidegrees for a distance of 12.5cm; from section 6.3.3).

6.5. Summary and conclusions

Wave propagation delays in MIT have been investigated using analytical and experimental methods. A simple plane wave analysis of wave propagation delays in MIT has been presented (6.2). This theory predicts large values of phase lag due to wave propagation (10° over 10cm in water), but values of this size have not been observed in suitable experimental investigations (Griffiths *et al* 1999). A more appropriate near-field analysis of the magnetic field due first to a magnetic dipole (6.3.2), and then a coil (6.3.3), has been used to predict the phase delay more accurately. This work predicts a much smaller phase delay (100 millidegrees for 10cm in water), but one which is still significant in MIT. Experimental measurements made on a single-channel MIT system, with the sensitivity to measure propagation delays of the magnitude predicted by theory, have failed to do so (6.4). Watson *et al* (2003) also found little evidence of wave propagation delays in measurements made on a 12cm diameter tank of deionised water, using the Cardiff MIT measurement system. Opposing coils were used to make sets of 320 measurements of real and imaginary $\frac{\Delta V}{V}$, which were averaged to reduce the effects of phase drift. An average value of -0.013% was measured for $\frac{\Delta V}{V}$, which equates to a phase change of approximately 7 millidegrees.

Although this absence of observed propagation delay is unsatisfactory for understanding the nature of wave propagation delays in MIT, it does suggest that these delays may not pose as great a problem to conductivity and permittivity measurement as was initially believed. However, further

research into this discrepancy is essential, as disagreement between theory and experiment is never satisfactory.

One possible reason for the discrepancy between theory and experiment here may be the fact that the theoretical treatment assumed a homogeneous propagation medium, while the experiment involved dielectric discontinuities (the air-water bath interface). The impact of such an interface on wave propagation is unclear, and further research into this area is needed. More accurate modelling is required; specifically a full solution of Maxwell's equations in an inhomogeneous dielectric medium. Initial studies have identified the Finite-Difference Time-Domain method (Yee 1966, Kunz and Luebbers 1993, Taflove and Hagnes 2000) as a promising candidate. This method calculates the electric and magnetic fields at all points in a grid of variable electrical properties. A stepping-in-time approach ensures the propagation of EM waves is suitably modelled. A FDTD solver has previously been used to model MIT measurements (Scharfetter *et al* 2002), although not for the estimation of wave propagation delays. This is a promising area for future research.

6.6. References

Feynman RP, Leighton RB, Sands M, 1964, Lectures on Physics (Addison-Wesley)

Gabriel S, Lau RW, Gabriel C, 1996, The dielectric properties of biological tissues: II. Measurements in the frequency range 10 Hz to 20 GHz. *Phys Med Biol*, vol. 41, p. 2251-2269

Gencer NG, Tek MN, 1998, Imaging tissue conductivity via contactless measurements: a feasibility study. *Elektrik*, vol. 6, no. 3, p. 183-200

Gough W, 2002, Wave propagation faster than light. *Eur. J. Phys.*, vol. 23, p. 17-19

Gough W, 2001, Private communication

Griffiths H, Stewart WR, Gough W, 1999, Magnetic induction tomography: a measuring system for biological tissues. *Annals of NY Acad. Sci.*, vol. 873, pp 335-345

Jackson JD, 1988, Classical Electrodynamics, Wiley

Kunz KS, Luebbers RJ, 1993, The Finite Difference Time Domain Method for Electromagnetics, CRC

Lorrain P, Corson DR, 1970, *Electromagnetic Fields and Waves*, W. H. Freeman & Co.

Morris A, Griffiths H, Gough W, 2001, A numerical model for magnetic induction tomographic measurements in biological tissues. *Physiol. Meas.*, vol. **22**, p.113-119

Scharfetter H, Riu P, Populo M, Rosell J, 2002, Sensitivity maps for low-contrast-perturbations within conducting background in magnetic induction tomography (MIT). *Physiol Meas*, vol. **23**, p.195-202

Taflove A, Hagnes SC, 2000, *Computational Electrodynamics*, Artech House

Yee KS 1966 Numerical solution of initial boundary value problems involving Maxwell's equations in isotropic media. *IEEE Trans. Antennas and Propagation*, **14**, 302-307

7. Future Work

7.1. Summary of this research

Image reconstruction and simulation studies in magnetic induction tomography have been studied in this thesis. A finite-difference model has been used to simulate MIT systems of varying sophistication. Comparison with analytical results and experimental measurements have illustrated the legitimacy of this method of simulation. The model has been used to calculate a sensitivity matrix, which relates (a linear approximation of) the changes in receiver coil emf to conductivity. A linear reconstruction algorithm, based on inversion of the sensitivity matrix using SVD, has been used to reconstruct images of conductivity perturbations from simulated and experimental MIT measurements. It has been shown that MIT can image conductivity perturbations of magnitudes that occur in pathology. The validity of using a quasi-static approximation in MIT has been investigated, resulting in an observed absence of theoretically predicted wave propagation delays.

There are questions resulting from this work that require further research to be answered. The values of conductivity reconstructed from experimental measurements (chapter 5) were significantly larger than the original sample conductivities; the influence of sensitivity matrix regularisation on this issue should be investigated. Also in chapter 5, the ability of the free-space sensitivity matrix to reconstruct images of better quality than the difference sensitivity matrix (section 5.3.4.3) is perplexing. Comparisons between experimental and simulated measurements made on different conductivity distributions may elucidate this issue. The apparent absence of theoretically predicted wave propagation delays, as reported in chapter 6, is a

particularly puzzling feature, and one that warrants careful attention. Although the lack of significant propagation delays is, at least superficially, helpful to conductivity imaging with MIT, the disagreement between theory and experiment can only be to its detriment.

7.2. Other areas of potential future work

7.2.1. Computer modelling

Another area of future work should be more realistic simulations of pathology/physiology using the Cardiff MIT model. This would identify potential future applications of medical MIT. The large contrast between cancerous and normal breast tissue referred to in chapter 1 suggests one possible application.

As suggested in chapter 6, the finite-difference time-domain method (FDTD) can be used to further investigate MIT. FDTD provides a full numerical solution to Maxwell's equations, and should be able to illuminate the lack of observed wave propagation delays described in chapter 6.

7.2.2. Image reconstruction

Relative permittivity imaging should be investigated, using the Cardiff MIT model, in the same way as used here for conductivity. As relative permittivity is in-phase with the primary signal and any capacitive coupling (unlike conductivity, which is in quadrature), it is likely to be more difficult to image. The ability to image both conductivity and relative permittivity from a single measurement technique would be extremely useful.

As image resolution in MIT depends on the number of independent measurements available, systems involving a larger number of coils (and hence independent measurements) should be simulated. For example, a system involving three 'tiers' of the 16 coil circular geometry used in the Cardiff MIT system (i.e. three 16 coils systems placed on top of each other) would theoretically give 2256 independent measurements. Increasing the number of independent measurements would allow fully three-dimensional sensitivity matrices to be used, eliminating the z-invariant conductivity constraint used in this work. The large number of measurements involved in such a system would take a large amount of time using the Cardiff MIT model. Finite-element method (FEM) simulations, commonly used in EIT, should be considered as an alternative for sensitivity matrix calculations, as the simulation times are reported as shorter. FEM would also facilitate iterative reconstruction methods, for the same reason of reduced simulation time (the sensitivity matrix could be continuously recalculated, based on conductivity calculated from the previous iteration).

7.2.3. MIT systems

Conductivity phantoms that represent typical pathological/physiological scenarios should be used in measurements taken by the Cardiff MIT system to investigate possible applications of medical MIT.

The single-channel planar system referred to in chapter 1 (Watson *et al* 2004) should be extended to a multichannel system, and the appropriate sensitivity matrix calculated to investigate the imaging properties of such a system.

Appendix A. The Cardiff MIT model code (Visual Fortran).

This appendix contains the Visual Fortran version of the Cardiff MIT model.

```
PROGRAM Quasistatic
```

```
! Calculates the measurements for an underdetermined system using a quasi-static model of a 16 coil MIT system.
```

```
USE QuasiGlobals  
IMPLICIT NONE
```

```
REAL(8) :: time1,time2,DUM1,DUM2  
INTEGER :: i,j,Ecoil,Dcoil,Voxel,Voxel1  
COMPLEX(8) :: MeasValues(MaxCoils,MaxCoils)
```

```
CALL CPU_TIME(time1)
```

```
! CALL ReciprocityCheck
```

```
! Open file in which measurements are to be stored
```

```
OPEN(4,file='C:\Program Files\Microsoft Visual Studio\MyProjects\Thesis\Glam Brain  
Meas\Four_Four_eight voxels\24cm diameter 8cm high 1 Sm\CondMeas.dat',form='formatted',status='new')  
OPEN(5,file='C:\Program Files\Microsoft Visual Studio\MyProjects\Thesis\Glam Brain  
Meas\Four_Four_eight voxels\24cm diameter 8cm high 1 Sm\PermMeas.dat',form='formatted',status='new')  
! OPEN(4,file='C:\Program Files\Microsoft Visual Studio\MyProjects\Thesis\Glam Brain Meas\Sim  
Stu Brain Meas\Meas.dat',form='formatted',status='new')
```

```
! Read in all 16 coil positions
```

```
CALL ReadCoilData
```

```
! Read in voxel data
```

```
CALL Dielectric_Data
```

```
! Calculate admittance between voxels
```

```
CALL Admittance
```

```
! Activate each excitaion coil in turn
```

```
DO Ecoil=1,MaxCoils
```

```
WRITE(*,*)  
WRITE(*,*)'ECOIL: ',Ecoil
```

```
! Calculate the electric field due to the excitation coil
```

```
CALL Electric_Field(Ecoil)
```



```

! Calculate the scalar potential distribution within the object
      CALL Electric_Potential(Ecoil)
! Calculate the electric current within the object
      CALL Electric_Current(Ecoil)
! Measure the induced emf in each of the detector coils
      DO Dcoil=1,MaxCoils
          WRITE(*,*)
          WRITE(*,*)' DCOIL:-',Dcoil
! Don't calculate for the same E and D coil
          IF(Dcoil.eq.Ecoil)GOTO 10
! Calculate the emf induced directly by the excitation coil
          CALL Direct_Influence_Emf(Ecoil,Dcoil,MeasValues)
! Calculate the emf induced by the eddy currents
          CALL Eddy_Current_Emf(Ecoil,Dcoil,MeasValues)
10      END DO
20  END DO
      CALL StoreValues(MeasValues)
      CALL CPU_TIME(time2)
      WRITE(*,*)
      WRITE(*,*)'TIME= ',time2-time1
      CLOSE(4)
      CLOSE(5)
101 FORMAT(F25.12)
200 FORMAT('ECoilPos=',f8.4,f8.4,f8.4,' DCoilPos=',f8.4,f8.4,f8.4)
300 FORMAT('ECoilOrien=',f8.4,f8.4,f8.4,' DCoilOrien=',f8.4,f8.4,f8.4)
END PROGRAM Quasistatic

```

SUBROUTINE ReadCoilData

USE QuasiGlobals
IMPLICIT NONE

INTEGER :: i
REAL(8) :: orienmag

OPEN(3,file='C:\Program Files\Microsoft Visual Studio\MyProjects\Thesis\Glam Brain
Meas\CoilDetails4.dat',form='formatted',status='old')

DO i=1,MaxCoils

READ(3,100)EcoilPos(i,1), EcoilPos(i,2), EcoilPos(i,3)
READ(3,100)EcoilOrien(i,1), EcoilOrien(i,2), EcoilOrien(i,3)

END DO

CLOSE(3)

OPEN(9,file='C:\Program Files\Microsoft Visual Studio\MyProjects\Thesis\Glam Brain
Meas\CoilDetails3.dat',form='formatted',status='old')

DO i=1,MaxCoils

READ(9,100)DcoilPos(i,1), DcoilPos(i,2), DcoilPos(i,3)
READ(9,100)DcoilOrien(i,1), DcoilOrien(i,2), DcoilOrien(i,3)

END DO

CLOSE(9)

DO i=1,MaxCoils

! Check that ECoil orientation vector is a unit vector

orienmag = DSQRT(EcoilOrien(i,1)**2 + EcoilOrien(i,2)**2 + EcoilOrien(i,3)**2)

IF((orienmag.gt.1.01D0).OR.(orienmag.lt.0.99D0))THEN

WRITE(*,*)'ECoil unit vector magnitude departs from unity by >1%'
STOP

END IF

! Check that DCoil orientation vector is a unit vector

orienmag = DSQRT(DcoilOrien(i,1)**2+DcoilOrien(i,2)**2+DcoilOrien(i,3)**2)

```
IF((orienmag.gt.1.01D0).OR.(orienmag.lt.0.99D0))THEN
```

```
    WRITE(*,*)'DCoil unit vector magnitude departs from unity by >1%'  
    STOP
```

```
END IF
```

```
END DO
```

```
100 FORMAT(3F25.12)
```

```
END SUBROUTINE ReadCoilData
```

```
SUBROUTINE Dielectric_Data
```

```
! Reads in dielectric distribution codes(id), and assigns relative  
! permittivity and conductivity values to each voxel
```

```
    USE DFLIB  
    USE QuasiGlobals  
    IMPLICIT NONE
```

```
    INTEGER :: i,j,k,n,iflag,inc  
    CHARACTER(20) :: layer
```

```
    inc=0
```

```
!     OPEN(2,file='C:\Program Files\Microsoft Visual Studio\MyProjects\Thesis\Glam Brain Meas\Sim  
Stu Brain Meas\Code_6cm.dat',form='formatted',status='old')
```

```
!     OPEN(2,file='C:\Program Files\Microsoft Visual Studio\MyProjects\Thesis\Glam Brain  
Meas\One_one_two_voxels\Cylinder_4dx_posC.dat',form='formatted',status='old')
```

```
!     OPEN(2,file='C:\Program Files\Microsoft Visual Studio\MyProjects\Thesis\Glam Brain  
Meas\Four_Four_eight_voxels\24cm diameter 8cm high 1
```

```
Sm\Code_120503_X5_24cm.dat',form='formatted',status='old')
```

```
    OPEN(2,file='C:\Program Files\Microsoft Visual Studio\MyProjects\Thesis\Glam Brain  
Meas\Four_Four_eight_voxels\20cm diameter 8cm
```

```
high\Code_120503_X2.dat',form='formatted',status='old')
```

```
!     OPEN(2,file='C:\Program Files\Microsoft Visual Studio\MyProjects\Thesis\Glam Brain  
Meas\Four_four_eight_voxels\UndDet.dat',form='formatted',status='old')
```

```
!     OPEN(2,file='C:\Program Files\Microsoft Visual Studio\MyProjects\Thesis\Glam Brain  
Meas\One_one_two_voxels\112_voxels 10 layers.dat',form='formatted',status='old')
```

```
    DO k=1,side
```

```

READ(2,*)layer
DO j=1,side
    n=(k-1)*(side**2)+(j-1)*side
    READ(2,201)(id(i),i=n+1,n+side)
END DO

```

```

END DO

```

```

! Check that boundary is entirely insulating (id=0)

```

```

! Bottom (k=1) & top (k=side) faces

```

```

DO n=1,side**2
    IF(id(n).ne.0.or.id((side**3-side**2)+n).ne.0)iflag=1
END DO

```

```

! Front (j=1) & rear (j=side) faces

```

```

DO i=1,side
    DO k=1,side
        n=(k-1)*(side**2)+i
        IF(id(n).ne.0.or.id((side**2-side)+n).ne.0)iflag=1
    END DO
END DO

```

```

! Left (i=1) & right (i=side) faces

```

```

DO j=1,side
    DO k=1,side
        n=(k-1)*(side**2)+(j-1)*side+1
        IF(id(n).ne.0.or.id(n+(side-1)).ne.0)iflag=1
    END DO
END DO

```

```

! Check boundary is all insulating

```

```

IF(iflag.eq.1)THEN
    WRITE(*,*)' boundary contains non-zero element'
    STOP
END IF
CLOSE(2)

```

```

! Set cond. and diel. const. for each pixel according to code id.

```

```

DO n=1,side**3
    IF((id(n).gt.0).AND.(id(n).le.1344))THEN
        diel(n,1) = 0.3D0 !sr(2*id(n)-1)
        diel(n,2) = 80.0D0 !sr(2*id(n)) !
    END IF

    IF(id(n).lt.0)THEN
        diel(n,1) = 0.3D0 !sr(2*(-id(n))-1)
        diel(n,2) = 80.0D0 !sr(2*(-id(n)))
    END IF

```

```

IF(id(n).eq.2)THEN

```

```

! 12, 97, 212 SET CONDUCTIVITY

```

```

        diel(n,1) = 1.0D0
        diel(n,2) = 80.0D0
    END IF

    IF(id(n).eq.-2)THEN
        diel(n,1) = 1.0D0
        diel(n,2) = 80.0D0
    END IF

    IF(id(n).gt.448)THEN
        WRITE(*,*)'Inadmissible tissue code (>448)'
        STOP
    END IF

```

```

END DO

```

```

201 FORMAT(200i4)

```

```

203 FORMAT(a20)

```

```

END SUBROUTINE Dielectric_Data

```

```

SUBROUTINE Admittance

```

```

! Calculates complex admittance between nodes

```

```

    USE QuasiGlobals

```

```

    IMPLICIT NONE

```

```

    INTEGER :: i,j,k,n,nj

```

```

    REAL(8) :: c1,c2,al,be,x,y

```

```

    DO k=1,(side-1)

```

```

        DO j=1,(side-1)

```

```

            nj=(k-1)*side**2+(j-1)*side

```

```

                DO i=1,(side-1)

```

```

                    n=(side**2)*(k-1)+side*(j-1)+i

```

```

! If node has a zero code, don't assign admittance to any of the

```

```

! three positive coordinate directions

```

```

        IF(id(n).eq.0)GOTO 103

```

```

! c1 is one of the constituents of admittance

```

```

        c1=2*dx*(diel(n,1)**2+we0*we0*diel(n,2)**2)

```

```

! If node to the right (+x-direction) has a zero code, leave admittance in positive

```

```

! x-direction a(n,1)=0

```

```

        IF(id(n+1).eq.0)GOTO 101

```

```

! Otherwise, calculate admittance a(n,1) in positive x-direction

```

```

      c2=2*dx*(diel(n+1,1)**2+we0*we0*diel(n+1,2)**2)
      al=diel(n,1)/c1+diel(n+1,1)/c2
      be=we0*(diel(n,2)/c1+diel(n+1,2)/c2)
      x=al/(al*al+be*be)
      y=be/(al*al+be*be)
      a(n,1)=CMPLX(x,y,8)

! If node behind (+y-direction) has a zero code, leave admittance in positive
! y-direction a(n,2)=0
101  IF(id(n+side).eq.0)GOTO 102

! Otherwise, calculate admittance a(n,2) in positive y-direction
      c2=2*dx*(diel(n+side,1)**2+we0*we0*diel(n+side,2)**2)
      al=diel(n,1)/c1+diel(n+side,1)/c2
      be=we0*(diel(n,2)/c1+diel(n+side,2)/c2)
      x=al/(al*al+be*be)
      y=be/(al*al+be*be)
      a(n,2)=CMPLX(x,y,8)

! If node above (+z-direction) has a zero code, leave admittance in positive
! z-direction a(n,3)=0
102  IF(id(n+side**2).eq.0)GOTO 103

! Otherwise, calculate admittance a(n,3) in positive z-direction
      c2=2*dx*(diel(n+side**2,1)**2+we0*we0*diel(n+side**2,2)**2)
      al=diel(n,1)/c1+diel(n+side**2,1)/c2
      be=we0*(diel(n,2)/c1+diel(n+side**2,2)/c2)
      x=al/(al*al+be*be)
      y=be/(al*al+be*be)
      a(n,3)=CMPLX(x,y,8)

103  CONTINUE
      END DO
      END DO
      END DO

50  FORMAT(8E9.2E2)

END SUBROUTINE Admittance

```

SUBROUTINE Electric_Field(Ecoil)

! Calculates magnetically induced electric field at each node in
! +x, +y and +z directions

```

      USE QuasiGlobals
      IMPLICIT NONE

```

```

    INTEGER :: i,j,k,n,nk,nj,Ecoil,t
    REAL(8) :: fkn,r,h,kn,kc,NodePosComp
    REAL(8) :: Aphi,Ax,Ay,Az,r2x,r2y,r2z
    REAL(8) :: rx,ry,rz,CEL,dist_inc,Dist_Calc

    DO k=2,(side-1)
        nk=(side**2)*(k-1)
        DO j=2,(side-1)
            nj=side*(j-1)
            DO i=2,(side-1)
                n=nk+nj+i

! If voxel is surrounded by free space, don't bother with the calculations
                IF((id(n+1).eq.0).AND.(id(n-1).eq.0).AND.(id(n+side).eq.0).AND.(id(n-side).eq.0)&
                    &.AND.(id(n+side**2).eq.0).AND.(id(n-side**2).eq.0))THEN

                    DO t=1,Points-1
                        eamp(n,1,t) = 0.0DO
                        eamp(n,2,t) = 0.0DO
                        eamp(n,3,t) = 0.0DO
                    END DO

                    ELSE IF(Dist_Calc(i,j,k,Ecoil).lt.(E_Deep*dx))THEN
! Call subroutine that calculates A

                    DO t=1,Points-1

                        dist_inc = (t-1)*(dx/(Points-1))

                        CALL
Magnetic_Vector_Potential(NodePosComp(i)+dist_inc,NodePosComp(j),&
NodePosComp(k),EcoilPos(Ecoil,1),EcoilPos(Ecoil,2),&
EcoilPos(Ecoil,3),EcoilRadius,EcoilCurrent,EcoilOrien(Ecoil,1),&
EcoilOrien(Ecoil,2),EcoilOrien(Ecoil,3),Ax,Ay,Az,n)

                        eamp(n,1,t) = -w*dx*Ax

                        CALL
Magnetic_Vector_Potential(NodePosComp(i),NodePosComp(j)+dist_inc,&
NodePosComp(k),EcoilPos(Ecoil,1),EcoilPos(Ecoil,2),&
EcoilPos(Ecoil,3),EcoilRadius,EcoilCurrent,EcoilOrien(Ecoil,1),&
EcoilOrien(Ecoil,2),EcoilOrien(Ecoil,3),Ax,Ay,Az,n)

                        eamp(n,2,t) = -w*dx*Ay

                        CALL
Magnetic_Vector_Potential(NodePosComp(i),NodePosComp(j),&

```

```

NodePosComp(k)+dist_inc,EcoilPos(Ecoil,1),EcoilPos(Ecoil,2),&
EcoilPos(Ecoil,3),EcoilRadius,EcoilCurrent,EcoilOrien(Ecoil,1),&
EcoilOrien(Ecoil,2),EcoilOrien(Ecoil,3),Ax,Ay,Az,n

                                eamp(n,3,t) = -w*dx*Az

                                END DO

                                ELSE

                                CALL
Magnetic_Vector_Potential(NodePosComp(i),NodePosComp(j),&
NodePosComp(k),EcoilPos(Ecoil,1),EcoilPos(Ecoil,2),&
EcoilPos(Ecoil,3),EcoilRadius,EcoilCurrent,EcoilOrien(Ecoil,1),&
                                EcoilOrien(Ecoil,2),EcoilOrien(Ecoil,3),Ax,Ay,Az,n)

                                eamp(n,1,1) = -w*dx*Ax
                                eamp(n,2,1) = -w*dx*Ay
                                eamp(n,3,1) = -w*dx*Az

                                END IF

                                END DO

                                END DO
END DO

```

END SUBROUTINE Electric_Field

SUBROUTINE Magnetic_Vector_Potential(r0x,r0y,r0z,r1x,r1y,r1z,radius,&

¤t,nx,ny,nz,Ax,Ay,Az,n)

! Calculates the magnetic vector potential A due to excitation coil
! at a point in the model (can be at a node or detector coil element).

USE QuasiGlobals
IMPLICIT NONE

! Dummy variables:- r0 is point where A is calculated, r1 is excitation
! coil position vector, n is excitation coil orientation vector,
! 'radius' is excitation coil radius, 'current' is excitation coil current

INTEGER :: n
REAL(8) :: r0x,r0y,r0z,r1x,r1y,r1z,r2x,r2y,r2z


```
REAL(8) :: h,fkn,kc,r,kn,rx,ry,rz,Aphi,Ax,Ay,Az,CEL
REAL(8) :: radius,current,nx,ny,nz,Dummy1
```

```
! r2 is vector joining ECoil to position at which A is to be calculated
```

```
r2x=r0x-r1x
r2y=r0y-r1y
r2z=r0z-r1z
```

```
! h is projection of r2 along ECoil orientation vector
```

```
h=r2x*nx+r2y*ny+r2z*nz
```

```
! (rx,ry,rz) is a vector in direction of Aphi
```

```
rx=r2y*nz-r2z*ny
ry=r2z*nx-r2x*nz
rz=r2x*ny-r2y*nx
```

```
! r is the magnitude of (rx,ry,rz)
```

```
r=DSQRT(rx*rx+ry*ry+rz*rz)
```

```
IF(r.le.1.0D-3)r=0.0D0
```

```
! kn and kc are needed in elliptic integral calculations
```

```
kn=DSQRT(4*r*radius/(h*h+(r+radius)**2))
kc=DSQRT(1-kn*kn)
```

```
! If kn=0 assign A=0, otherwise NaN
```

```
IF(kn.ne.0.0D0)THEN
```

```
! fkn is a function of elliptic integrals of 1st and 2nd kinds
```

```
! represented here by the CEL function
```

```
fkn=(((2/kn)-kn)*CEL(kc,1.0D0,1.0D0,1.0D0,pi))&
&-(2/kn)*CEL(kc,1.0D0,1.0D0,kc**2,pi)
```

```
! Aphi is magnetic vector potential in polar coordinate phi direction
```

```
Aphi=2D-7*current*DSQRT(radius/r)*fkn
```

```
! Ax,Ay,Az are in cartesian coordinates
```

```
Ax=Aphi*rx/r
Ay=Aphi*ry/r
Az=Aphi*rz/r
```

```
ELSE
```

```
Ax=0.0D0
Ay=0.0D0
Az=0.0D0
```

```
END IF
```

```
END SUBROUTINE Magnetic_Vector_Potential
```

SUBROUTINE Electric_Potential(Ecoil)

! Solves Poisson's equation by obeying Kirchoff's current law at each node.

USE QuasiGlobals
IMPLICIT NONE

INTEGER :: i,j,k,n,it,nk,nj,idn,ssi_flag,Ecoil
REAL(8) :: ssi,initial_ssi,ssi_drop,Dist_Calc
COMPLEX(8) :: a0,a1,a2,a3,a4,a5,a6,c0,e(6)

! Reference point for scalar potential

```
DO n=1,side**3
  IF(id(n).lt.0)THEN
    phi(n)=(0.0D0,0.0D0)
    WRITE(*,*)'POTENTIAL GROUND AT ',n
  END IF
END DO
```

! Initialize values

```
it=1
phi=(0.0D0,0.0D0)
ssi_flag=0
```

! Main iteration loop

9 ssi=0.0D0

```
DO k=2,(side-1)
  nk=(side**2)*(k-1)

  DO j=2,(side-1)
    nj = nk + side*(j-1)

    DO i=2,(side-1)
      n = nj + i
      idn = id(n)
```

! Don't change electrode or air outside body

```
IF(idn.le.0)GOTO 10      !.eq.-1.or.idn.eq.-2.or.idn.eq.0
```

! Admittance to left, right, front, behind, below and above

```
a1 = a(n-1,1)
a2 = a(n,1)
a3 = a(n-side,2)
a4 = a(n,2)
a5 = a(n-side**2,3)
a6 = a(n,3)
```

! Admittance sum

```
a0 = a1 + a2 + a3 + a4 + a5 + a6
```

! Voltage generators in the positive x, y and z directions

```
IF(Dist_Calc(i,j,k,Ecoil).lt.(E_Deep*dx))THEN
```

```

CALL Voltage_Generators(i,j,k,n,e,Ecoil)

ELSE

e(1) = (0.0D0,0.5D0)*(eamp(n-1,1,1)+eamp(n,1,i))
e(2) = (0.0D0,0.5D0)*(eamp(n,1,1)+eamp(n+1,1,1))
e(3) = (0.0D0,0.5D0)*(eamp(n-side,2,1)+eamp(n,2,1))
e(4) = (0.0D0,0.5D0)*(eamp(n,2,1)+eamp(n+side,2,1))
e(5) = (0.0D0,0.5D0)*(eamp(n-side**2,3,1)+eamp(n,3,1))
e(6) = (0.0D0,0.5D0)*(eamp(n,3,1)+eamp(n+side**2,3,1))

END IF

! c0 is the change in scalar potential from the previous iteration
c0 = ( a1*(phi(n-1)+e(1)) + a2*(phi(n+1)-e(2)) + a3*(phi(n-side)+e(3))+&
a4*(phi(n+side)-e(4)) + a5*(phi(n-side**2)+e(5)) + a6*(phi(n+side**2)-e(6))
)&
/a0 - phi(n)

! Calculate the sum of the squares of the increments (ssi) and potential (phi)
ssi = ssi + (CDABS(c0))**2
phi(n) = phi(n) + accel*c0

10 CONTINUE

END DO

END DO

END DO

! Set initial ssi
IF(ssi_flag.eq.0)THEN
initial_ssi=ssi
ssi_flag=1
END IF

! Calculate ssi_drop
ssi_drop=initial_ssi/ssi

! Increment iteration variable (it)
it=it+1

! WRITE(*,*)it,ssi_drop

! If the fall in scalar potential is to small, repeat calculation
IF(it.lt.maxit)GOTO 9 !ssi_drop.lt.ssilim.AND.

WRITE(*,*)"Total no. of iterations = ',it
write(*,100)ssi_drop

100 FORMAT('ssi_drop= ',E12.3)

```

END SUBROUTINE Electric_Potential

SUBROUTINE Electric_Current(Ecoil)

! Compute current elements in +x,+y,+z directions from each node

USE QuasiGlobals
IMPLICIT NONE

INTEGER :: i,j,k,n,nj,nk,Ecoil,flag,Nodes(side,side,side)
REAL(8) :: Dist_Calc
COMPLEX :: DummyCurrent(side**3,3)
COMPLEX(8) :: e(6)

!!!!Change the form to 'binary' when using Borland

display!!!!!!

! OPEN(2,file='C:\program files\borland\cbuilder4\projects\gl_mit&
! &\FlatCurrent.dat',form='binary',status='unknown')

flag = 0

Nodes = 0

DO k=2,(side-1)
nk=(side**2)*(k-1)

DO j=2,(side-1)
nj=side*(j-1)

DO i=2,(side-1)
n=nk+nj+i

! Voltage generators (e) in +x,+y,+z directions

IF(Dist_Calc(i,j,k,Ecoil).lt.(E_Deep*dx))THEN

! flag = flag + 1

IF(id(n).ne.0)Nodes(i,j,k) = 1

CALL Voltage_Generators(i,j,k,n,e,Ecoil)

ELSE

```

e(2) = (0.0D0,0.5D0)*(eamp(n,1,1)+eamp(n+1,1,1))
e(4) = (0.0D0,0.5D0)*(eamp(n,2,1)+eamp(n+side,2,1))
e(6) = (0.0D0,0.5D0)*(eamp(n,3,1)+eamp(n+side**2,3,1))

```

```

END IF

```

```

! Currents (xi) in +x,+y,+z directions

```

```

xi(n,1)=a(n,1)*(phi(n)-phi(n+1)+e(2))
xi(n,2)=a(n,2)*(phi(n)-phi(n+side)+e(4))
xi(n,3)=a(n,3)*(phi(n)-phi(n+side**2)+e(6))

```

```

END DO

```

```

END DO

```

```

END DO

```

```

! IF(Ecoil.eq.1)CALL NodeSelector(Nodes)

```

```

! WRITE(*,*)'No. of nodes within depth = ',flag
! read(*,*)

```

```

! DummyCurrent=xi
! WRITE(2)DummyCurrent
! CLOSE(2)
! read(*,*)

```

```

END SUBROUTINE Electric_Current

```

```

SUBROUTINE Direct_Influence_Emf(Ecoil,Dcoil,MeasValues)

```

```

! Calculates the induced emf in the detector coil due only to the
! direct influence of the excitation coil, i.e. NOT due to eddy currents

```

```

USE QuasiGlobals
IMPLICIT NONE

```

```

INTEGER :: n,Ecoil,Dcoil
REAL(8) :: b0x,b0y,b0z,b1x,b1y,b1z,b_comp,b2_comp,sine,cosine,beta,small_sine
REAL(8) :: dtheta,theta,Ax,Ay,Az,sine_values(DcoilElements),cosine_values(DcoilElements)
REAL(8) :: MeasValues(MaxCoils,MaxCoils)
COMPLEX(8) :: A_dl

```

```

! dtheta is the angle subtended by 1 coil element

```

```

dtheta=2*pi/DcoilElements

```

!Ensure emf starts at zero

```
direct_emf=(0.0D0,0.0D0)
```

! Create sin/cos look up table

```
DO n=1,DcoilElements
```

```
beta=dtheta*(n-1)  
sine_values(n)=SIN(beta)  
cosine_values(n)=COS(beta)
```

```
END DO
```

```
small_sine=SIN(dtheta/2)
```

! coil_axes calculates the local x and y axes of the DCoil

```
CALL coil_axes(DcoilOrien(Dcoil,1),DcoilOrien(Dcoil,2),DcoilOrien(Dcoil,3),&  
&DcoilRadius,b0x,b0y,b0z,b1x,b1y,b1z)
```

! Loop around the DCoil

```
DO n=1,DcoilElements
```

! theta is the angle from local x-axis to coil element radial vector

```
theta=dtheta*(n-1)
```

```
sine=sine_values(n)  
cosine=cosine_values(n)
```

! Call subroutine that calculates A

```
CALL Magnetic_Vector_Potential(DcoilPos(Dcoil,1)+b_comp(b0x,b1x,theta),&  
&DcoilPos(Dcoil,2)+b_comp(b0y,b1y,theta),DcoilPos(Dcoil,3)+b_comp(b0z,b1z,theta),&  
&EcoilPos(Ecoil,1),EcoilPos(Ecoil,2),EcoilPos(Ecoil,3),EcoilRadius,&  
&EcoilCurrent,EcoilOrien(Ecoil,1),EcoilOrien(Ecoil,2),EcoilOrien(Ecoil,3),&  
&Ax,Ay,Az,n)
```

! A_dl is the product of vector potential A and coil element dl (b2 here)

```
A_dl=Ax*b2_comp(b1x,b0x,sine,cosine,small_sine)&  
&+Ay*b2_comp(b1y,b0y,sine,cosine,small_sine)&  
&+Az*b2_comp(b1z,b0z,sine,cosine,small_sine)
```

! emf is the line integral of w.A.dl around DCoil

! i.e. it is the emf due to the DIRECT INFLUENCE of the excitation coil

```
direct_emf=direct_emf-(0.0D0,1.0D0)*w*A_dl
```

```
END DO
```

```

MeasValues(Ecoil,Dcoil)=IMAG(direct_emf)

! WRITE(*,*)'Directly Induced Emf= ',direct_emf

END SUBROUTINE Direct_Influence_Emf

SUBROUTINE Eddy_Current_Emf(Ecoil,Dcoil,MeasValues)
! Calculates the emf induced in the detector coil due to the
! dielectric block eddy current elements

USE QuasiGlobals
IMPLICIT NONE

INTEGER :: i,j,k,n,nk,nj,s,Ecoil,Dcoil
REAL(8) ::
magrx,magry,magrz,b2_comp,b0x,b0y,b0z,b1x,b1y,b1z,sine,cosine,beta,small_sine,mu_prod
REAL(8) :: NodePosComp,theta,dtheta,sine_values(DcoilElements),cosine_values(DcoilElements)
REAL(8) :: Dist_comp
REAL(8) :: magrx1,magrx2,magrx3,magry1,magry2,magry3,magrz1,magrz2,magrz3
COMPLEX(8) ::
A_dl,Ax,Ay,Az,nearly_Ax,nearly_Ay,nearly_Az,MeasValues(MaxCoils,MaxCoils)

! Ensure emf starts at zero
eddy_emf=(0.0D0,0.0D0)

! dtheta is the angle subtended by 1 coil element
dtheta=2*pi/DcoilElements

! Create look-up table of sin and cos values, so that SIN and COS aren't called
! during iteration loop

DO s=1,DcoilElements
    beta=dtheta*(s-1)
    sine_values(s)=SIN(beta)
    cosine_values(s)=COS(beta)
END DO

small_sine=SIN(dtheta/2)
mu_prod=(mu0*dx)/(4*pi)

! coil_axes calculates the local x and y axes of the DCoil
CALL coil_axes(DcoilOrient(Dcoil,1),DcoilOrient(Dcoil,2),DcoilOrient(Dcoil,3),&
&DcoilRadius,b0x,b0y,b0z,b1x,b1y,b1z)

! Loop through the block
DO k=2,side-1
    nk=(side**2)*(k-1)

```

```

DO j=2,side-1
  nj=side*(j-1)

  DO i=2,side-1
    n=nk+nj+i

! Reset A_dl=0 at start of each integration around the coil
    A_dl = (0.0D0,0.0D0)

! Calculate part of Ax that's independent of coil element
    nearly_Ax = mu_prod*xi(n,1)
    nearly_Ay = mu_prod*xi(n,2)
    nearly_Az = mu_prod*xi(n,3)

! Loop around the circle
    DO s=1,DcoilElements

! theta is the angle from local x-axis to coil element radial vector
        theta=dtheta*(s-1)

        sine=sine_values(s)
        cosine=cosine_values(s)

! Call subroutine that calculates distance from coil element
! to eddy current elements
        CALL
Distance(DcoilPos(Dcoil,1),DcoilPos(Dcoil,2),DcoilPos(Dcoil,3),b0x,&
        &b0y,b0z,b1x,b1y,b1z,sine,cosine,NodePosComp(i)+dx/2,&
        &NodePosComp(j),NodePosComp(k),NodePosComp(i),&
        &NodePosComp(j)+dx/2,NodePosComp(k),&
        &NodePosComp(i),NodePosComp(j),NodePosComp(k)+dx/2,&
        &magrx,magry,magrz)

! If the current element in the x-direction is close to the coil element, split it up into 'elements'
! separate elements
        IF(magrx.lt.(D_Deep*dx))THEN

                CALL
Refine_x(Ax,nearly_Ax,b0x,b0y,b0z,b1x,b1y,b1z,sine,cosine,Dcoil,i,j,k)

        ELSE

! If it's not too close, don't

                Ax = nearly_Ax / magrx

        END IF
    END DO
  END DO

```


! If the current element in the y-direction is close to the coil element, split it up into 'elements'
! separate elements

IF(magry.lt.(D_Deep*dx))THEN

CALL

Refine_y(Ay,nearly_Ay,b0x,b0y,b0z,b1x,b1y,b1z,sine,cosine,Dcoil,i,j,k)

ELSE

! If it's not too close, don't

Ay = nearly_Ay / magry

END IF

! If the current element in the z-direction is close to the coil element, split it up into 'elements'
! separate elements

IF(magrz.lt.(D_Deep*dx))THEN

CALL

Refine_z(Az,nearly_Az,b0x,b0y,b0z,b1x,b1y,b1z,sine,cosine,Dcoil,i,j,k)

ELSE

! If it's not too close, don't

Az = nearly_Az / magrz

END IF

! Perform summation of A.dl (i.e. product of vector potential A and
! coil element dl [b2]) for all coil elements

A_dl = A_dl + Ax*b2_comp(b1x,b0x,sine,cosine,small_sine)&
& + Ay*b2_comp(b1y,b0y,sine,cosine,small_sine)&
& +

Az*b2_comp(b1z,b0z,sine,cosine,small_sine)

END DO

! Perform line integral around DCoil to give emf due to one eddy
! current element, and sum to give emf due to all eddy currents

eddy_emf=eddy_emf-(0.0D0,1.0D0)*w*A_dl

END DO

END DO

END DO

```
MeasValues(Ecoil,Dcoil)= eddy_emf      !/IMAG(direct_emf)
```

```
END SUBROUTINE Eddy_Current_Emf
```

```
SUBROUTINE StoreValues(Values)
```

```
! This stores the measurements (i.e. for each conductivity perturbation) as a 16x16 matrix
```

```
USE QuasiGlobals  
IMPLICIT NONE
```

```
INTEGER :: i,j  
COMPLEX(8) :: Values(MaxCoils,MaxCoils)
```

```
DO i=1,MaxCoils
```

```
    WRITE(4,200)(REAL(Values(i,j)),j=1,MaxCoils)  
    WRITE(5,200)(IMAG(Values(i,j)),j=1,MaxCoils)
```

```
END DO
```

```
WRITE(4,*)  
WRITE(5,*)
```

```
100 FORMAT(200F25.12)
```

```
200 FORMAT(200E25.12)
```

```
END SUBROUTINE StoreValues
```

```
SUBROUTINE coil_axes(mx,my,mz,b,b0x,b0y,b0z,b1x,b1y,b1z)
```

```
! Defines the local x and y axes of the Rcoil
```

```
IMPLICIT NONE
```

```
REAL(8) :: mx,my,mz,b,b0x,b0y,b0z,b1x,b1y,b1z
```

```

! Defines b0 if DCoil orientation vector is in y-z plane
  IF(DABS(mx).lt.1D-6)THEN
    b0x=b
    b0y=0.0          ! b0 is a vector from the DCoil centre
    b0z=0.0          ! to a point on the DCoil, i.e. local x-axis
    GOTO 200
  END IF

! Defines b0 if DCoil orientation vector is in x-z plane
  IF(DABS(my).lt.1D-6)THEN
    b0x=0.0
    b0y=b
    b0z=0.0
    GOTO 200
  END IF

! Define b0 otherwise
  b0x=b/(DSQRT(1+((mx*mx)/(my*my))))
  b0y=b/(DSQRT(1+((my*my)/(mx*mx))))
  b0z=0.0

! Assigns the correct sign (- or +) to b0
  IF(my.lt.0.0)b0x=DABS(b0x)
  IF(my.gt.0.0)b0x=-DABS(b0x)
  IF(mx.lt.0.0)b0y=-DABS(b0y)
  IF(mx.gt.0.0)b0y=DABS(b0y)

! Checks that DCoil orientation vector and local x-axis are at
! right angles
200  IF(DABS(mx*b0x+my*b0y+mz*b0z).gt.1D-6)THEN
      WRITE(*,*)'Rx coil orientation vector and radial vector not at&
& right angles'
      STOP
    END IF

! Define DCoil local y-axis (b1)
  b1x=my*b0z-mz*b0y
  b1y=mz*b0x-mx*b0z
  b1z=mx*b0y-my*b0x

END SUBROUTINE coil_axes

SUBROUTINE Refine_x(Ax,nearly_Ax,b0x,b0y,b0z,b1x,b1y,b1z,sine,cosine,Dcoil,i,j,k)

  USE QuasiGlobals, ONLY:DcoilPos,dx,elements
  IMPLICIT NONE

```

```
INTEGER :: i,j,k,n,Dcoil
REAL(8) :: magrx1,magrx2,magrx3,Dist_comp,NodePosComp,inv_rx
REAL(8) :: b0x,b0y,b0z,b1x,b1y,b1z,sine,cosine
COMPLEX(8) :: Ax,nearly_Ax
```

```
inv_rx = 0.0D0
```

```
DO n=1,elements
```

```
    inv_rx = inv_rx + 1.0D0 /
```

```
Dist_comp(DcoilPos(Dcoil,1),DcoilPos(Dcoil,2),DcoilPos(Dcoil,3),&
```

```
    b0x,b0y,b0z,b1x,b1y,b1z,sine,cosine,&
```

```
    NodePosComp(i)+(n-0.5)*(dx/elements),NodePosComp(j),NodePosComp(k))
```

```
END DO
```

```
Ax = (nearly_Ax / REAL(elements))*inv_rx
```

```
END SUBROUTINE Refine_x
```

```
SUBROUTINE Refine_y(Ay,nearly_Ay,b0x,b0y,b0z,b1x,b1y,b1z,sine,cosine,Dcoil,i,j,k)
```

```
USE QuasiGlobals, ONLY:DcoilPos,dx,elements
```

```
IMPLICIT NONE
```

```
INTEGER :: i,j,k,n,Dcoil
```

```
REAL(8) :: magry1,magry2,magry3,Dist_comp,NodePosComp,inv_ry
```

```
REAL(8) :: b0x,b0y,b0z,b1x,b1y,b1z,sine,cosine
```

```
COMPLEX(8) :: Ay,nearly_Ay
```

```
inv_ry = 0.0D0
```

```
DO n=1,elements
```

```
    inv_ry = inv_ry + 1.0D0 /
```

```
Dist_comp(DcoilPos(Dcoil,1),DcoilPos(Dcoil,2),DcoilPos(Dcoil,3),&
```

```
    b0x,b0y,b0z,b1x,b1y,b1z,sine,cosine,&
```

```
    NodePosComp(i),NodePosComp(j)+(n-0.5)*(dx/elements),NodePosComp(k))
```

```
END DO
```

```
Ay = (nearly_Ay / REAL(elements))*inv_ry
```

END SUBROUTINE Refine_y

SUBROUTINE Refine_z(Az,nearly_Az,b0x,b0y,b0z,b1x,b1y,b1z,sine,cosine,Dcoil,i,j,k)

USE QuasiGlobals, ONLY: DcoilPos,dx,elements
IMPLICIT NONE

INTEGER :: i,j,k,n,Dcoil
REAL(8) :: magrz1,magrz2,magrz3,Dist_comp,NodePosComp,inv_rz
REAL(8) :: b0x,b0y,b0z,b1x,b1y,b1z,sine,cosine
COMPLEX(8) :: Az,nearly_Az

inv_rz = 0.0D0

DO n=1,elements

 inv_rz = inv_rz + 1.0D0 /
Dist_comp(DcoilPos(Dcoil,1),DcoilPos(Dcoil,2),DcoilPos(Dcoil,3),&

 b0x,b0y,b0z,b1x,b1y,b1z,sine,cosine,&

 NodePosComp(i),NodePosComp(j),NodePosComp(k)+(n-0.5)*(dx/elements))
END DO

Az = (nearly_Az / REAL(elements))*inv_rz

END SUBROUTINE Refine_z

REAL(8) FUNCTION NodePosComp(num)
! Returns a component of the node position vector

USE QuasiGlobals, ONLY: dx,side
IMPLICIT NONE

INTEGER :: num

NodePosComp=(num-side/2-0.5)* dx

END FUNCTION NodePosComp

REAL(8) FUNCTION CEL(QQC,PP,AA,BB,PI)
! Calculates elliptic integrals (taken from numerical recipes)

IMPLICIT NONE

REAL(8) :: QQC,PP,AA,BB,A,B,P,E,EM,F,QC,Q,G,PI,PIO2
REAL(8), PARAMETER :: CA=0.0003

PIO2=PI/2

IF(QQC.eq.0.)pause'failure in CEL'
QC=DABS(QQC)
A=AA
B=BB
P=PP
E=QC
EM=1.0

IF(P.gt.0.)THEN
P=DSQRT(P)
B=B/P
ELSE
F=QC*QC
Q=1.0-F
G=1.0-p
F=F-P
Q=Q*(B-A*P)
P=DSQRT(F/G)
A=(A-B)/G
B=-Q/(G*G*P)+A*P
END IF

1 F=A
A=A+B/P
G=E/P
B=B+F*G
B=B+B
P=G+P
G=EM
EM=QC+EM

IF(ABS(G-QC).gt.G*CA)THEN
QC=DSQRT(E)
QC=QC+QC
E=QC*EM
GOTO 1

END IF

CEL=PIO2*(B+A*EM)/(EM*(EM+P))

END FUNCTION CEL

REAL(8) FUNCTION b_comp(b0_comp,b1_comp,angle)
! Returns a component of the vector from the coil centre to the
! position at which A will be calculated (b_comp)

IMPLICIT NONE

REAL(8) :: b0_comp,b1_comp,angle

b_comp=b0_comp*COS(angle)+b1_comp*SIN(angle)

END FUNCTION b_comp

REAL(8) FUNCTION b2_comp(b1_comp,b0_comp,sine,cosine,small_sine)
! Returns the coil element component of b2 (dl)

IMPLICIT NONE

REAL(8) :: b1_comp,b0_comp,sine,cosine,small_sine

b2_comp=2*small_sine*(b1_comp*cosine -b0_comp*sine)

END FUNCTION b2_comp

SUBROUTINE Distance(r3x,r3y,r3z,b0x,b0y,b0z,b1x,b1y,b1z,sine,cosine,&
 &r1xx,r1xy,r1xz,r1yx,r1yy,r1yz,r1zx,r1zy,r1zz,&
 &magrx,magry,magrz)

! This returns the distance between the coil element and the
! eddy current elements

IMPLICIT NONE

! Dummy variables:- r3 is the position vector of the DCoil centre,
! r1x is the position vector of the eddy current element in the
! +x-direction, etc.

REAL(8) magrx,magry,magrz,r3x,r3y,r3z,b0x,b0y,b0z
REAL(8) r1xx,r1xy,r1xz,r1yx,r1yy,r1yz,r1zx,r1zy,r1zz
REAL(8) b1x,b1y,b1z,sine,cosine,r0_comp

! magrx is the distance from coil element to eddy current element
! in the +x-direction, etc.
! r0_comp returns a component of the position vector of the coil element

```
magrx = SQRT((r0_comp(r3x,b0x,b1x,sine,cosine)-r1xx)**2&
&+(r0_comp(r3y,b0y,b1y,sine,cosine)-r1xy)**2&
&+(r0_comp(r3z,b0z,b1z,sine,cosine)-r1xz)**2)
```

```
magry = SQRT((r0_comp(r3x,b0x,b1x,sine,cosine)-r1yx)**2&
&+(r0_comp(r3y,b0y,b1y,sine,cosine)-r1yy)**2&
&+(r0_comp(r3z,b0z,b1z,sine,cosine)-r1yz)**2)
```

```
magrz = SQRT((r0_comp(r3x,b0x,b1x,sine,cosine)-r1zx)**2&
&+(r0_comp(r3y,b0y,b1y,sine,cosine)-r1zy)**2&
&+(r0_comp(r3z,b0z,b1z,sine,cosine)-r1zz)**2)
```

END SUBROUTINE Distance

REAL(8) FUNCTION Dist_Calc(i,j,k,Ecoil)

```
USE QuasiGlobals, ONLY: EcoilPos
IMPLICIT NONE
```

```
INTEGER :: i,j,k,Ecoil
REAL(8) :: NodePosComp
```

```
Dist_Calc = DSQRT( (NodePosComp(i)-EcoilPos(Ecoil,1))**2 + &
(NodePosComp(j)-EcoilPos(Ecoil,2))**2 + &
(NodePosComp(k)-EcoilPos(Ecoil,3))**2 )
```

END FUNCTION Dist_Calc

REAL(8) FUNCTION Dist_comp(r3x,r3y,r3z,b0x,b0y,b0z,b1x,b1y,b1z,sine,cosine,&
&r1comp1,r1comp2,r1comp3)

! This effectively calculates the distance between two points, the
! mid-point of the current element, and the mid-point of the coil element

```
IMPLICIT NONE
```

```
REAL(8) magrx,magry,magrz,r3x,r3y,r3z,b0x,b0y,b0z
REAL(8) r1comp1,r1comp2,r1comp3
REAL(8) b1x,b1y,b1z,sine,cosine,r0_comp
```

! Dummy variables:- r3 is the position vector of the DCoil centre,
! r1x is the position vector of the eddy current element in the
! +x-direction, etc.
! r0_comp returns a component of the position vector of the coil element


```
Dist_comp = SQRT((r0_comp(r3x,b0x,b1x,sine,cosine)-rIcomp1)**2&
                 &+(r0_comp(r3y,b0y,b1y,sine,cosine)-rIcomp2)**2&
                 &+(r0_comp(r3z,b0z,b1z,sine,cosine)-rIcomp3)**2)
```

```
END FUNCTION Dist_comp
```

```
REAL(8) FUNCTION r0_comp(r3_comp,b0_comp,b1_comp,sine,cosine)
! Returns a component of the position vector of the coil element
```

```
IMPLICIT NONE
```

```
REAL(8) r3_comp,b0_comp,b1_comp,sine,cosine
```

```
r0_comp=r3_comp+b0_comp*cosine+b1_comp*sine
```

```
END FUNCTION r0_comp
```

Appendix B. Derivation of complex admittance equations.

This appendix describes the calculation of complex admittance from knowledge of voxel conductivities and relative permittivities, as used in the Cardiff MIT model. The admittance between one voxel and the next in the positive x-direction will be considered as an example.

For nodes n and $n+1$ having a conductivity and relative permittivity σ_n , ϵ_n , σ_{n+1} , and ϵ_{n+1} respectively, and equivalent resistor-capacitor network (figure 1) can be used to calculate impedance. The equivalent resistance R_n and capacitance C_n are given by

$$R_n = \frac{1}{2\Delta x \sigma_n} \quad (\text{B.1})$$

$$C_n = 2\Delta x \epsilon_n \quad (\text{B.2})$$

where Δx is the inter-node spacing.

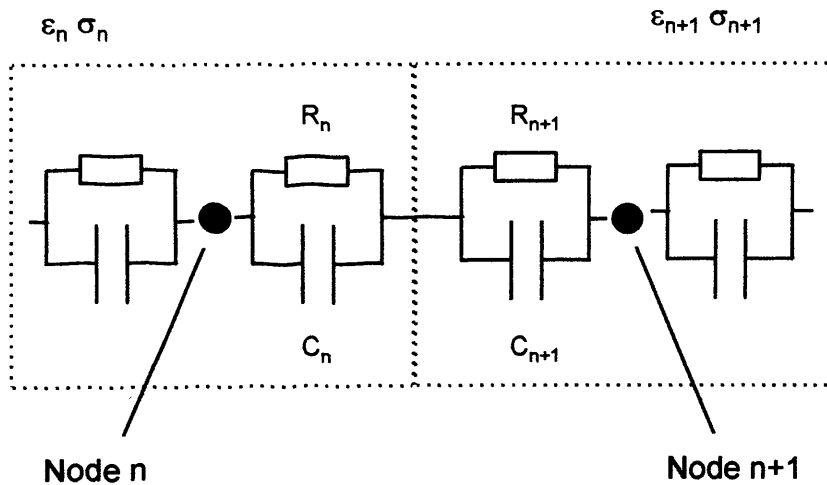


Figure 1. The equivalent resistor-capacitor network for two nodes n and $n+1$.

The impedances of the resistive and capacitive components are given by

$$Z_n^R = R \quad (\text{B.3})$$

$$Z_n^C = \frac{1}{j\omega C_n} \quad (\text{B.4})$$

respectively, where ω is the angular frequency of the transmitter coil current. The impedance associated with node n is

$$Z_n = \frac{Z_n^C Z_n^R}{Z_n^C + Z_n^R} = \frac{R_n / j\omega C_n}{R_n + j\omega C_n} = \frac{R_n}{j\omega C_n R_n + 1} \quad (\text{B.5})$$

and substituting (B.1) and (B.2) into (B.5) gives

$$Z_n = \frac{1}{2\Delta x(\sigma_n + j\omega\epsilon_n)} \quad (\text{B.6})$$

Multiplying top and bottom by the complex conjugate of the denominator results in

$$Z_n = \frac{\sigma_n - j\omega\epsilon_n}{2\Delta x(\sigma_n^2 + \omega^2\epsilon_n^2)} \quad (\text{B.7})$$

Defining the variables

$$C_1 = 2\Delta x(\sigma_n^2 + \omega^2\epsilon_n^2) \quad (\text{B.8})$$

$$C_2 = 2\Delta x(\sigma_{n+1}^2 + \omega^2\epsilon_{n+1}^2) \quad (\text{B.9})$$

leads to

$$Z_1 = \frac{\sigma_n - j\omega\epsilon_n}{C_1} \quad (\text{B.10})$$

$$Z_2 = \frac{\sigma_{n+1} - j\omega\epsilon_{n+1}}{C_2} \quad (\text{B.11})$$

where Z_1 is the impedance associated with the parallel combination of R_1 and C_1 , and Z_2 is that for R_2 and C_2 . The total impedance between the two nodes in the x -direction is $Z = Z_1 + Z_2$, or

$$Z = \frac{\sigma_n}{C_1} + \frac{\sigma_{n+1}}{C_2} - j\omega \left(\frac{\epsilon_n}{C_1} + \frac{\epsilon_{n+1}}{C_2} \right) \quad (\text{B.12})$$

Defining

$$\alpha = \frac{\sigma_n}{C_1} + \frac{\sigma_{n+1}}{C_2} \quad (\text{B.13})$$

$$\beta = \omega \left(\frac{\epsilon_n}{C_1} + \frac{\epsilon_{n+1}}{C_2} \right) \quad (\text{B.14})$$

leads to a concise equation for the impedance between two voxels

$$Z = \alpha - j\beta \quad (\text{B.15})$$

The admittance, Y , is

$$Y = \frac{1}{Z} = \frac{1}{\alpha - j\beta} \quad (\text{B.16})$$

Multiplying (B.16) by its complex conjugate, and substituting equations (B.17) and

(B.18)

$$x = \frac{\alpha}{\alpha^2 + \beta^2} \quad (\text{B.17})$$

$$y = \frac{\beta}{\alpha^2 + \beta^2} \quad (\text{B.18})$$

into (B.16) gives

$$a = x + jy \quad (\text{B.19})$$

These equations are used in the Cardiff MIT model code for the calculation of inter-node impedances.

Appendix C. Simulating random noise

Random, or Gaussian, noise can be simulated and added to measurement simulations to make them more 'realistic'. Here, random noise was calculated using the standard normal (Gaussian) distribution function

$$F(t) = \frac{1}{\sqrt{2\pi}} \int_{-\infty}^x e^{-t^2/2} dt \quad (\text{C.1})$$

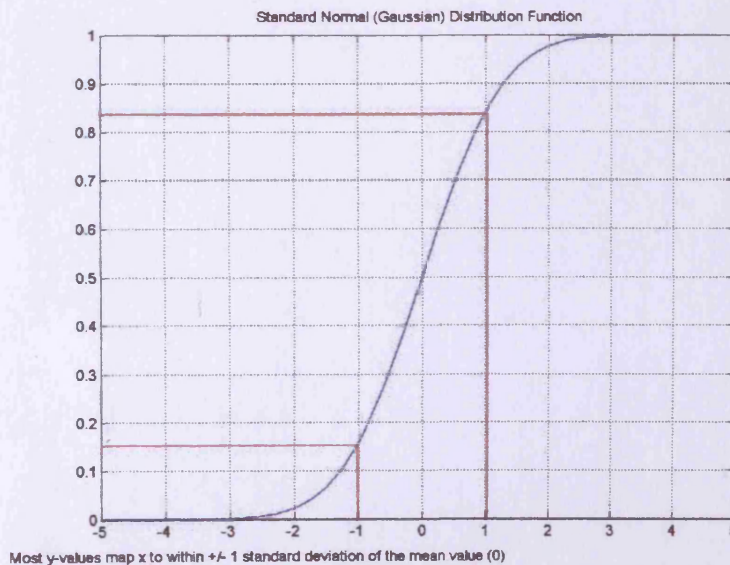
which was calculated in terms of the standard error function

$$\text{erf}(x) = \frac{2}{\sqrt{\pi}} \int_0^x e^{-t^2} dt \quad (\text{C.2})$$

provided in Matlab 6.0, such that

$$F = \frac{1}{2} + \frac{1}{2} \text{erf}\left(\frac{x}{\sqrt{2}}\right) \quad (\text{C.3})$$

A graph of this function is shown below.



This function was calculated for $x = -4$ to $+4$ in steps of 0.1 , so 81 values in total. The random number generator function 'rand' in Matlab was used to generate a number between 0 and 1 . Linear interpolation found the x -value corresponding to this random number on the above graph. This x -value was then multiplied by the standard deviation to give the random error, which was then added to a simulated measurement value. This process was repeated for all simulated measurements.